Exciton Dephasing Mechanism of CdSe and CuBr Quantum Dots Embedded in Matrix

Kazuya TAKEMOTO

A dissertation submitted to the Doctoral Program
in Physics, the University of Tsukuba
in partial fulfillment of the requirements
for the degree of Doctor of Philosophy in Science

January 2003

Abstract

Low-temperature exciton dephasing mechanism of CdSe quantum dots and CuBr quantum dots was investigated using accumulated photon echo method. The accumulated photon echo with a phase-modulation technique has high sensitivity for detecting signals even under extremely weak excitation intensity. Using this, we have investigated in detail the temperature dependence of the homogeneous linewidth from the time domain. It has been clarified that the two excitations, the small energy excitation in the two-level system (TLS) and the confined acoustic phonons, determine the low-temeperature dependence of the homogeneous linewidth in CdSe and CuBr quantum dots.

The TLS is a model based on the assumption that quantum mechanical tunneling takes place through double-potential wells in the host matrix near the quantum dots, bringing about the anomalous nonlinear temperature dependence of the homogeneous linewidth for CuBr quantum dots in NaBr below 15 K. On the other hand, T-linear dependence due to the TLS was observed for CdSe and CuBr quantum dots in glass at very low temperature. The difference of the TLS-energy distribution is considered to cause matrix-dependent temperature dependence in the low-temperature region between glass- and crystal-matrix samples. With increasing temperature, the two-phonon Raman process of confined acoustic phonons becomes dominant for all the samples, leading to the quadratic temperature dependence of the homogeneous linewidth. The existence of confined phonons was also confirmed by Raman scattering and persistent spectral hole-burning experiment.

Those results agree well with the previous report of CuCl quantum dots, indicating the universal influence of the surface-related effects and confined-phonon scattering on the excitonic dephasing mechanism of semiconductor quantum dots embedded in matrices.

Contents

Chapter 1

General Introduction

In recent years, a considerable number of studies have been made on zero-dimensional semiconductor systems. These systems have small dimensions lying in nanometer or less scale, and have been called as semiconductor "quantum dot". The most striking feature of quantum dots is atomic-like quantized energy levels due to three-dimensional confinement effect [1, 2]. If the quantum confinement effect prevents excitons in quantum dots from losing their coherence, the excitonic dephasing or phase relaxation time, T_2, in quantum dots is expected to be much longer than in the bulk materials. In this case quantum dots would have extremely sharp optical spectra whose linewidth, Γ_h, is limited only by the population relaxation time as $\Gamma_h = 2\hbar/T_2 \approx \hbar/T_1$. This is the reason why quantum dots have been believed to be suitable for application to devices especially for quantum information processing [3, 4], because long dephasing time makes a number of implementations possible until the decoherence takes place. Several kinds of coherent nonlinear optical phenomena has been proposed and demonstrated, such as optical control of polarizations and spins [3–6], Rabi oscillations [7, 8], and optically induced entanglement [9].

However in real quantum dots, the dephasing time is not so long as to realize the δ-function-like homogeneous linewidth. Although the dephasing time of quantum dots ranging from tens of picoseconds to a nanosecond of I-VII, II-VI and III-V semiconductor quantum dots has been reported so far, a good knowledge of the dephasing mechanism of excitons confined in quantum dots could not be obtained yet. For example, the longest dephasing time of fundamental exciton transition, $T_2 = 1.3$ ns ($\Gamma_h \approx 1\,\mu$eV) has been directly

measured from time-domain using accumulated photon echo for CuCl quantum dots embedded in NaCl matrix [10]. For CuCl quantum dots in glass, dephasing time of $T_2 = 650$ ps ($\Gamma_h \approx 2\,\mu$eV) was reported using the same technique. However, shorter value of T_2, 130 ps, was also reported for the same kind of sample by using transient four-wave mixing (TFWM) [11]. In the case of InGaAs self-assembled quantum dots, the dephasing time of 630 ps ($\Gamma_h \approx 2\,\mu$eV) measured by TFWM technique has been reported [12]. On the other hand, in the spectral domain, recent single quantum dot photoluminescence experiments on III-V self-assembled quantum dots [13–15] have shown spectral line widths of ≈ 50 μeV corresponding to $T_2 = 13$ ps, which is still too short compared to the dephasing time obtained from the FWM experiment. The one possible reason of the above discrepancies lies in the difference of their experimental technique. In single quantum dot spectroscopy, the linewidth which is comparable to or narrower than 0.1 meV is too sharp to be studied with sufficient spectral resolution. The TFWM has also difficulty with detecting signals under weak excitation intensity where no carrier-carrier scattering can be observed. These experimental difficulties have masked the intrinsic physical properties. From the fundamental physical point of view, investigating the mechanism to shorten the dephasing time of quantum dots using "reliable" technique is most important.

The homogeneous broadening, or excitonic dephasing time is determined by various mechanisms such as lifetime broadening, exciton-exciton scattering, exciton-phonon scattering, impurity or defect scattering, and surface scattering. The question about how an optical homogeneous spectrum changes as a function of temperature provides motivation to clarify the origin of excitonic dephasing, because the above dephasing mechanisms should have own characteristic temperature dependence. Generally in bulk semiconductor, the dephasing is mainly caused by *inelastic* scattering of excitons, which is the transitions between different states accompanied by thermalization, energy relaxation, or recombination processes. Although energy conservation between initial and final states is required in these processes, a continuum electronic spectrum in higher dimensional crystal realizes the corresponding loss of population of the radiative state. In this case, the loss of

phase coherence comes from scattering of exciton by optical or acoustic phonons, resulting in temperature-dependent homogeneous broadening [13]. In the case of quantum dots, not only the electron-hole states but also the low-frequency vibrational (acoustic phonon) modes are quantized. Therefore, the interaction of carriers with acoustic phonons is reduced due to the absence of suited states between the discrete energy levels (phonon bottleneck). In other words, the inelastic scattering in quantum dots is allowed by the one-phonon-assisted interlevel transition only for energy matching phonons. Then, temperature dependent homogeneous broadening of zero-phonon line separated from the other lines by more than phonon energy is dominated only by inefficient two-phonon Raman scattering (*elastic* scattering) which brings about the narrow linewidth, nonlinear temperature broadening and the long dephasing time in the time domain. Nevertheless linear temperature broadening or activation type nonlinear temperature broadening was contradictorily reported in the self-assembled quantum dots [12, 16]. On the other hand, two-acoustic-phonon process was reported in CuCl quantum dots in the weak confinement regime [10, 17] and in CdSe quantum dots embedded in the polymer [18]. Serious difference is present in the understanding of the temperature-dependent homogeneous broadening and dephasing mechanism of quantum dots. The possible difference between two categories seems to arise from the different condition whether phonon confinement is present or not. To clarify the phonon broadening mechanism of the zero-phonon line, we should investigate different kinds of quantum dots whose acoustic phonons are confined, because discrete phonon energy does not blur out temperature dependence of broadening.

The another problem is that most study of the temperature-dependent homogeneous broadening has been done without paying attention to the surrounding matrix. Quantum dots, as is different from two-dimensional quantum wells or one-dimensional quantum wires, have very small number of atoms with $10^3 \sim 10^6$, and the number of atoms exposed to surface or interface of small quantum dots ranges from several to tens of percent of whole quantum dots. This leads to the enhancement of surface-related phenomena, such as persistent spectral hole-burning (PSHB) [19], fluorescence intermittency [20, 21], and

spectral diffusion [22]. Two-level system (TLS) has been successfully introduced to explain the anomalous temperature dependence of the homogeneous linewidth of impurity atoms in a glass matrix or dye molecules in a polymer [23]. However, there is only one report taking into account the matrix effects on the dephasing process in quantum dots, where small energy excitation in the TLS was proposed to explain the matrix-dependent homogeneous broadening of CuCl quantum dots [10]. If the interaction between quantum dots and the surrounding host plays a critical role on the dephasing mechanism of excitons confined in small quantum dots, it is also important to extend the study to quantum dots ranging from weak to strong confinement regimes with different matrices at low temperature limit.

In this work, we show the results of the heterodyne-detected accumulated photon echo experiment for CdSe quantum dots embedded in glass (CdSe-QDs/glass), CuBr quantum dots in glass (CuBr-QDs/glass), and CuBr quantum dots in NaBr (CuBr-QDs/NaBr) under weakest excitation intensity. An approach to very sharp optical spectrum from the time domain is a clever one, because the narrow homogeneous linewidth corresponds to long dephasing time which is easily accessible. It is verified that the Fourier-cosine transformation of the time-trace observed by the heterodyne-detected accumulated photon echo gives the persistent hole-burning spectrum [24]. The accumulated photon echo method with a phase modulation technique can detect signals with higher sensitivity under weaker excitation density than the other photon echo method, hardly suffering from the hole broadening [25]. Using this, we have examined carefully the temperature dependence of the homogeneous linewidth of CdSe quantum dots and CuBr quantum dots down to 0.6 K. The systematic investigation of quantum dots embedded in crystals or glass in weak to strong confinement regimes show the universal influence of surface-related effects and two-confined-acoustic-phonon scattering on the dephasing process of quantum dots in matrices.

Chapter II reviews fundamental physics of ultrafast spectroscopy of semiconductors. Typical two-beam pump-probe method, time-resolved luminescence, transient four-wave mixing, and accumulated photon echo method with phase-modulation technique are briefly

summarized.

Chapter III discusses the low-temperature exciton dephasing mechanism of CdSe-QDs/glass in strong confinement regime. The nonlinear temperature dependence of the homogeneous linewidth obtained from the heterodyne-detected accumulated photon echo is discussed in detail. The contribution of confined acoustic phonon and TLS is considered to explain the temperature broadening process. The low-frequency phonon modes are observed by Raman scattering measurement.

Chapter IV describes matrix dependence of the excitonic dephasing of CuBr-QDs/glass and CuBr-QDs/NaBr. The observed temperature dependence of the homogeneous linewidth clearly differs from each other below 15 K, showing the dephasing mechanism of excitons confined in quantum dots is highly sensitive to the surrounding host at very low temperature. We show the universal influence of confined phonons and surrounding matrices on the low-temperature dephasing process of very small semiconductor quantum dots by comparing with the result for CdSe and CuCl quantum dots.

Chapter V concludes this thesis.

References

[1] A. I. Ekimov, Al. L. Efros, and A. A. Onushchenko, Solid State Commun. **56**, 921 (1985).

[2] A. D. Yoffe, Adv. Phys. **42**, 173 (1993), and references therein.

[3] E. Biolatti, R. C. Iotti, P. Zanardi, and F. Rossi, Phys. Rev. Lett. **85**, 5647 (2000).

[4] N. H. Bonadeo, J. Erland, D. Gammon, D. Park, D. S. Katzer, and D. G. Steel, Science **282**, 1473 (1998).

[5] Pochung Chen, C. Piermarocchi, and L. J. Sham, Phys. Rev. Lett. **87**, 67401 (2001).

[6] A. Imamoglu, D. D. Awschalom, G. Burkard, D. P. DiVincenzo, D. Loss, M. Sherwin, and A. Smass, Phys. Rev. Lett. **83**, 4202 (1999).

[7] T. H. Stievater, Xiaoqin Li, D. G. Steel, D. Gammon, D. S. Katzer, D. Park, C. Piermarocchi, and L. J. Sham, Phys. Rev. Lett. **87**, 133603 (2001).

[8] H. Kamada, H. Gotoh, J. Temmyo, T. Takagahara, and H. Ando, Phys. Rev. Lett. **87**, 246401 (2001).

[9] Gang Chen, N. H. Bonadeo, D. G. Steel, D. Gammon, D. S. Katzer, D. Park, and L. J. Sham, Science **289**, 1906 (2000).

[10] M. Ikezawa and Y. Masumoto, Phys. Rev. B **61**, 12662 (2000).

[11] R. Kuribayashi, K. Inoue, K. Sakoda, V. A. Tsekhomskii, and A. V. Baranov, Phys. Rev. B **57**, 15084 (1998).

[12] P. Borri, W. Langbein, S. Schneider, U. Woggon, R. L. Sellin, D. Ouyang, and D. Bimberg, Phys. Rev. Lett. **87**, 157401 (2001).

[13] D. Gammon, E. S. Snow, B. V. Shanabrook, D. S. Katzer, and D. Park, Phys. Rev. Lett. **76**, 3005 (1996).

[14] Y. Toda, O. Moriwaki, M. Nishioka, and Y. Arakawa, Phys. Rev. Lett. **82**, 4114 (1999).

[15] K. Leosson, J. R. Jensen, J. M. Hvam, and W. Langbein, Phys. Stat. Sol. (b) **221**, 49 (2000).

[16] D. Birkedal, K. Leosson, and J. M. Hvam, Phys. Rev. Lett. **87**, 227401 (2001).

[17] K. Edamatsu, T. Itoh, K. Matsuda, and S. Saikan, Phys. Rev. B **64**, 195317 (2001).

[18] P. Palinginis and H. Wang, Appl. Phys. Lett. **78**, 1541 (2001).

[19] For review, see: Y. Masumoto, J. Lumin. **70**, 386 (1996).

[20] M. Nirmal, B. O. Dabbousi, M. G. Bawendi, J. J. Macklin, J. K. Trautman, T. D. Harris, and L. E. Brus, Nature **383**, 802 (1996).

[21] M. Sugisaki, H.-W. Ren, K. Nishi, and Y. Masumoto, Phys. Rev. Lett. **86**, 4883 (2001).

[22] S. A. Empedocles and M. G. Bawendi, Science **278**, 2114 (1997).

[23] For review, see: R. M. Macfarlane and R. M. Shelby, J. Lumin. **36**, 179 (1987); D. L. Huber, in *Dynamical Processes in Disordered Systems*, edited by W. M. Yen (Trans. Tech. Aedermannsdorf, Switzerland, 1989).

[24] S. Saikan, T. Nakabayashi, Y. Kanematsu, N. Tato, Phys. Rev. B **38**, 7777 (1988).

[25] W. H. Hesselink and D. A. Wiersma, Phys. Rev. Lett. **43**, 1991 (1979).

Chapter 2

Fundamentals

2.1 Introduction

When optical spectroscopy is combined with ultrafast laser pulses, it becomes a powerful tool for investigating a wide variety of phenomena related to relaxation and coherent dynamics in semiconductors. In this chapter, we describe the fundamental physics of ultrafast laser spectroscopy including pump-probe spectroscopy, transient four-wave mixing spectroscopy and accumulated photon echo spectroscopy.

Pump-probe spectroscopy is the most common form of ultrafast spectroscopy. If the dynamics in a pump-probe transmission experiment is longer than the dephasing times of the system, it determines incoherent carrier relaxation time T_1, *i.e.* population dynamics corresponding to the diagonal components of the density matrix [1]. *Four-wave mixing* or *photon echo* spectroscopy is well known method as the complementary technique to conventional site-selective spectroscopy such as hole-burning [2], fluorescence line narrowing, and single quantum dot spectroscopy [3–5], which access narrow homogeneous linewidth of quantum dots and extract it from inhomogeneously broadened optical spectra from the spectral domain. On the other hand, photon echo directly observes the dephasing time (T_2) which is inversely proportional to the homogeneous linewidth (Γ_h) of quantum dots. It enables us to access easily the very sharp homogeneous width from the time domain. When quantum dots have longer absorption recovery time compared with the laser repetition period, we can use the *accumulated photon echo* technique which is associated with

persistent hole-burning phenomena in the spectral domain [6]. Accumulated photon echo technique combined with *heterodyne-detection* method is known as one of the most sensitive methods of photon echo measurement, which can detect echo signal in ideally weakest excitation intensity [7]. We discuss the accumulated photon echo measurement combined with heterodyne-detection method in the end of this chapter.

2.2 Ultrafast Laser Spectroscopy

2.2.1 Pump-Probe Spectroscopy

Pump-probe spectroscopy is basic form for many ultrafast laser spectroscopy. In simplest degenerate pump-probe spectroscopy, the ultrafast pulse train is divided into two directions. The probe pulse is suitably delayed with respect to the pump pulse using an optical delay. A train of pump pulses excites the sample under investigation. The changes induced by the pump pulses (e.g. reflectivity, absorption, luminescence, etc.) are probed by the second pulse train (probe pulses). For suitably thin samples, the time resolution in pump-probe spectroscopy is limited only by the pulse width of the laser.

If we can ignore the *many-body effects* (e.g. band-gap renormalization or a change in the exciton binding energy) because of low excitation energy density, only *occupation effects*, or changes in the optical properties or transition rates brought about by the nonequilibrium occupation of certain states, need to be considered.

Here, for the photoexcited electron and hole distribution functions at energies E_e and E_h coupled by a photon energy $\hbar\omega$, we can express the change in the absorption coefficient as follows:

$$\Delta\alpha(\hbar\omega) = (1 - f_e - f_h)\alpha_0(\hbar\omega), \tag{2.1}$$

where $\alpha_0(\hbar\omega)$ is the absorption coefficient of the unexcited sample. If the absorption change, $\Delta\alpha(\hbar\omega)d$, is sufficiently small, the differential transmission spectrum (DTS) is given by

$$\text{DTS}(\hbar\omega) = [T(\hbar\omega) - T_0(\hbar\omega)]/T_0(\hbar\omega) = -\Delta\alpha(\hbar\omega)d, \tag{2.2}$$

where T and T_0 are the transmitted intensities with and without photoexcitation.

2.2.2   Luminescence Spectroscopy

In general, luminescence and pump-probe spectroscopy give useful complementary information. As in the case for DTS discussed in Section 2.2.1, the luminescence intensity at the photon energy $\hbar\omega$ is given by

$$L(\hbar\omega) = \alpha(\hbar\omega)f_\mathrm{e}f_\mathrm{h} \approx \alpha_0(\hbar\omega)f_\mathrm{e}f_\mathrm{h}. \tag{2.3}$$

The approximation is valid for sufficiently small change in the absorption coefficient induced by the photoexcitation. Therefore, the luminescence intensity is determined by the temporal evolution of the product of the appropriate electron and hole distribution functions. On the other hand, the DTS spectrum obtained by pump-probe spectroscopy is determined by the sum of the appropriate electron and hole distribution functions as in eq. (2.2).

2.2.3   Four-Wave Mixing Spectroscopy

In the two-beam *Degenerate* Four-wave mixing (DFWM) which is the simplest form of FWM spectroscopy, basic pump-probe configuration is used to produce FWM signal. First, the pump photons with wavevector $\boldsymbol{k}_1$ generate a coherent polarization in the sample. Second, the probe photons with wavevector $\boldsymbol{k}_2$ delayed by time τ arrive at the sample. Third, probe pulse with $\boldsymbol{k}_2$ is self-diffracted along the phase matched direction $\boldsymbol{k} = 2\boldsymbol{k}_2 - \boldsymbol{k}_1$ by an interference grating. The diffracted FWM signal is measured as a function of τ using a lock-in amplifier and an optical chopper (Fig. 2.1).

2.3   Formalization of Coherent Phenomena

In this chapter, we provide a framework for discussing coherent phenomena in semiconductors. First, we focus on coherent transient phenomena. The optical Bloch equations
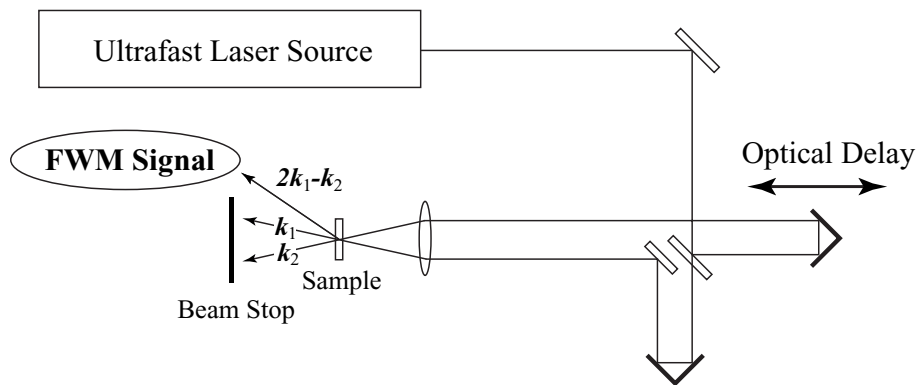
Figure 2.1: Schematic figure of the experimental setup for the degenerate two-beam FWM spectroscopy.

are introduced to describe the relaxation process for an ensemble of independent two-level systems with homogeneous and inhomogeneous broadening in the Markovian approximation. Second, we show the principle of accumulated photon echo together with the phase-modulated heterodyne method.

2.3.1 Two-Pulse Photon Echo

Density Matrix Formalism In an approximation, the electronic states in a semiconductor are considered as a two-level system. The density matrix formalism enables us to know statistical properties of the ensemble of two-level systems. Here, we define the density matrix operator as follows:

$$\rho = \sum_j P_j |\Psi_j\rangle\langle\Psi_j|. \tag{2.4}$$

For a two-level system with the ground state $|a\rangle$ and the excited state $|b\rangle$ the density operator can be written as

$$\rho = \begin{pmatrix} \rho_{bb} & \rho_{ba} \\ \rho_{ab} & \rho_{aa} \end{pmatrix} = \begin{pmatrix} n & p \\ p^* & 1-n \end{pmatrix}, \tag{2.5}$$

where $n = \rho_{bb}$, $1 - n = \rho_{aa}$, and $p = \rho_{ba}$. The density matrix (2.5) obeys the following

Liouville equation:

$$i\hbar\dot{\rho} = [H, \rho]. \tag{2.6}$$

The Hamiltonian of the system is given by

$$H = H_0 + H_1 + H_{\mathrm{R}}, \tag{2.7}$$

where H_0 is the unperturbed Hamiltonian, H_1 is the interaction Hamiltonian, and H_{R} is the relaxation Hamiltonian. H_0 and H_1 can be written as

$$H_0 = \begin{pmatrix} E_b & 0 \\ 0 & E_a \end{pmatrix}, \quad H_1 = \begin{pmatrix} 0 & \Delta_{ba} \\ \Delta_{ba}{}^* & 0 \end{pmatrix}, \tag{2.8}$$

where, Δ_{nl} means the interaction between the dibole moment and incident electrical field,

$$\Delta_{nl} = -e\,\boldsymbol{r}_{nl} \cdot \boldsymbol{E}(\boldsymbol{R}, t). \tag{2.9}$$

Assuming that the relaxation times in which the ensemble get back to thermal equilibrium are determined by the instantaneous distribution and polarization functions (Markovian approximation), the relaxation Hamiltonian is approximated by

$$[H_{\mathrm{R}}, \rho_{bb}] = -i\hbar\,\frac{\rho_{bb}}{T_1}, \quad [H_{\mathrm{R}}, \rho_{ba}] = -i\hbar\,\frac{\rho_{bb}}{T_2}, \tag{2.10}$$

where T_1 is the lifetime of the state $|b\rangle$ and T_2 is the transverse relaxation time (dephasing time). The transverse relaxation rate $1/T_2$ is given by the sum of the recombination rate $(1/T_1)$ and the pure dephasing rate $(1/T_2{}^*)$:

$$\frac{1}{T_2} = \frac{1}{2\,T_1} + \frac{1}{T_2{}^*}. \tag{2.11}$$

Using eqs. (2.6), (2.7) and (2.8), we obtain

$$\dot{n} + g_r\,n + \frac{i}{\hbar}(\Delta_{ba}\,p^* - p\,\Delta_{ba}{}^*) = 0, \tag{2.12}$$

$$\dot{p} + g\,p + \frac{i}{\hbar}(1 - 2n)\Delta_{ba} = 0, \tag{2.13}$$

where $g_r = 1/T_1$ and $g = (i\Omega + 1/T_2)$ with $\Omega = (E_b - E_a)/\hbar$. eqs. (2.12) and (2.13) are called *optical Bloch equations*.

In order to solve the optical Bloch equations, we expand the density n and polarization p into a Taylor series.

$$n = n^{(0)} + n^{(1)} + n^{(2)} + n^{(3)} + \cdots, \qquad (2.14)$$

$$p = p^{(0)} + p^{(1)} + p^{(2)} + p^{(3)} + \cdots. \qquad (2.15)$$

with $n^{(0)} = p^{(0)} = 0$. Using the initial conditions of $n = 0$ and $p = 0$, eq. (2.14) and (2.15) are expressed as follows:

$$\dot{p}^{(1)} + g\, p^{(1)} + (i/\hbar)\Delta_{ba} = 0, \qquad (2.16)$$

$$\dot{n}^{(2)} + g_r\, n^{(2)} + (i/\hbar)(\Delta_{ba}\, p^{*(1)} - p^{(1)}\Delta_{ba}{}^{*}) = 0, \qquad (2.17)$$

$$\dot{p}^{(3)} + g\, p^{(3)} - 2(i/\hbar)\Delta_{ba}\, n^{(2)} = 0. \qquad (2.18)$$

Four-Wave Mixing Here, we consider the standard two-beam FWM experiment (Fig. 2.1) in which first pulse along $\boldsymbol{k}_1$ direction and second pulse along $\boldsymbol{k}_2$ direction create a grating in the sample. In this case, the FWM signal is obtained as the self-diffracted signal of the second pulse in the direction $\boldsymbol{k} = 2\boldsymbol{k}_2 - \boldsymbol{k}_1$. With the rotating-wave approximation, the incident electric field can be expressed as

$$E(t, \boldsymbol{R}) = E_1(t, \boldsymbol{R})\exp\left[i(\boldsymbol{k}_1 \cdot \boldsymbol{R} - \omega t)\right] + E_2(t - t_{21}, \boldsymbol{R})\exp\left[i(\boldsymbol{k}_2 \cdot \boldsymbol{R} - \omega t)\right], \qquad (2.19)$$

where incident pulse along $\boldsymbol{k}_2$ is delayed by time delay t_{21} with respect to the pulse along $\boldsymbol{k}_1$. $E_1(t, \boldsymbol{R})$ and $E_2(t, \boldsymbol{R})$ are the electric field pulse shapes of the first and second incident pulse.

Equations (2.16), (2.17) and (2.18) can be solved sequentially using eqs. (2.9) and (2.19). The FWM signal is related to $p_{221}{}^{(3)}$ which is the third-order polarization calculated only for the $2\boldsymbol{k}_2 - \boldsymbol{k}_1$ direction. When the electric field pulse is approximated by the δ-function, the third-order polarization $p_{221}{}^{(3)}$ is given by

$$
\begin{aligned}
p_{221}{}^{(3)} =\ & -i\,(e|r_{ba}|/\hbar)^3\exp(-i\omega t)\,\exp[i\,(2\boldsymbol{k}_2 - \boldsymbol{k}_1)\cdot \boldsymbol{R}] \\
& \times \Theta(t_{21})\Theta(t - t_{21})\exp\left[-i(\Omega - \omega)t - \frac{t - 2t_{21}}{T_2}\right],
\end{aligned} \qquad (2.20)
$$

where Θ is the Heaviside step function. Assuming the inhomogeneously broadened system, the macroscopic polarization of the ensemble needs to be integrated over the inhomogeneous distribution $g(\Omega_0)$,

$$g(\Omega, \Omega_0, \Gamma_{\text{in}}) = \frac{1}{\sqrt{\pi}\,\Gamma_{\text{in}}} \exp\left[-\frac{(\omega - \omega_0)^2}{\delta\omega^2}\right], \tag{2.21}$$

where Γ_{in} is the inhomogeneous linewidth, and Ω_0 is central frequency. Then the macroscopic polarization is given by

$$\begin{aligned}
p_{221}^{(3)} &\propto \int_{-\infty}^{\infty} d\Omega\, g(\Omega,\, \Omega_0, \Gamma_{\text{in}}) p_{221}^{(3)} \\
&= \sqrt{\pi}\,\Gamma_{\text{in}} \exp\left[-\frac{1}{4}\Gamma_{\text{in}}^2 (t - 2t_{21})^2\right] e^{-i(\omega+\Omega_0)\,(t-2t_{21})}.
\end{aligned} \tag{2.22}$$

Therefore, the time-resolved FWM signal in $2\boldsymbol{k}_2 - \boldsymbol{k}_1$ direction is written as

$$S_{221}{}^{(3)} = |p_{221}{}^{(3)}|^2 = \exp\left[-\frac{(t - 2t_{21})^2}{2\tau_{\text{in}}^2}\right] \exp\left(-\frac{2t}{T_2}\right), \tag{2.23}$$

where $\Gamma_{\text{in}} = \tau_{\text{in}}{}^{-1}$. Finally, the time-integrated FWM signal in $2\boldsymbol{k}_2 - \boldsymbol{k}_1$ direction is obtained as a function of time delay t_{21}

$$I_{221}{}^{(3)}(\tau) = \int_{-\infty}^{\infty} dt\, S_{221}{}^{(3)}(t) \propto \exp\left(-\frac{4\tau}{T_2}\right). \tag{2.24}$$

Equation (2.24) indicates that four times of decay time of two-pulse photon echo signal corresponds the dephasing time T_2.

2.3.2 Accumulated Photon Echo

Two-beam FWM, or photon echo, is a powerful tool to access very sharp homogeneous spectra due to the direct observation of long dephasing time from the time domain as shown in eq. (2.24). However, transient photon echo method has several disadvantages. First, strong excitation pulses are needed because of the third-order nonlinear optical process of the photon echo which results in the additional broadening process coming from carrier-carrier scattering process. Second, it is difficult to detect photon echo signals in scattering materials because the scattered pump beam overloads the detector.

As an improved technique of detecting photon echo, Hesselink and Wiersma have developed accumulated photon echo method with heterodyne detection technique [7]. The heterodyne-detected accumulated photon echo (HAPE) measurement is known as one of the most sensitive methods of photon echo measurement. It enables us to observe the photon echo signal under the very low excitation condition free from dephasing due to the mutual collisions of carriers. The unique requirement for its applicability is the presence of a longer absorption recovery time compared with the laser repetition period [6, 7]. Therefore, persistent spectral hole-burning phenomena in quantum dots automatically satisfy the requirement for the applicability of the accumulated photon echo. The accumulation of population grating is shown in Fig. 2.2 schematically.

We will derive the expression for the delay-time dependence of the signal intensity of phase-modulated two-beam accumulated photon echo measurements in the following. The pump beam and the probe beam are assumed to have wave vectors of $\boldsymbol{k}_1$ and $\boldsymbol{k}_2$, respectively. The phase of the pump beam is assumed to be modulated at a frequency of f with an amplitude of M. The $2f$ component of the probe intensity is detected as a signal by lock-in detection. The accumulated photon echo can be considered as a repetition of a three-pulse photon echo. In the three-pulse photon echo, the incident electric field can be expressed as

$$
\begin{aligned}
E(t, \boldsymbol{R}) = E_1(t, \boldsymbol{R})\, e^{i(\boldsymbol{k}_1 \cdot \boldsymbol{R} - \omega t)} \\
+\quad E_2(t - t_{21}, \boldsymbol{R}) e^{i(\boldsymbol{k}_2 \cdot \boldsymbol{R} - \omega t)} + E_3(t - t_{31}, \boldsymbol{R}) e^{i(\boldsymbol{k}_3 \cdot \boldsymbol{R} - \omega t)},
\end{aligned} \tag{2.25}
$$

where E_1, E_2 and E_3 are the electric field pulse shapes of the first, second and third incident pulses, respectively. The t_{21} (t_{31}) is the delay time between the second (third) and first pulses. Assuming a one-dimensional case for simplification, eq. (2.25) becomes

$$
\begin{aligned}
E(t, z) = E_1(t, z)\, e^{i(k_1 z - \omega t)} \\
+\quad E_2(t - t_{21}, z)\, e^{i(k_2 z - \omega t)} + E_3(t - t_{31}, z)\, e^{i(k_1 z - \omega t)},
\end{aligned} \tag{2.26}
$$

where $k_3 = k_1$ was used. Just like the case of the two-pulse photon echo, eqs. (2.16) $\sim$
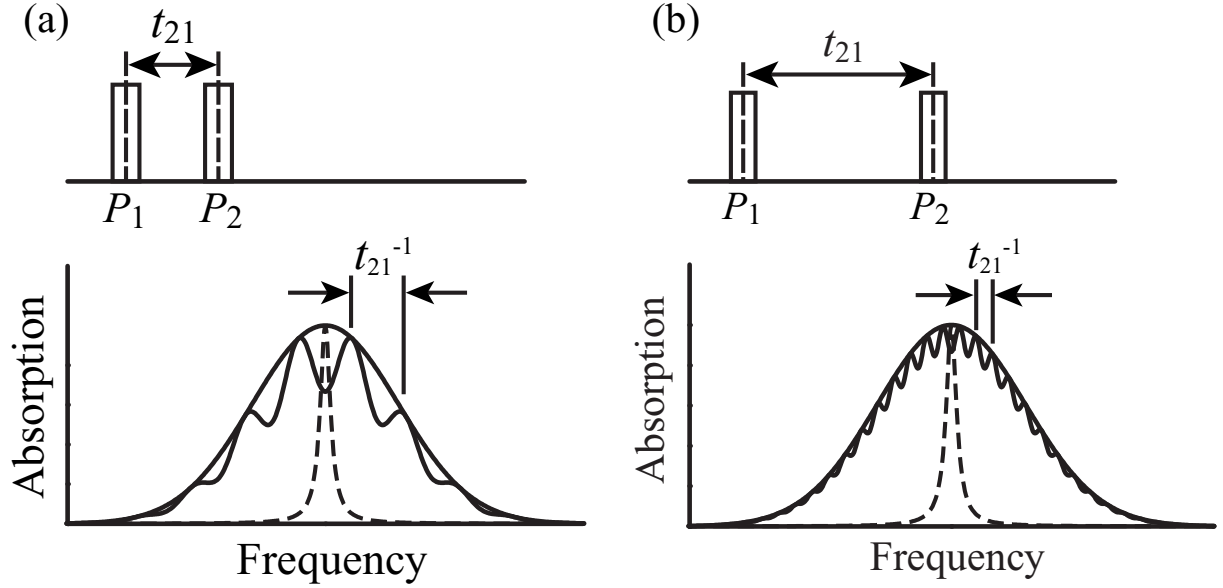
Figure 2.2: Schematic figure of population grating formation. Two incident degenerate light pulses (P_1 and P_2) creates the spectral interference pattern in the inhomogeneous broadened absorption spectrum. The t_{21} denotes (a) short and (b) long time delay between P_1 and P_2. Dashed lines show the homogeneous spectrum with the linewidth of $\Gamma_\mathrm{h} = 2\hbar/T_2$.

(2.18) have to be solved sequentially in order to obtain the third-order polarization along the direction k_2.

First, $p^{(1)}(t)$ can be obtained from eqs. (2.9), (2.16) and (2.26)

$$p^{(1)}(t) = \int_{-\infty}^{t} d\tau \, e^{-\xi(t-\tau)} f(\tau) e^{-i\omega t}, \tag{2.27}$$

where $\xi \equiv g - i\omega$, and

$$f(t) = \frac{er_{ba}}{i\hbar} \left[E_1(t, \, z) \, e^{ik_1 z} + E_2(t - t_{21}, \, z) \, e^{ik_2 z} + E_3(t - t_{31}, \, z) \, e^{ik_1 z} \right]. \tag{2.28}$$

Considering only the $k = k_2 - k_1$ component, the density $n^{(2)}$ can be obtained from eqs. (2.17) and (2.28)

$$n_{21}^{(2)} = \int_{-\infty}^{t} d\tau' \, e^{-g_\mathrm{r}(t-\tau')} f_{21}(\tau'), \tag{2.29}$$

where

$$f_{21}(t) = \frac{e^2 r_{ba}^2}{\hbar^2} e^{i(k_2-k_1)z} \times \int_{-\infty}^{t} d\tau \Big\{ E_2(t - t_{21}, z) E_1^*(\tau, z)$$

$$+ E_1^*(t, z) E_2(\tau - t_{21}, z) \Big\} e^{-\xi(t-\tau)}. \qquad (2.30)$$

Finally, the third-order polarization in the direction $k = k_2 - k_1 + k_1 = k_2$ is obtained from eqs. (2.18) and (2.29)

$$p_{211}^{(3)} \propto -2i \left(\frac{e\, r_{ba}}{\hbar}\right)^3 e^{ik_2 z} \int_{-\infty}^{t} d\tau \int_{-\infty}^{\tau} d\tau' \int_{-\infty}^{\tau'} d\tau'' e^{-i\omega(t-\tau)} e^{-g_r(\tau-\tau')-\xi(t-\tau+\tau'-\tau'')}$$

$$\times \ [E_3(\tau - t_{31}, z)E_2(\tau' - t_{21}, z)E_1^*(\tau'', z) + E_3(\tau - t_{31}, z)E_2(\tau'' - t_{21}, z)E_1^*(\tau', z)].$$

$$(2.31)$$

By using a transformation of variables in eq. (2.31), and by the integration over the inhomogeneous distribution function, eq. (2.21), we obtain the macroscopic polarization

$$P(t) = i \int_0^{\infty} d\tau \int_0^{\infty} d\tau' \int_0^{\infty} d\tau'' e^{-\tau'/T_1 - (\tau+\tau'')/T_2} \Big\{ E_3(t - \tau - t_{31}, z)E_2(t - \tau - \tau' - t_{21}, z)$$

$$\times E_1^*(t - \tau - \tau' - \tau'', z)\exp\Big[-\frac{(\tau - \tau'')^2\Gamma_{in}^2}{4} - i\Omega_0(\tau - \tau'')\Big]$$

$$+ E_3(t - \tau - t_{31}, z)E_2(t - \tau - \tau' - \tau'' - t_{21}, z)E_1^*(t - \tau - \tau', z)$$

$$\times \exp\Big[-\frac{(\tau + \tau'')^2\Gamma_{in}^2}{4} - i\Omega_0(\tau + \tau'')\Big] \Big\},$$

$$(2.32)$$

where Ω_0 is central frequency of the inhomogeneously broadened spectrum with the width of Γ_{in}. The photo-detected signal is expressed as $\int_{-\infty}^{\infty} d\omega |E_4(\omega, l)|^2$ where l is the sample thickness. The $E_4(\omega, z)$ is the field spectrum at the time of fourth-incident-pulse arrival, satisfying linearized Maxwell equation

$$\frac{dE_4(\omega, z)}{dz} = -\frac{1}{2}\gamma(\omega)E_4(\omega, z) - iP(\omega, z)\exp[-i(\omega + \omega_l)t_4], \qquad (2.33)$$

where $\gamma(\omega)$ is the absorption spectrum and ω_l the central frequency of the laser. Using eqs. (2.32) and (2.32), and assuming a sufficiently long T_1, we obtain the expression for

the signal strength of HAPE [8]

$$
\begin{aligned}
S \;=\; & \mathrm{Re} \int_0^\infty d\tau \int_{-\infty}^\infty d\tau'' G_R(\tau - t_{21}) G_W^*(\tau'' - t_{21}) \\
& \times \exp\!\left[-\frac{\tau + |\tau''|}{T_2} - \frac{\Gamma_{\mathrm{in}}^2 (\tau - \tau'')^2}{4} - i\Delta\omega(\tau - \tau'') \right],
\end{aligned}
\qquad (2.34)
$$

where $\Delta\omega$ is the frequency detuning of the excitation light, and G_W and G_R denotes the effective correlation function of the write-in process of the population grating and read-out process of the burned spectral hole through the heterodyne detection, respectively. Assuming the δ-function-like excitation pulses, extremely broad inhomogeneous width, and equal central frequencies of G_W and G_R, eq. (2.34) can be modified as

$$
S = \mathrm{Re} \int_0^\infty d\tau \, G_R(\tau - t_{21}) G_W^*(\tau - t_{21}) \exp\!\left(-\frac{2\,\tau}{T_2} \right).
\qquad (2.35)
$$

If a modulation frequency is higher than the ground-state recovery rate, G_W should be understood as the time-averaged correlation function. On the other hand, we need not make time-averaging for G_R because G_R is associated with the induced nonlinear polarization. Therefore, G_W and G_R become [9]

$$
G_W^*(\tau - t_{21}) \;=\; \langle \exp(iM\sin ft) \rangle_{\mathrm{av}} G^*(\tau - t_{21}) = J_0(M)\, G^*(\tau - t_{21}),
\qquad (2.36)
$$

$$
G_R(\tau - t_{21}) \;=\; \exp(-iM\sin ft)\, G(\tau - t_{21}),
\qquad (2.37)
$$

where G is the field correlation function of the excitation light, f is the modulation frequency, J_n is the n-th order Bessel function, and M is the modulation depth. The product of $J_0(M)$ and $\exp(-iM\sin ft)$ becomes

$$
\begin{aligned}
J_0(M)\exp(-iM\sin ft) &= J_0(M) \sum_{n=-\infty}^\infty J_n(M)\cos nft \\
&= J_0(M)\left[J_0(M) + \sum_{n=1}^\infty \{(-1)^n J_n(M)\cos nft + J_n(M)\cos nft\} \right] \\
&= J_0(M)\left\{ J_0(M) + 2J_2(M)\cos 2ft + 2J_4(M)\cos 4ft + \cdots \right\},
\end{aligned}
\qquad (2.38)
$$

where we used the following formula:

$$
\exp(i z \sin\theta) = \sum_{n=-\infty}^\infty J_n(z) \exp(i n\,\theta).
\qquad (2.39)
$$
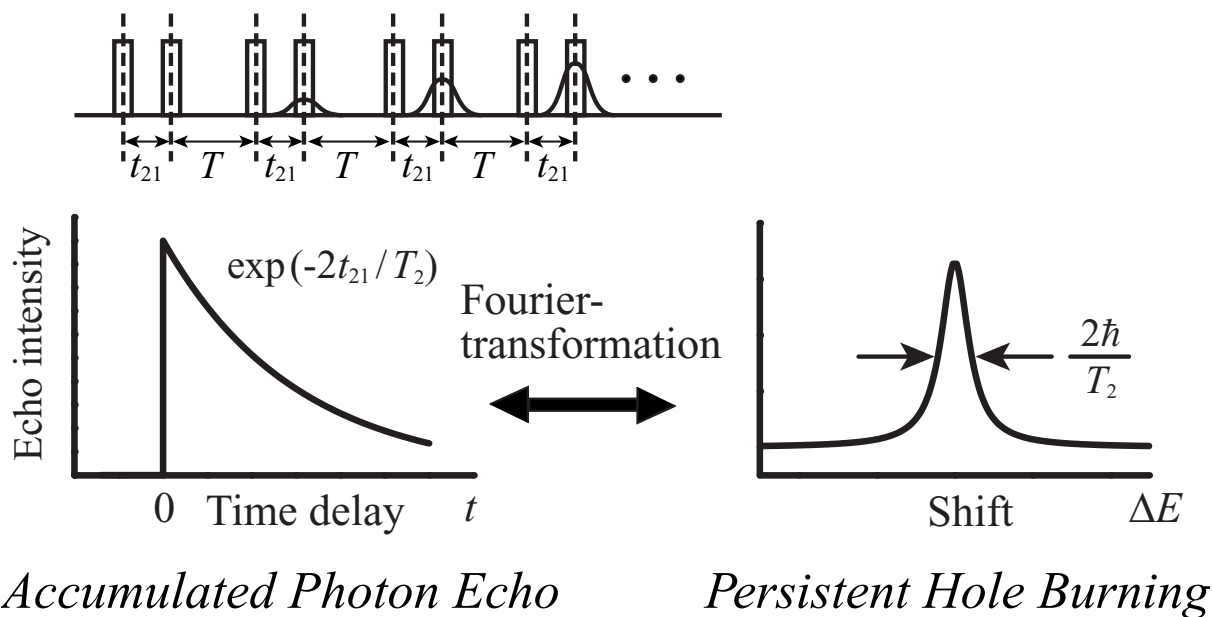
Figure 2.3: Schematic drawing of the relation between the time-trace signal of HAPE and PSHB.

Therefore, from eq. (2.35) $\sim$ (2.38), we obtain the expression of the signal intensity of the accumulated photon echo with heterodyne-detection method

$$I_{\text{echo}}(t,\, t_{21}) \propto \exp\left(-\frac{2\, t_{21}}{T_2}\right) J_0(M) \times \{J_0(M) + 2J_2(M)\cos 2ft + \cdots\}. \qquad (2.40)$$

Finally, the lock-in-detected echo signal as the $\cos 2ft$ component is given by

$$I_{\text{echo}}(t_{21}) \propto J_0(M)J_2(M)\exp(-2\, t_{21}/T_2), \qquad (2.41)$$

where I_{echo} is non-zero only for positive time delays ($t_{21} > 0$) and is zero for negative time delays ($t_{21} < 0$). Equation (2.41) indicates that the accumulated photon echo signal is the dephasing time T_2 is given by twice of the decay time of the accumulated photon echo signal.

The schematic drawing of the accumulation effect of the population grating is shown in Fig. 2.2. The accumulation effect corresponds to the persistent spectral hole-burning (PSHB) process in the spectral domain. In the case of PSHB, if we assume the extremely wide inhomogeneous broadening, and consider that the burning process and reading process are well distinguished temporally, the hole-burning spectrum is given by the Fourier

transform of the accumulated photon echo signal [6]

$$H(\Delta\omega) = \int_0^\infty d\tau \cos\Delta\omega\,\tau\,S(\tau),\tag{2.42}$$

where $\Delta\omega$ is the detuning frequency of the probe beam with respect to the pump beam, $S(\tau)$ is the signal strength of the accumulated photon echo. The relation between the time-trace of the accumulated photon echo signal and its Fourier-transformed signal is schematically shown in Fig. 2.3.

References

[1] For review, see: J. Shah, in *Ultrafast Spectroscopy of Semiconductors and Semiconductor Nanostructures* (Springer, Berlin, 1996).

[2] K. Naoe, L. G. Zimin, and Y. Masumoto, Phys. Rev. B **50**, 18200 (1994).

[3] D. Gammon, E. S. Snow, B. V. Shanabrook, D. S. Katzer, and D. Park, Phys. Rev. Lett. **76**, 3005 (1996).

[4] Y. Toda, O. Moriwaki, M. Nishioka, and Y. Arakawa, Phys. Rev. Lett. **82**, 4114 (1999).

[5] K. Leosson, J. R. Jensen, J. M. Hvam, and W. Langbein, Phys. Stat. Sol. (b) **221**, 49 (2000).

[6] S. Saikan, T. Nakabayashi, Y. Kanematsu, and N. Tato, Phys. Rev. B **38**, 7777 (1988).

[7] W. H. Hesselink and D. A. Wiersma, Phys. Rev. Lett. **43**, 1991 (1979).

[8] S. Saikan, H. Miyamoto, Y. Tosaki, and A. Fujiwara, Phys. Rev. B **36**, 5074 (1987).

[9] S. Saikan, K. Uchikawa, and H. Ohsawa, Opt. Lett. **16**, 10 (1991).

Chapter 3

Optical Dephasing of Excitons in CdSe Quantum Dots

3.1 Introduction

So far CdSe quantum dots in the strong confinement regime, fabricated by many growth methods, such as ion aggregation growth in glass and polymers, and by chemical growth in solvents and polymers, have been actively investigated. Spectral hole burning (SHB) and photon echo measurements have been used to observe the homogeneous broadening (Γ_h) of the quantum levels buried in the inhomogeneously broadened absorption spectra of CdSe quantum dots [1–6]. However, as a probable result of variation of the dot-matrix interface, the homogeneous width varies from sample to sample.

At first, most studies have been done by means of SHB, where the full-width at half-maximum (FWHM) of the hole gives twice of the FWHM ($2\Gamma_h$) of the homogeneous spectrum. A wide variety of values $2\Gamma_h$, such as 90 meV [1], 17 meV [2], and 8 meV [3], have been reported [4]. Single quantum dot spectroscopy observed the resolution-limited luminescence spectra of CdSe/ZnS core/shell quantum dots as sharp as 0.1 meV [7]. In the time-domain, Mittleman has reported the result of three-pulse photon echo measurement of chemically synthesized CdSe quantum dots dispersed in a free-standing polymer film [6]. The dephasing times varying from 85 fs for 2-nm quantum dots to 270 fs for 4-nm quantum dots have been reported. They classified temperature-dependent electronic dephasing into

three dynamical processes: the coupling to a heat bath of low-frequency phonon modes, the lifetime broadening accompanying fast energy relaxation process of carriers, and the scattering process from impurity or defect sites. Recently, Palinginis has reported nonlinear temperature dependence of homogeneous linewidth in CdSe/ZnS core/shell quantum dots by using high-resolution spectral hole burning [8]. The observed quadratic temperature dependence of the homogeneous width was explained by two-phonon Raman process involving simultaneous absorption and emission of confined phonons. At low temperature, homogeneous linewidth of 32 μeV was observed in this experiment. As a result of different data on different samples, the present knowledge on the homogeneous linewidth is in confusion.

The one reason of these discrepancies arise from difference of the experimental technique. In transient hole-burning and transient photon echo spectroscopy, the temperature broadening of confined excitons suffers from hole-broadening process by intense excitation pulses which creates many carriers in quantum dots. In single quantum dot spectroscopy, the linewidth is too sharp to be studied with sufficient spectral resolution.

In chis chapter, we show the results of the detailed study of the temperature dependence of the homogeneous linewidth of high-quality CdSe quantum dots in glass (CdSe-QDs/glass) with long T_1 of 120 ps under weakest intensity by the heterodyne-detected accumulated photon echo method. This method can detect signals with higher sensitivity under weaker excitation density than the other photon echo method, hardly suffering from the hole broadening process as described in Chapter 2. We have measured the Raman scattering spectra for different size of CdSe quantum dots in order to clarify the presence of confined acoustic phonons.

3.2   Cadmium Selenide

Cadmium selenide (CdSe) is an important II-VI compound semiconductor because of its suitable direct band gap ($\approx$ 1.75 eV at room temperature) and high photosensitivity. In this section, we will summarize the physical properties of CdSe such as crystal structure, band structure and optical properties.

3.2.1   Bulk CdSe

Lattice structure   Cadmium selenide is a II-VI compound semiconductor which crystal-lized in different structures. The most common form is the hexagonal wurtzite structure. The other two lattice forms are cubic zincblende structures and a high pressure NaCl-type phase [9]. Each selenide ion is surrounded by four ions of cadmium placed on the corners of a tetrahedron. The structure has a polar direction along the c-axis.

Band structure   The electronic structure of CdSe quantum dots has been studied the-oretically with effective mass approximation models [10, 11]. The conduction band comes from the 5s states of cadmium. The energy minimum is located at the center of the Bril-louin zone (Γ-point). A second minimum higher by about 1.7 eV is located at the A-point. The conduction band has Γ_7-symmetry for $k = 0$ with quantum number $J_z = 1/2$.

The valence band results from the $4p$ states of selenium, having its maximum at the Γ-point, too, which leads to a direct band gap. Further maxima are situated at A ($\approx$ -0.2 eV) and H ($\approx$ -0.4 eV). Because the p atomic orbitals are degenerate, the interaction between Se 4p orbitals in the crystal field and the effect of spin-orbit coupling contribute to the valence band splitting at $k = 0$ into three sub-bands (A, B and C-bands). The A-band has Γ_9-symmetry and the quantum number $J_z = 3/2$, while B and C have Γ_7-symmetry with $J_z = 1/2$. The schematic figure of the band structure is shown in Fig. 3.1. Calculated band structure of CdSe is also shown in Fig. 3.2.
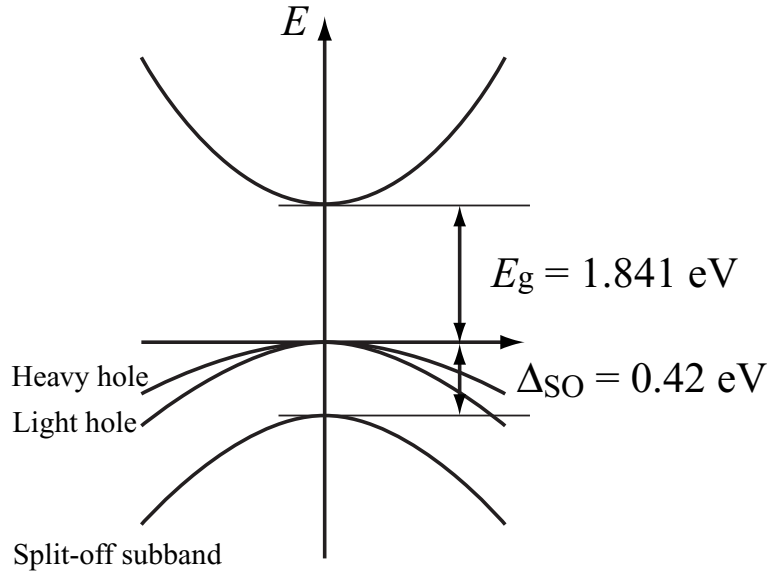
Figure 3.1: Schematic diagram of energy band structure of bulk CdSe.

3.2.2   Quantum Dot

When the size of quantum dots is comparable or smaller than the exciton Bohr radius of bulk semiconductor ($R/a_B \ll 1$), the individual particle confinement occurs. This is the case called a strong confinement regime. CdSe quantum dot is a typical model for the strong confinement due to a large Bohr radius, $a_B \approx 5.6$ nm.

As described in the previous section, the top of valence bands in CdSe quantum dots is degenerate at $\boldsymbol{k} = 0$. The degeneracy of the top valence bands brings about different effective masses, leading to so-called heavy- and light-hole bands. Due to the quantum confinement in CdSe quantum dots, strong mixing of the valence band states and a removal of the degeneracy occur.

Physical property		Numerical value
lattice structure		hexagonal (wurtzite)
density		$5.81\,\mathrm{g/cm^2}$
melting point		$1514\,°C$
bandgap energy (1.8 K)	$E_g{}^{\mathrm{A}}\ (\Gamma_9 v \to \Gamma_7 c)$	1.841 eV
	$E_g{}^{\mathrm{B}}\ (\Gamma_7 v \to \Gamma_7 c)$	1.866 eV
	$E_g{}^{\mathrm{C}}\ (\Gamma_7 v \to \Gamma_7 c)$	2.274 eV
bandgap energy (293 K)	$E_g{}^{\mathrm{A}}\ (\Gamma_9 v \to \Gamma_7 c)$	1.751 eV
	$E_g{}^{\mathrm{B}}\ (\Gamma_7 v \to \Gamma_7 c)$	1.771 eV
	$E_g{}^{\mathrm{C}}\ (\Gamma_7 v \to \Gamma_7 c)$	2.176 eV
free exciton transition energy (1.8 K)	$E_{g,\,\mathrm{ex}}{}^{\mathrm{A}}(n=1)$	1.826 eV
	$E_{g,\,\mathrm{ex}}{}^{\mathrm{B}}(n=1)$	1.851 eV
	$E_{g,\,\mathrm{ex}}{}^{\mathrm{C}}(n=1)$	2.259 eV
conduction band, effective mass		$0.13\ m_0$
valence band, effective mass		$0.45\ m_0$
exciton Bohr radius		5.6 nm
exciton binding energy	$E_{\mathrm{b}}^{\mathrm{A}}$	13.2 meV
	$E_{\mathrm{b}}^{\mathrm{B}}$	14.9 meV
lattice constant (hexagonal modification)	a	0.43 nm
	c	0.70 nm
phonon wavenumbers	$\nu_{\mathrm{LO}}(\Gamma_1)$	$211\ \mathrm{cm^{-1}}$ (26 meV)
	$\nu_{\mathrm{TO}}(\Gamma_5)$	$211\ \mathrm{cm^{-1}}$ (26 meV)

Table 3.1: Physical parameters of bulk CdSe.
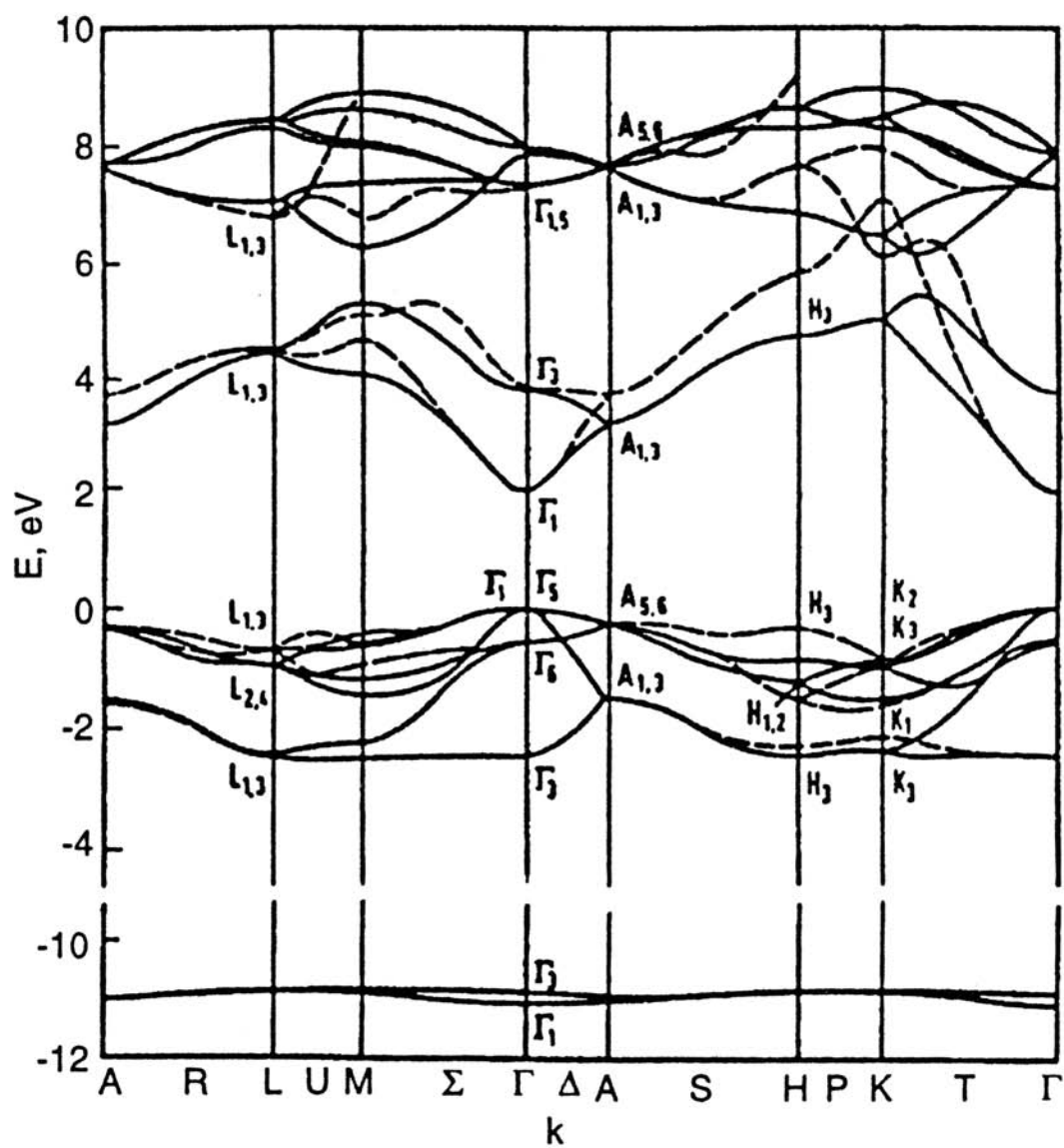
Figure 3.2: Band structure of hexagonal CdSe [12].

3.3 Samples

The samples studied are CdSe quantum dots embedded in $GeO_2 : Na_2O$ glass which were grown by the double heat treatment procedure. First, the mixture of GeO_2, Na_2CO_3 and CdSe powder was melted at 1200 °C and then quenched to avoid nucleation of CdSe crystals. Na_2CO_3 was used to decrease the melting point. Second, quantum dots were grown in the glass matrix by annealing process. The size of quantum dots was controlled by the heat-treatment temperature and the tratment time. In this experiment, the annealing temperature was $500\,°C \sim 600\,°C$ and the annealing time was 10 minutes ~ 24 hours. The average radius increased for the higher temperature and the longer treatment time.

Figure 3.3 shows absorption spectra of them at 2 K. The absorption peaks show large blue shift because of quantum confinement effect. The average radii of the samples are determined by X-ray scattering at small angles as $R = 2.3$, 2.5, 2.7 and 3.6 nm. The lowest energy absorption peak is ascribed to the $1S_{3/2}1S_e$ transition.
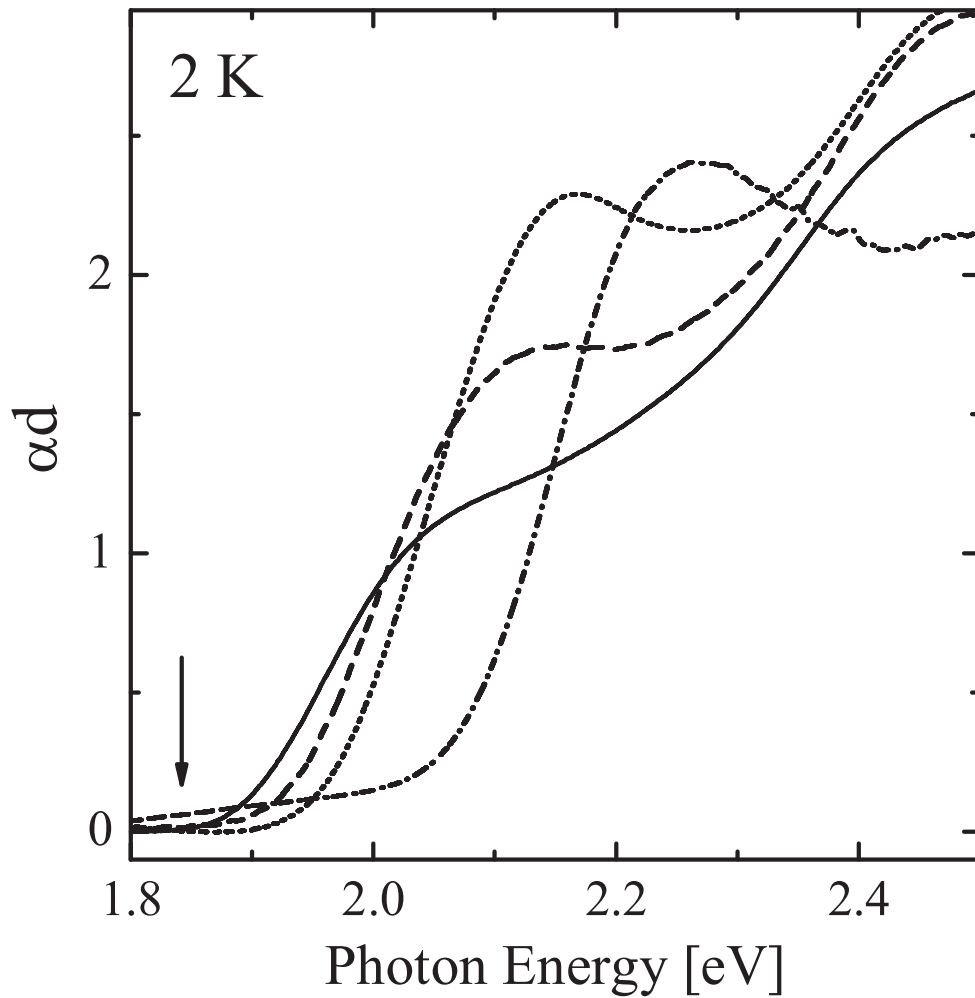
Figure 3.3: Absorption spectra of CdSe-QDs/glass with the following radii: 2.3 (dash-dotted line), 2.5 (dotted line), 2.7 (dashed line), and 3.6 nm (solid line) at 2 K. The vertical arrow indicates absorption energy of the lowest exciton transition of bulk CdSe (1.841 eV).

3.4 Carrier Dynamics in CdSe Quantum Dots

In this chapter, we discuss carrier dynamics of CdSe-QDs/glass. Usually, zero-dimensional quantum dots have so large surface-to-volume ratio compared to higher dimensional semiconductor, that the relaxation mechanism of excitons confined in quantum dots can be affected by carrier transfer to the surface or matrix. Previously, it was reported that chemically synthesized CdSe quantum dots show large Stokes-shifted exciton luminescence which was explained by relaxation from the initial exciton state into a surface trapped state of quantum dots [3]. In order to determine the carrier lifetime of such quantum dots, we should investigate both time-resolved luminescence and time-resolved induced absorption. As shown in eq. (2.2) and (2.3), exciton luminescence is proportional to the number of pairs of electrons and holes, while the induced absorption is determined by the sum of electron and hole number. If the electron and the hole are decomposed into different layers such as type-II quantum wells [13, 14], difference between time-resolved luminescence and induced absorption should be observed.

3.4.1 Experimental Setup

For the measurement of time-resolved luminescence and time-resolved induced absorption, an optical parametric amplifier (OPA) pumped by 200 kHz regeneratively amplified output of a 82 MHz femtosecond Ti:sapphire laser was used as an excitation source. The pulse width of the OPA output is 280 fs. In order to improve the site-selectivity, a diffraction grating was used to eliminate the additional broadening of the OPA output pulse ($\Delta\lambda_{\mathrm{exc}} \approx 10$ nm). Using the diffraction grating and a slit, narrower spectrum with full-width at half maximum of 1 nm was obtained.

For the time-resolved induced absorption measurement, pump-probe setup was used to observe the temporal change of differential transmission. Pump-probe experiment was performed in transmission configuration, and the signal was detected by lock-in amplifier together with an optical chopper. The probe beam power was attenuated by neutral-

density filter into 1/10 with respect to the pump beam power. Time-resolved luminescence was measured by means of a synchroscan streak camera in conjunction with a subtractive dispersion double monochromator. The time resolution of the streak camera system was 25 ps. For spectral measurement, nitrogen-cooled charge-coupled device (CCD) was used. The sample used in this experiment was 3.6 nm-radius CdSe-QDs/glass which was directly immersed in superfluid helium at 2 K in an optical cryostat. Temperature-dependent measurement of luminescence was performed by using gas-flow type optical cryostat.

3.4.2   Results and Discussion

Figure 3.5 (a) shows linear absorption and luminescence spectra of CdSe-QDs/glass with radius of 3.6 nm obtained at 2 K. Both these spectra are inhomogeneously broadened. The lowest energy absorption peak is ascribed to the $1S_{3/2}1S_e$ transition. The peak energy of the luminescence spectrum is located around 1.894 eV which is about 150 meV lower than the lowest exciton transition energy, 2.023 eV observed in the absorption spectrum. The Stokes shifted luminescence peak suggests that the band-edge emission is not from the free exciton state but from some localized state of the surface of quantum dots [15, 16]. In Fig. 3.5 (b), time-resolved induced absorption (temporal change of the differential transmission) observed by pump-probe experiment with the excitation energy of 2.023 eV is shown. The obtained signal is well fitted by a linear combination of two exponential decays with fast and slow decay time constant of 120 ps and 1.65 ns, respectively. Figure 3.5 (c) shows time-resolved photoluminescence signal which is also fitted by the double-exponential with the decay time of 120 ps and 800 ps for the fast and slow decay component, respectively. Although the fast decay time constant has almost the same value, the slow decay time constant in the pump-probe time trace is about 3.0 times longer than that in the time trace or luminescence. The amplitude of the fast decay component is dominant in the luminescence decay but is minor in the pump-probe decay. This disagreement is also observed in CuCl and CuBr quantum dots when the electron-hole spatial separation takes
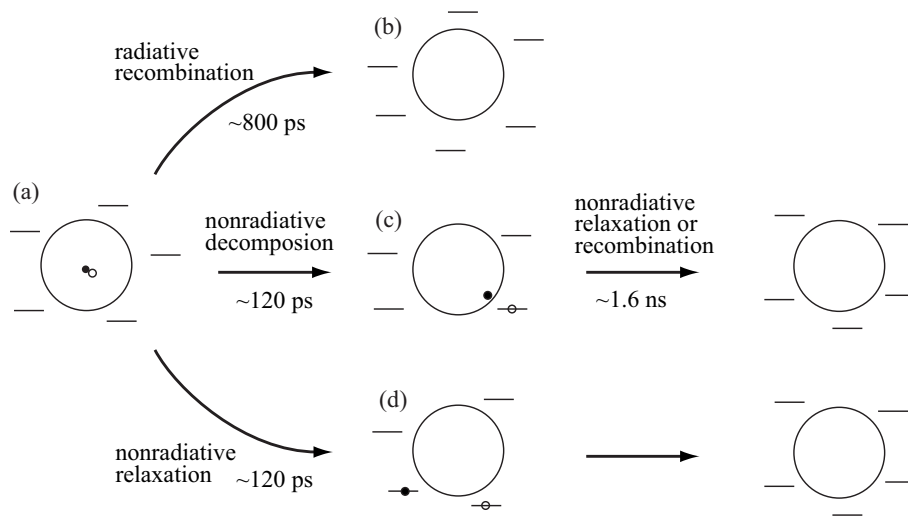
Figure 3.4: Radiative or nonradiative relaxation mechanism of carriers including exciton decomposition process in CdSe-QDs/glass [17].

place [17].

Schematic figure of relaxation mechanisms of excitons in CdSe quantum dots were shown in Fig. 3.4. As shown in Fig. 3.5 (a), the luminescence spectrum has shown large Stokes shift of 150 meV which indicates the relaxation of excitons into some localized states at surface of quantum dots. The detection photon energy was set at 2.023 eV which is in higher-energy tail of the luminescence spectrum in order to avoid the contribution of luminescence from these localized excitons. In this case, the identical initial fast decay component and succeeding large difference of slow decay component between the time-resolved luminescence and pump-probe signal shows the decomposition process of free excitons where electron trapping at the surface of quantum dots and hole tunneling into traps in the glass host occur with decay time of $\sim$ 120 ps. (Fig. 3.4 (c), (d)). The long decay time of $\sim$ 1.65 ns in the pump-probe signal corresponds to the nonradiative recombination time between the electron at the surface and the hole at the traps in the glass. (Fig. 3.4 (c)). On the other hand, the long decay component of time-resolved luminescence corresponds to the radiative recombination of free excitons (Fig. 3.4 (b)).
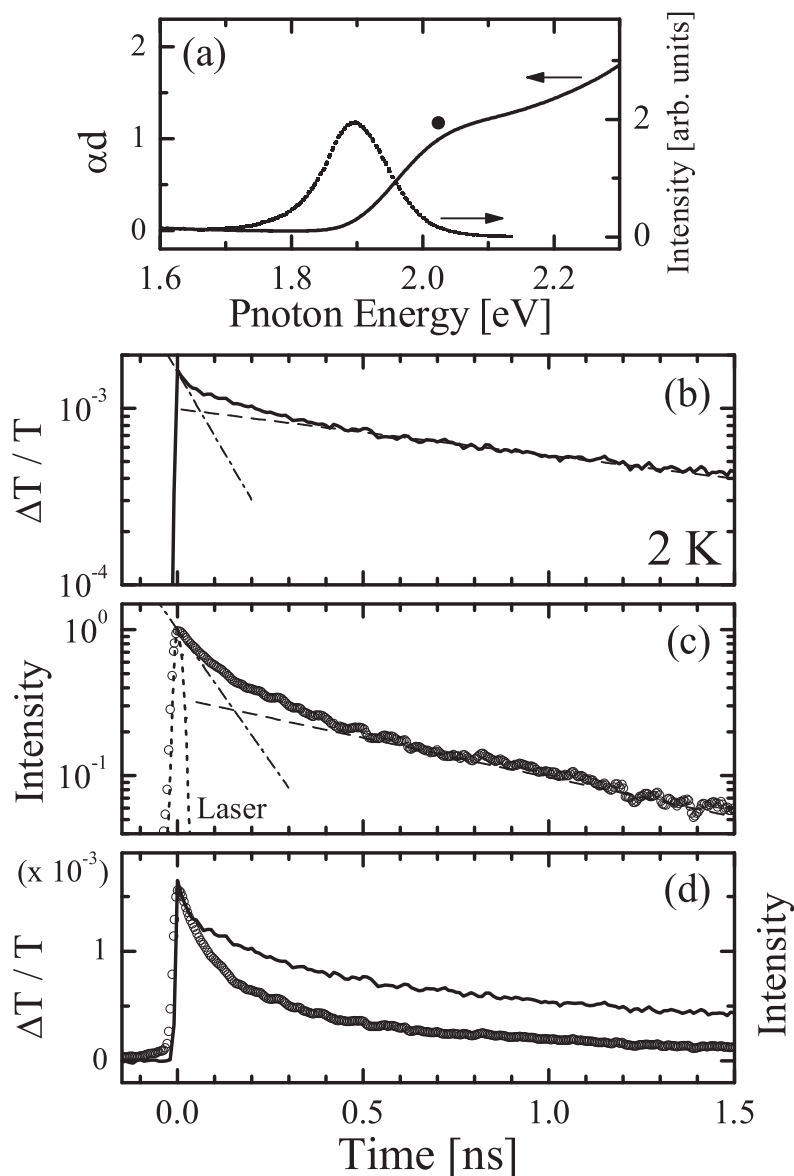
Figure 3.5: (a) Absorption (a solid line) and luminescence (a dotted line) spectra of CdSe-QDs/glass with radius of 3.6 nm. (b) Time-trace signal of differential transmission observed at 2.023 eV at 2 K. The trace is well fitted by a linear combination of two-exponential decays, $0.0005 \exp(-t/120\,\text{ps}) + 0.001 \exp(-t/1.65\,\text{ns})$. (c) Time-resolved luminescence with an excitation photon energy of 2.023 eV (open circles). The excitation light was centered at 2.295 eV at 2 K. The dotted line indicates the excitation laser pulse. The normalized signal is also fitted by double-exponential decay, $0.60 \exp(-t/120\,\text{ps}) + 0.40 \exp(-t/800\,\text{ps})$. In (b) and (c) the fast and slow decay components are shown by the dash-dotted line and dashed line, respectively. (d) Comparison between time-resolved luminescence (open circles) and differential transmission (a solid line).

3.5 Accumulated Photon Echo

In this section, we show the results of heterodyne-detected accumulated photon echo experiment in CdSe-QDs/glass. Homogeneous linewidth Γ_h is obtained from the inverse value of dephasing time T_2. Detailed measurement of temperature-dependent homogeneous linewidth reveals the intrinsic dephasing mechanism of excitons confined in CdSe-QDs/glass.

3.5.1 Experimental Setup

Figure 3.6 shows the experimental setup of the heterodyne-detected accumulated photon echo. For optical measurement at 2 K, samples were directly immersed in superfluid helium, while a temperature variable optical cryostat was used between 4 and 40 K. For a very low-temperature measurement (T < 1.5 K) one-shot ^{3}He cryostat [18] was used. An optical parametric generator pumped by 200 kHz regeneratively amplified output of a femtosecond Ti:sapphire laser was used for the excitation. The spectral linewidth of the excitation light was approximately 8 nm near the central wavelength of 600 nm, and gave the accumulated photon echo measurement a time resolution of 70 fs [19]. The accumulated photon echo experiments were done using a phase-modulation technique with a piezoelectric actuator (PZT) [20]. The echo signals were detected by balanced photo-diodes and then fed into a lock-in amplifier.

3.5.2 Results and Discussion

Time-Trace Accumulated Photon Echo Signals   Figure 3.7 shows the accumulated photon echo signal of 2.7 nm-radius CdSe-QDs/glass observed at 2 K under different excitation energy density ranging from 40 nJ/cm^2 to 1.8 μJ/cm^2. The obtained time-trace signals show initial fast decay component together with slower decay component. The decay profile of the echo signals shows no power dependence in this range, indicating that carrier-carrier scattering does not contribute to the measured dephasing time. The excitation density of
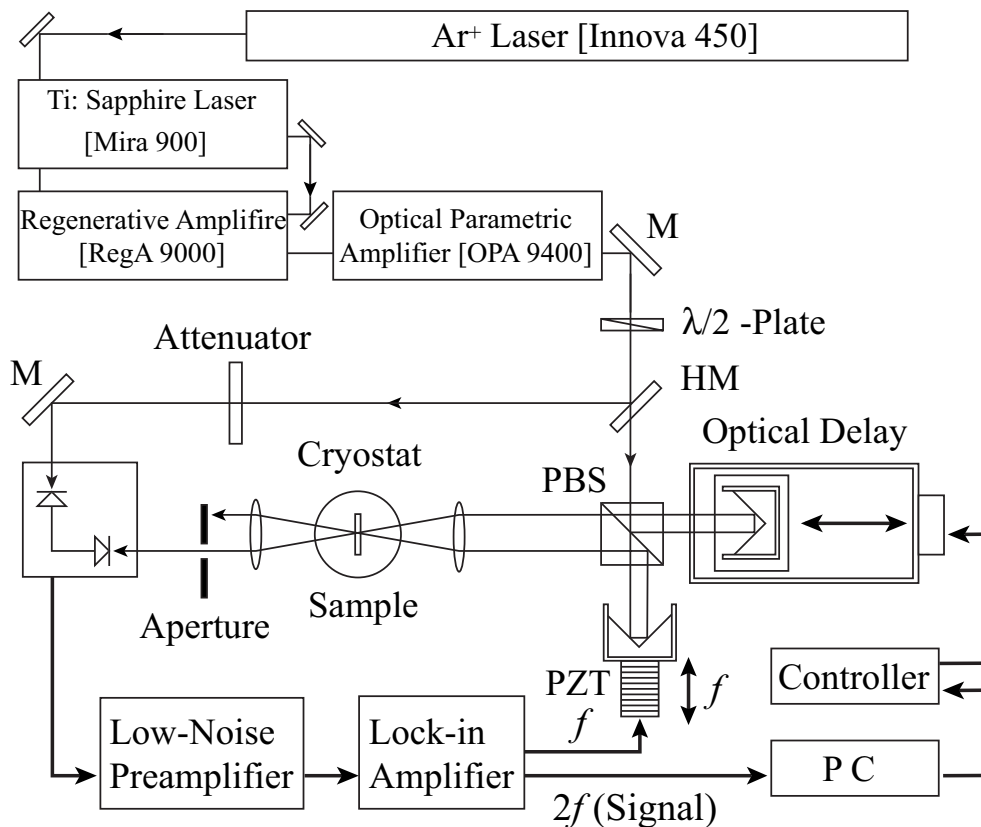
Figure 3.6: Experimental setup of the heterodyne-detected accumulated photon echo for CdSe-QDs/glass.

40 nJ/cm^2 corresponds to that of 10^{-3} photons per dot.

Figure 3.8 shows the temperature dependent time traces of the accumulated photon echo observed for 3.6-nm-radius CdSe-QDs/glass. The traces are well fitted by a linear combination of two exponential decays, $a_f \exp(-t/\tau_f) + a_s \exp(-t/\tau_s)$. The fast decay time, τ_f, was 270 fs corresponding to $\Gamma_h = 2.4$ meV in the spectral domain at 2 K. The slow decay time, τ_s, was 3.8 ps corresponding to $\Gamma_h = 0.17$ meV at 2 K. The decay time of the slow decay component becomes faster with the increase of temperature.
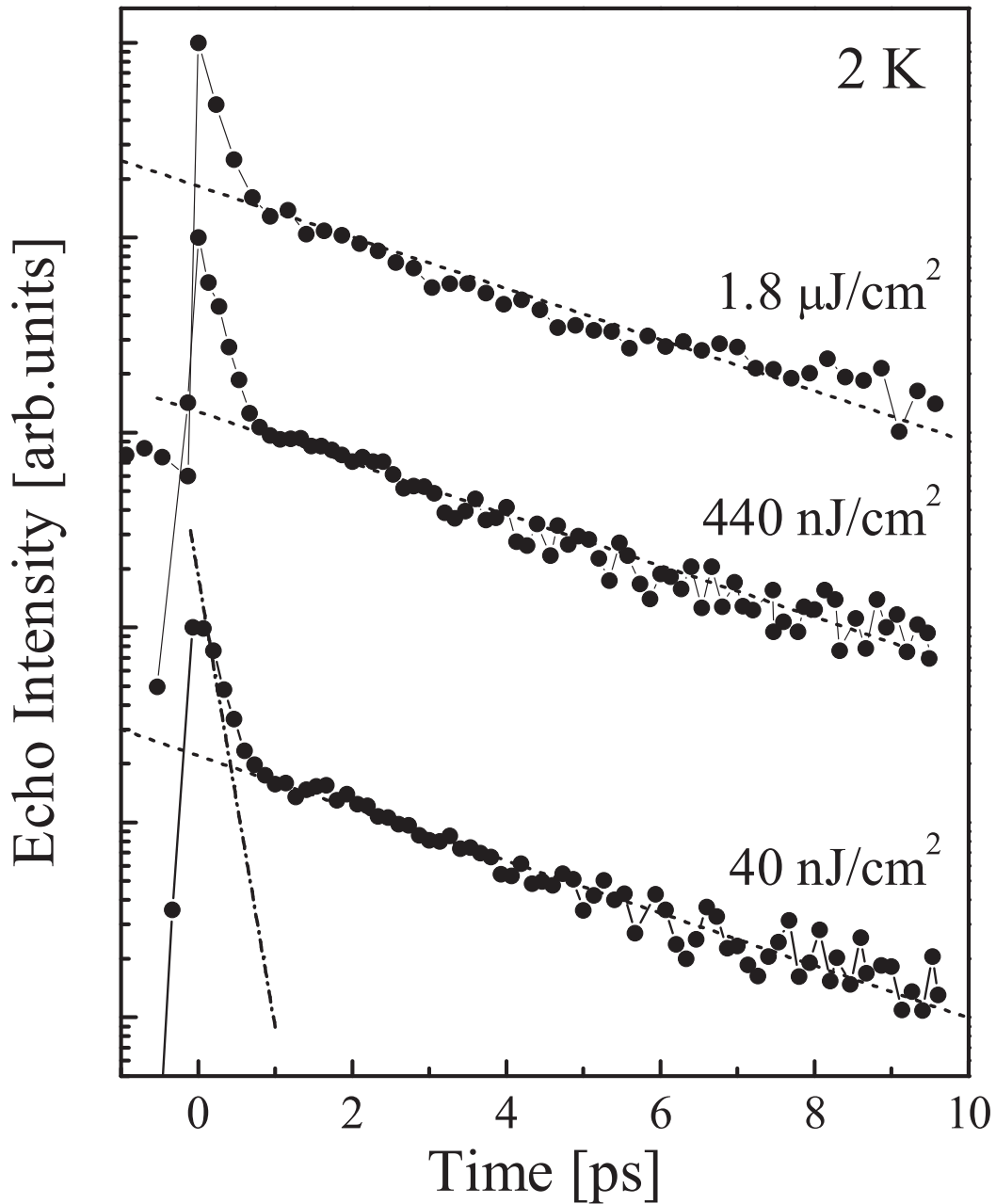
Figure 3.7: Time-trace signals of the accumulated photon echo of CdSe-QDs/glass with radius of 2.7 nm at 2 K under the excitation energy density of 40 nJ/cm², 440 nJ/cm² and 1.8μJ/cm². A dash-dotted line and dotted lines show the single-exponential fit to the fast- and slow-decay component of the echo signal, respectively.
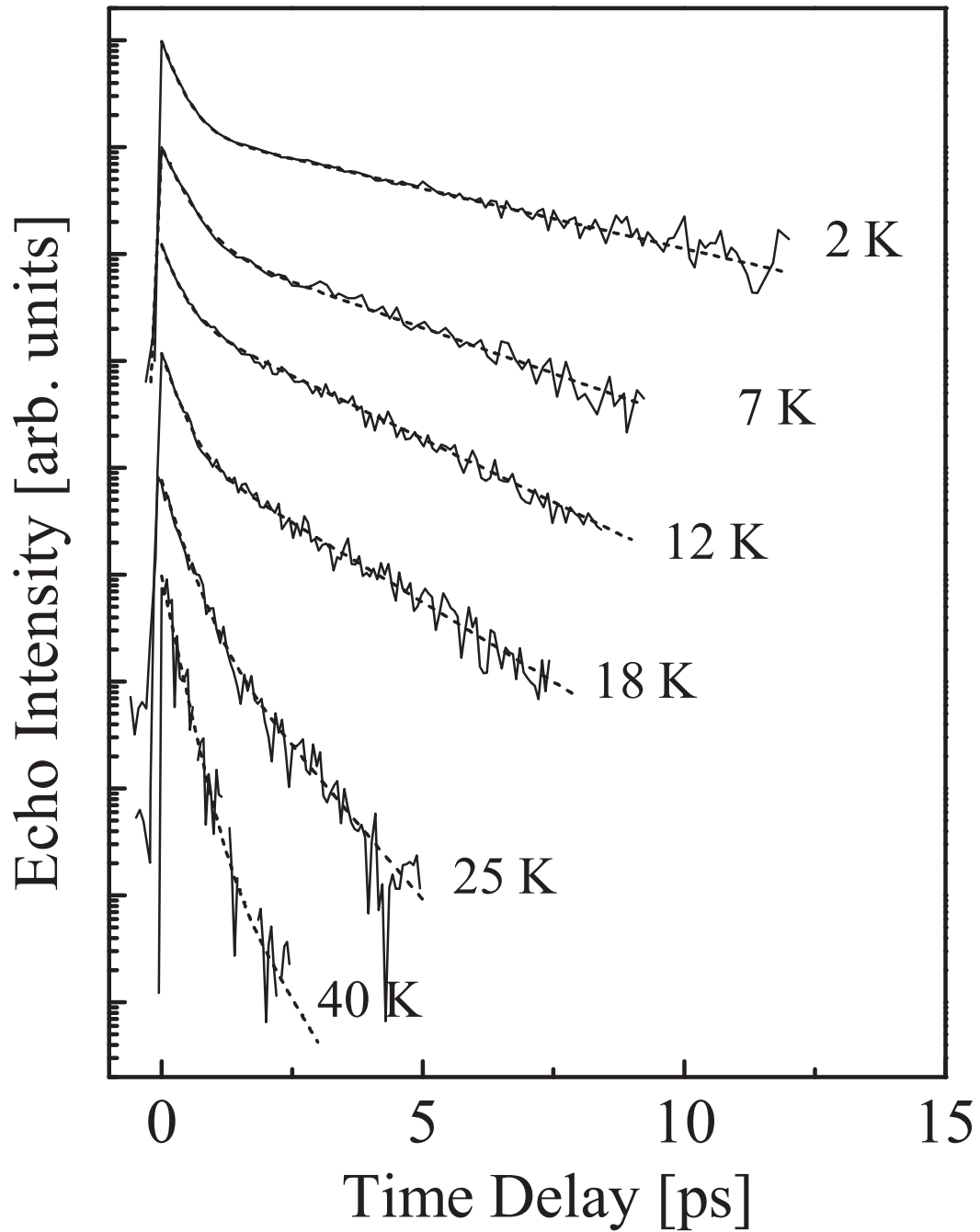
Figure 3.8: The accumulated photon echo signal for CdSe-QDs/glass (R = 3.6 nm) under excitation density of 100 nJ/cm^2 at various temperatures. Dotted lines are fitting by two-exponential decays.

Temperature Dependence of Debye-Waller Factor Now we discuss the origin of the fast and slow decay component of the double-exponential signal of the accumulated photon echo [21]. As described in Chapter 2, hole-burning spectrum can be obtained from the Fourier-cosine transform of the echo signal.

$$H(\Delta\omega) = \int_0^\infty d\tau \cos(\Delta\omega\tau) S(\tau). \tag{3.1}$$

When the echo signal has complete time-reversal symmetry, *i.e.* $S(-\tau) = S(\tau)$, eq. (3.1) becomes

$$H(\Delta\omega) = \int_{-\infty}^\infty d\tau \, e^{-i\Delta\omega\tau} S(\tau). \tag{3.2}$$

On the other hand, $H(\Delta\omega)$ is expressed by autocorrelation function of the homogeneous spectrum $J(\omega)$,

$$H(\Delta\omega) = \int_{-\infty}^\infty d\omega \, J(\omega)J(\omega + \Delta\omega). \tag{3.3}$$

Fourier-transformation of eq. (3.3) will be

$$\int_{-\infty}^\infty d(\Delta\omega) \, H(\Delta\omega) \, e^{i(\Delta\omega)\tau}$$
$$= \int d\omega \, J(\omega) \, e^{-i\omega\tau} \int d(\Delta\omega) \, J(\omega + \Delta\omega) \, e^{i(\omega+\Delta\omega)\tau}$$
$$= |J(\tau)|^2. \tag{3.4}$$

Therefore, from eq. (3.2) and (3.4), we obtain the following relation:

$$S(\tau) = \left| \int_{-\infty}^\infty d\omega \, J(\omega) \, e^{i\omega\tau} \right|^2. \tag{3.5}$$

Considering the normalized $J(\omega)$, the peak height of the echo signal $S(0)$ will be

$$S(0) = \left| \int_{-\infty}^\infty d\omega \, J(\omega) \right|^2 = 1. \tag{3.6}$$

Taking into account the temperature-dependent Debye-Waller factor $\alpha(T)$ which is related to the coupling strength of the electron-phonon interaction, the zero-phonon line $Z(\omega)$ is described as

$$Z(\omega) = \frac{\alpha(T)}{\pi} \frac{\Gamma}{\omega^2 + \Gamma^2}, \tag{3.7}$$

where Γ is the homogeneous width of the zero-phonon line. The value of $\alpha(T)$ decreases exponentially with increasing temperature. Then eq. (3.7) is intuitively understood as the decreasing of the zero-phonon-line intensity due to the coupling to lattice vibration. In this case, the echo signal coming from the zero-phonon line is described as follows:

$$S_{\mathrm{z}}(\tau) = \left| \int_{-\infty}^{\infty} d\omega \, Z(\omega) \, e^{i\omega\tau} \right|^2 = \alpha^2 \, e^{-2\Gamma\tau}. \tag{3.8}$$

Consequently, the following relation is derived:

$$\alpha = \left[\frac{S_{\mathrm{z}}(0)}{S(0)} \right]^{1/2}. \tag{3.9}$$

Here $S(0)$ is the peak height around the time origin and $S_{\mathrm{z}}(0)$ is the extrapolated value of the exponential decay which is related to the zero-phonon linewidth. In our case, the observed echo signal showed double-exponential decay as in Fig. 3.8. Assuming the slow decay component, $a_{\mathrm{s}}\exp(-t/\tau_{\mathrm{s}})$, corresponds to the zero-phonon linewidth, eq. (3.9) is expressed as

$$\alpha = \left[\frac{a_{\mathrm{s}}}{a_{\mathrm{f}} + a_{\mathrm{s}}} \right]^{1/2}. \tag{3.10}$$

We show in Fig. 3.10 the obtained value of α using eq. (3.10) for 3.6-nm-radius CdSe-QDs/glass. The temperature dependence of the slow component contribution, $[a_{\mathrm{s}}/(a_{\mathrm{f}}+a_{\mathrm{s}})]$ is plotted in Fig. 3.10. The calculated Debye-Waller factor decreases with increasing temperature.

By the theory based on linear electron-phonon interaction considering a single-phonon mode, the Debye-Waller factor can be expressed by [22]

$$\alpha = \exp\left[-\xi^2 \coth\left(\frac{\hbar\omega}{2k_{\mathrm{B}}T} \right) \right]. \tag{3.11}$$

The plotted data in Fig. 3.10 can be well fitted by eq. (3.11). The fitting parameter of $\hbar\omega = 2.0$ meV is almost comparable to the confined acoustic phonon energy observed from the Raman scattering experiment, indicating that the fast component is ascribed to the phonon sideband (Fig. 3.9). On the other hand, the slow component in the echo decay,
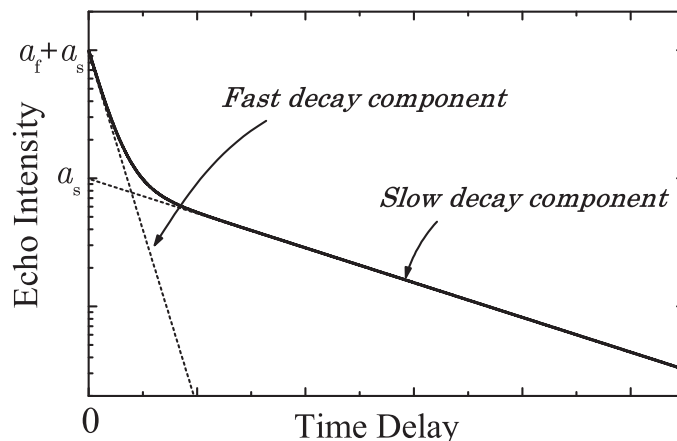
Figure 3.9: Schematic figure of the double-exponential decay of the echo signal.

that is sharp spectrum, is ascribed to the zero-phonon line. Similar spectral features of the homogeneous spectrum consisting of very sharp zero-phonon line superposed on acoustic phonon sideband were observed in CuCl quantum dots by means of PSHB [23].

Fourier-Transformed Echo Signal   Twice of the decay time constant in the heterodyne-detected accumulated photon echo signal corresponds to T_2. The fast decay component of $T_1 = 120$ ps observed in the pump-probe and luminescence time traces discussed in the last section is much longer than T_2 measured by the accumulated photon echo, indicating that the localization of electrons and/or holes at the surface of the quantum dots contributes little to T_2. The relation between accumulated photon echo signals and their Fourier-transformed spectra are shown in Fig. 3.11 and 3.12. The Fourier-cosine transformation of the accumulated photon echo signal exhibits its homogeneous spectrum of a 0.17 meV sharp line superposed on a 2.4 meV broad band. The fast decay component becomes dominant with the temperature rise. From here on, the temperature dependence of the zero-phonon linewidth obtained from the slower decay component is discussed.
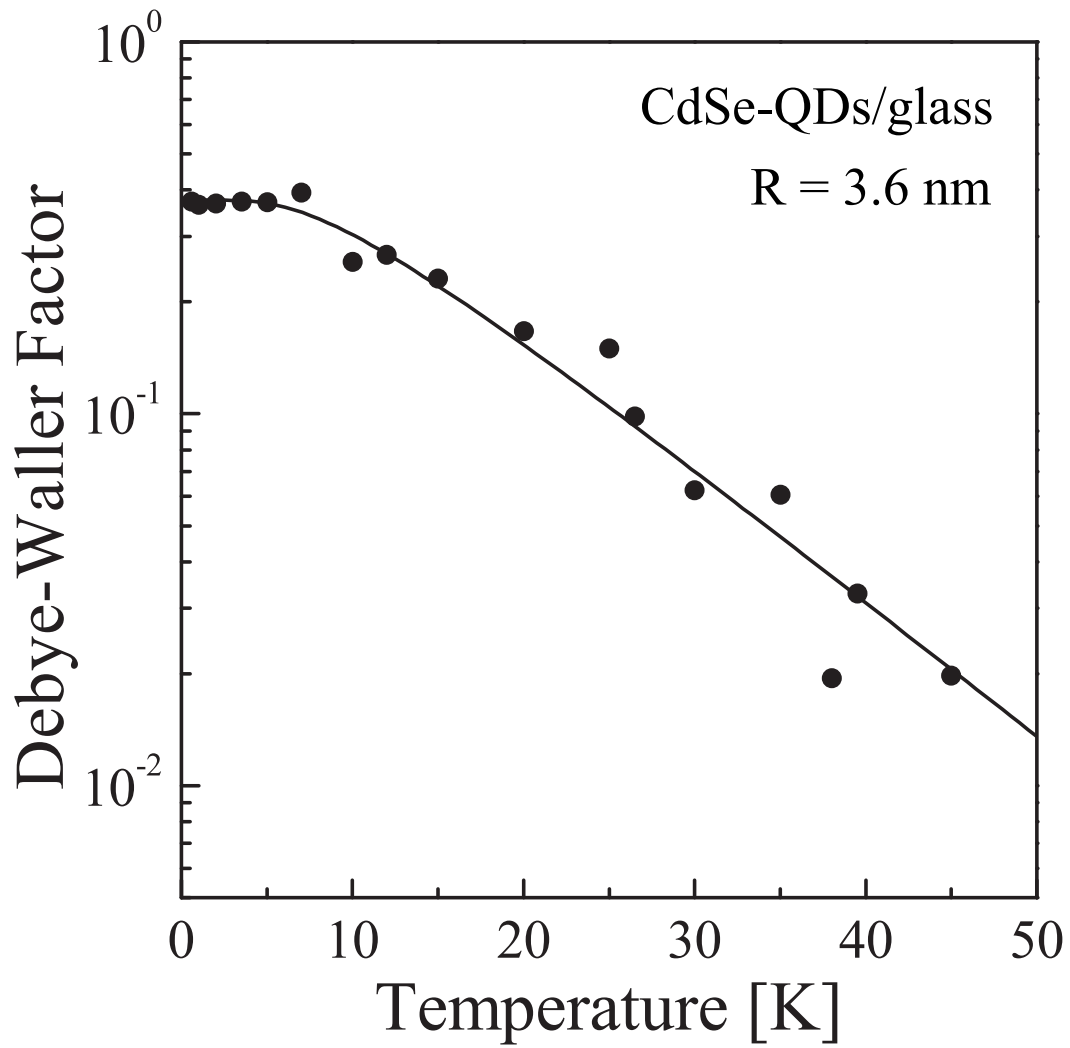
Figure 3.10: Temperature dependence of the Debye-Waller factor for 3.6-nm-radius CdSe-QDs/glass estimated from the HAPE signals using eq. (3.10) (closed circles). The solid line shows the fitting by eq. (3.11) for the fitting parameters of $S_0 = 0.96$, $\hbar\omega = 2.0$ meV.
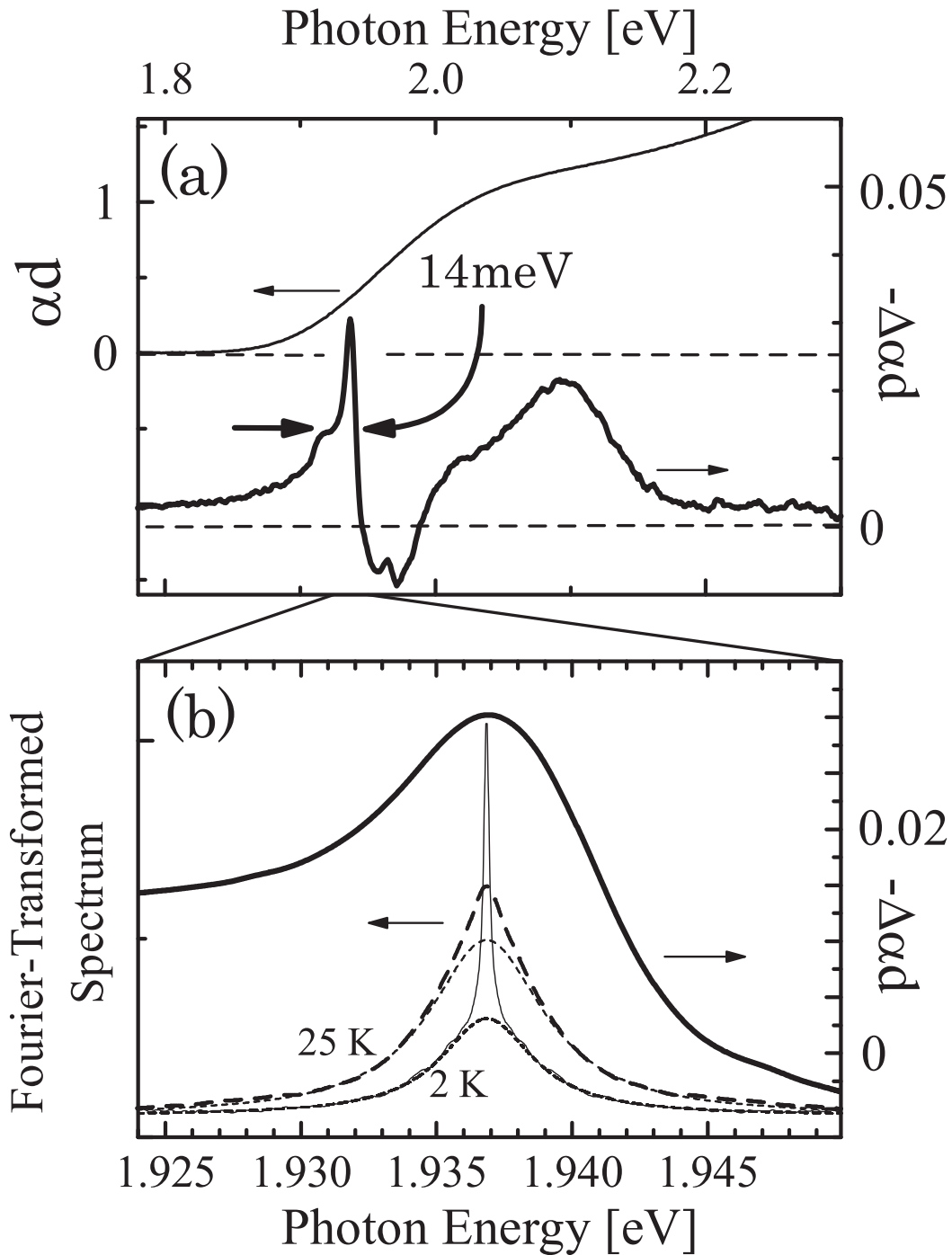
Figure 3.11: (a) The absorption spectrum (thin solid line) and the persistent hole-burning spectrum (thick solid line) of CdSe-QDs/glass with radius of 3.6 nm. The CdSe sample is excited by 9000 shots of dye laser pulses with the photon energy of 1.937 eV, and energy density of 0.18 mJ/cm^2. (b) Fourier-transformed spectrum of the accumulated photon echo in Fig. 3.8 at 2 K and 25 K. Their broad components are described by dotted lines. The persistent hole-burning spectrum in (a) is replotted by a thick solid line.
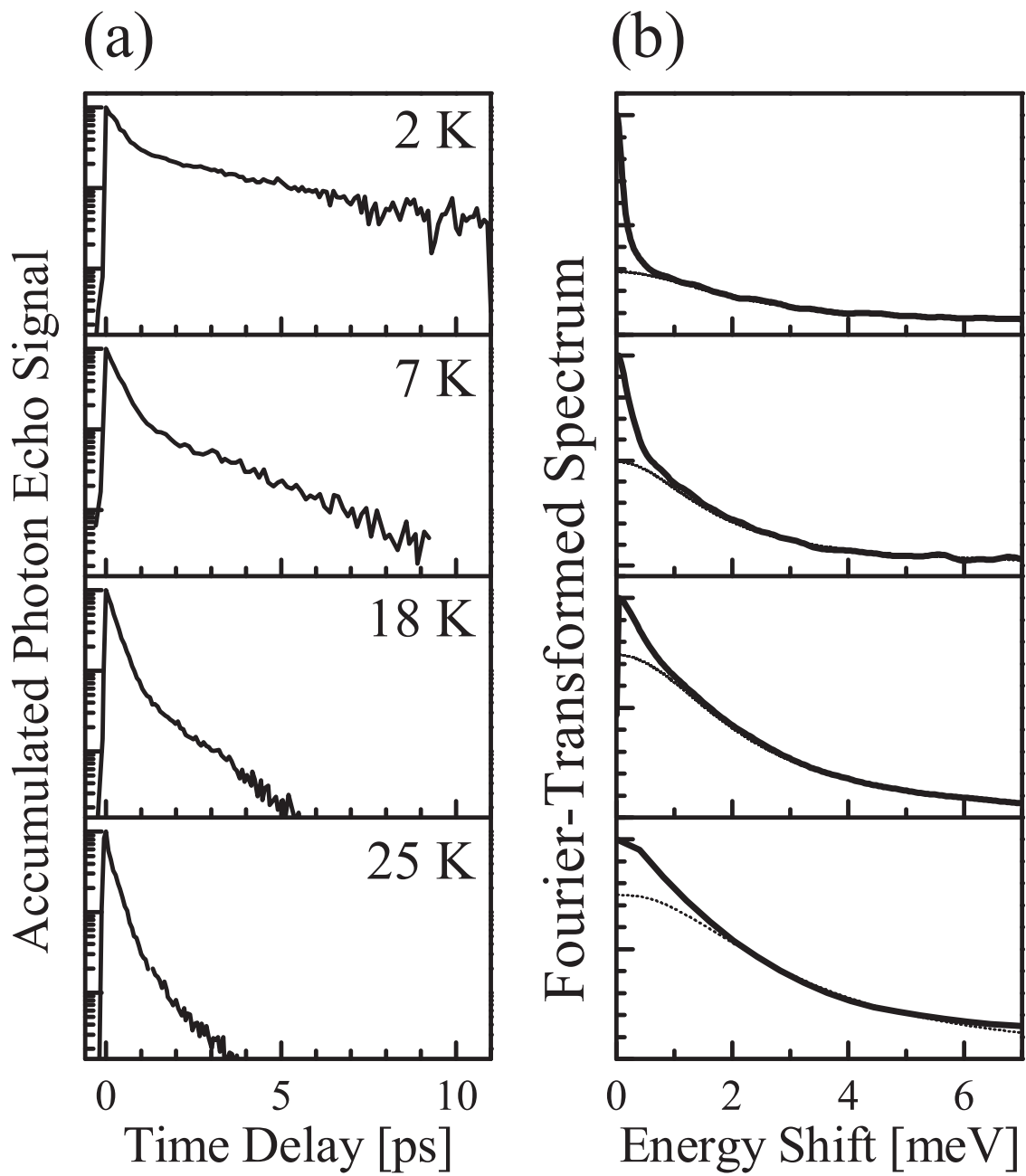
Figure 3.12: (a) Time-trace signals of the accumulated photon echo of CdSe-QDs/glass (R = 3.6 nm) at different temperatures. (b) Corresponding Fourier-transformed spectra of (a).

Temperature Dependent Homogeneous Broadening Fig. 3.13 shows temperature-dependent homogeneous broadening of CdSe-QDs/glass with radius of 3.6 nm. Homogeneous widths show almost linear dependence on temperature between 0.7 and 10 K. However, they deviate from the T-linear dependence above 10 K.

Considering the existence of confined phonon sideband in the Fourier-transformed accumulated photon echo spectrum, and in Raman scattering experiment which is discussed later, the quadratic temperature dependence of the homogeneous linewidth above 10 K considered to arise from the quantized acoustic phonon modes in quantum dots. Discrete phonon modes taking into account the lowest order electron-phonon interaction bring about a two-phonon Raman process where simultaneous absorption and emission of phonons occurs [8, 18]. Its scattering probability is proportional to $n(n + 1)$, where n is the phonon occupation number, $n(T) = 1/[\exp(\hbar\omega'/k_{\mathrm{B}}T) - 1]$. In this case, homogeneous broadening coming from exciton-phonon interaction can be expressed as

$$\gamma_{\mathrm{ph}}(T) \propto \int_0^\infty d\omega' \, F_{\mathrm{ph}}(\omega') \sinh^{-2}\left(\frac{\hbar\omega'}{2k_{\mathrm{B}}T}\right), \tag{3.12}$$

where $F_{\mathrm{ph}}(\omega')$ is distribution function of phonon frequency ω'. When we consider a pseudolocalized phonon, or confined phonon in quantum dots, F_{ph} is replaced by delta-function centered at single-mode phonon frequency ω. Therefore, eq. (3.12) will be

$$\gamma_{\mathrm{ph}}(T) \propto \sinh^{-2}\left(\frac{\hbar\omega}{2k_{\mathrm{B}}T}\right). \tag{3.13}$$

Equation 3.13 fits the observed quadratic temperature dependence of the homogeneous linewidth above 10 K very well, however, it cannot explain the T-linear broadening at very low temperature. One possible dephasing process is coupling to a two-level system (TLS). Two-level system was proposed in 1972 by Phillips and Anderson for the first time [24, 25], which had been used to explain the anomalous temperature dependence of the homogeneous linewidth of impurity atoms in a glass matrix or dye molecules in a polymer [26]. The basic concept of TLS is as follows. Carrier trapping at the surface of quantum dots produces more than one ground states of the total system consisting of quantum dots and host
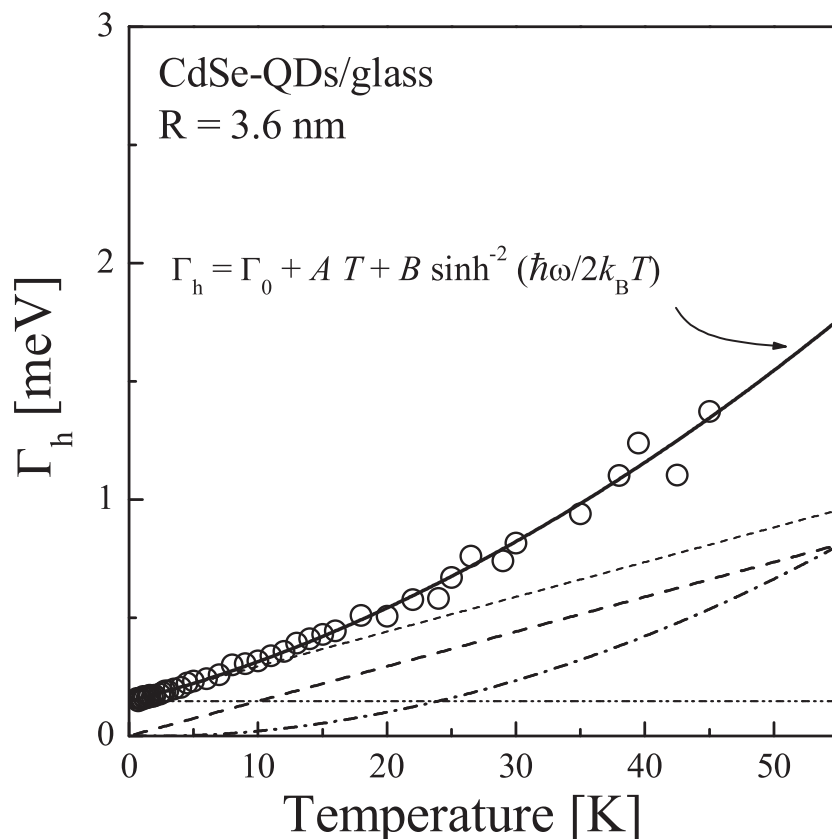
Figure 3.13: Temperature dependence of the homogeneous linewidths (in linear scale) for 3.6 nm CdSe-QDs/glass. Open circles show the experimental data. Thick solid line shows fitting to the data by eq. (3.18). The dashed line and dash-dotted line indicate the contribution of two-level system and two-phonon Raman scattering process of confined acoustic phonons, respectively. The fitting parameters are as follows: $\Gamma_{h0} = 0.147$ meV and $\hbar\omega = 1.56$ meV.

materials [27] as shown in Fig. 3.15. Many ground-state configurations can be simplified into the double welled potential representation (Fig. 3.16). If we consider the spectral diffusion, the dephasing of the exciton states is caused by interaction with acoustic phonons of the host materials. The effect of the flipping is to modulate the exciton states in such a manner that the homogeneous linewidth evolves with time diffusively.

The effect of the TLS on the homogeneous broadening can be considered as *two-tunnelon* process supposing the quantization of TLS. The probability of this process is proportional to
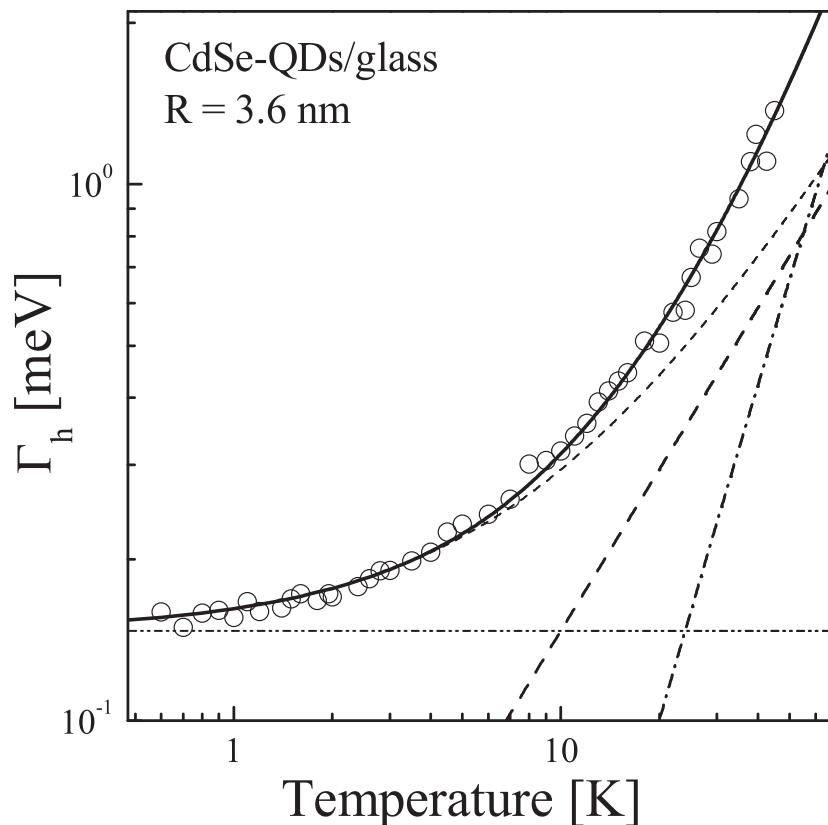
Figure 3.14: Temperature dependence of the homogeneous linewidths (in logarithmic scale) for 3.6 nm CdSe-QDs/glass. For the lines, see Fig. 3.13.

$f(f+1)$, where f is the Fermi factor, $f(T) = 1/[\exp(\delta'/k_\mathrm{B}T)+1]$. Therefore, homogeneous broadening coming from exciton-TLS interaction can be expressed as

$$\gamma_\mathrm{TLS}(T) \propto \int_0^\infty d\delta' \, F_\mathrm{TLS}(\delta') \cosh^{-2}\left(\frac{\delta'}{2k_\mathrm{B}T}\right), \qquad (3.14)$$

where $F_\mathrm{TLS}(\delta')$ is the distribution function of the TLS energy. If the TLS energy concentrates on a characteristic energy, δ, F_TLS is replaced by delta-function centered at the energy of δ. Therefore, eq. (3.14) will be

$$\gamma_\mathrm{TLS}(T) \propto \cosh^{-2}\left(\frac{\delta}{2k_\mathrm{B}T}\right). \qquad (3.15)$$

On the other hand, if the TLS energy are widely distributed throughout the glassy matrix,
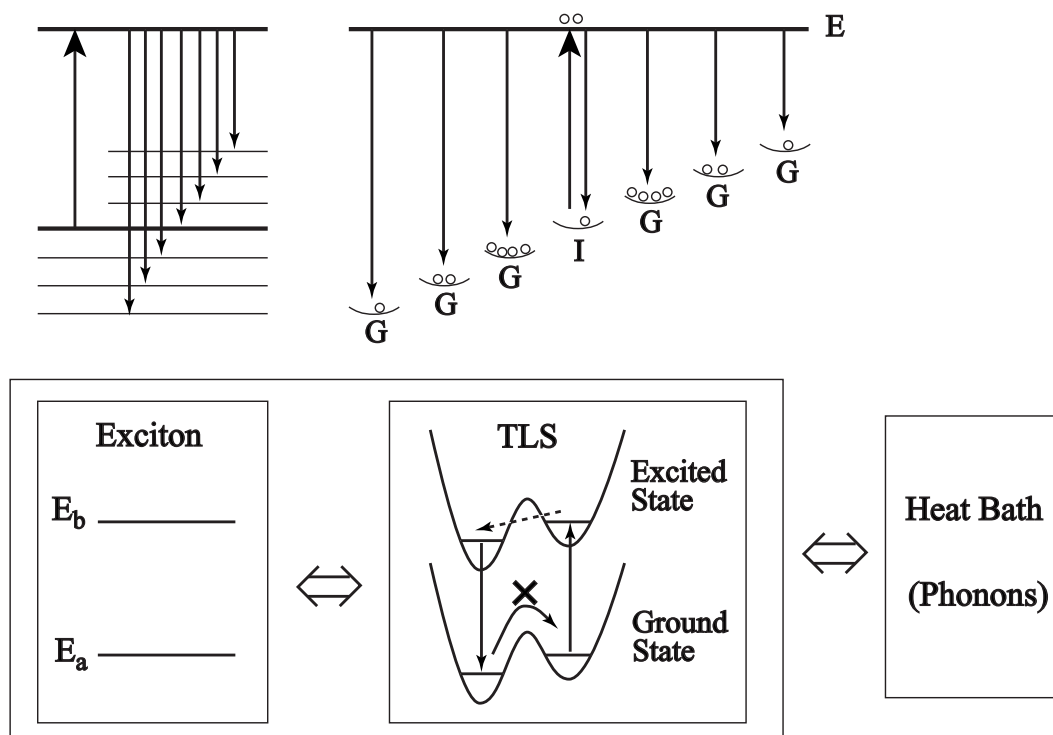
Figure 3.15: Upper figures: Schematic drawing of the many-ground-state configuration. Lower figures: Sketch of the TLS model coupled to the exciton states and the phonon field.

the average of eq. (3.15) becomes

$$
\begin{aligned}
\langle \gamma_{\mathrm{TLS}}(T) \rangle &\propto F_{\mathrm{TLS}}(0) \int_0^{\varepsilon_{\mathrm{m}}} d\delta' \cosh^{-2}\left(\frac{\delta'}{2k_{\mathrm{B}}T}\right) \\
&= 2k_{\mathrm{B}}T \, F_{\mathrm{TLS}}(0) \tanh\left(\frac{\varepsilon_{\mathrm{m}}}{2k_{\mathrm{B}}T}\right).
\end{aligned} \tag{3.16}
$$

Supposing that the upper limit of the TLS-energy distribution, ε_{m} is larger than T, eq. (3.16) is approximated as

$$
\gamma_{\mathrm{TLS}} \propto T. \tag{3.17}
$$

Using eq. (3.12) and (3.17), we obtain the expression of homogeneous line broadening as a function of temperature taking into account the contribution of exciton-confined-phonon interaction and exciton-TLS interaction:

$$
\Gamma_{\mathrm{h}}(T) = \Gamma_{\mathrm{h0}} + A\,T + B \sinh^{-2}\left(\frac{\hbar\omega}{2k_{\mathrm{B}}T}\right), \tag{3.18}
$$
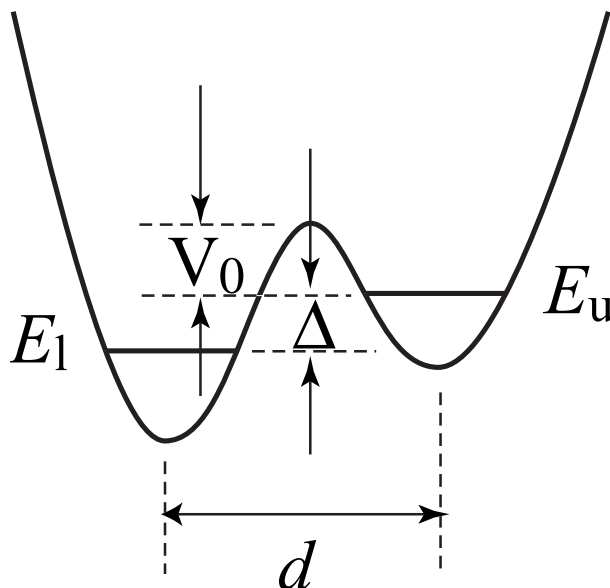
Figure 3.16: The energy diagram of TLS with an upper state (E_u) and lower state (E_l) in a configuration coordinate. V_0, Δ and d indicate potential barrier height, energy asymmetry of the well depth, and distance between two potential minima, respectively.

where Γ_h0 is temperature-independent term, $\hbar\omega$ is the energy of the confined phonon frequency, A and B are fitting parameters. Equation (3.18) gives best fitting to the data for the parameters of $\Gamma_\mathrm{h0} = 0.147$ meV, $\hbar\omega = 1.56$ meV, $A = 0.0147\,\mathrm{meV \cdot K^{-1}}$, and $B = 0.022$ meV as shown in Fig. 3.13 and 3.14.

Size Dependence The HAPE signals for representative two samples are shown in Fig. 3.17. Temperature dependence of the homogeneous linewidth for four different size of CdSe quantum dots are shown in Fig. 3.18. The temperature where the hyperbolic-sine-term becomes effective increases with decrease of dot size (arrows in Fig. 3.18). The confined phonon energies were experimentally observed by Raman scattering (discussed in the next chapter), which agree well with our fitting values, $\hbar\omega$. According to the hole-burning measurement for interband [4] and intraband [28] excitation, the coupling to the LO phonon is little below 50 K. The transition energy between $1S_{3/2}1S_\mathrm{e}$ and $2S_{3/2}1S_\mathrm{e}$ ($\geq$ 60 meV) [29] is larger than the bulk LO phonon energy ($\approx$ 26 meV). Only the exciton-level
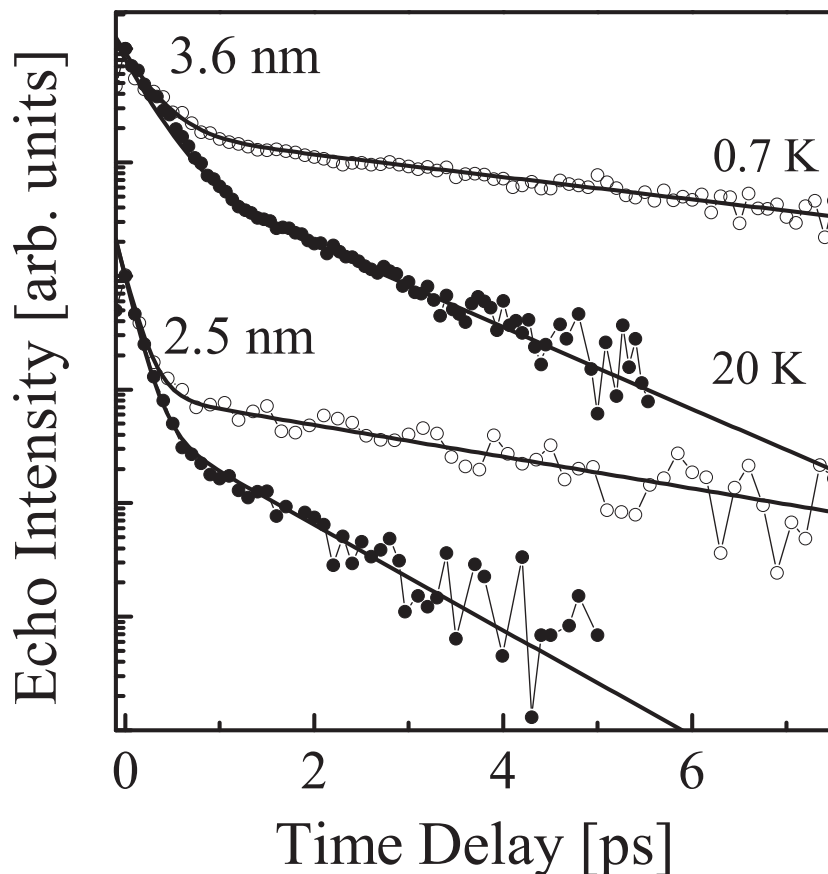
Figure 3.17: The accumulated photon echo signals at 0.7 K (open circles) and 20 K (closed circles). Upper (Lower) two curves correspond to CdSe-QDs/glass with radius of 3.6 nm (2.5 nm).

splitting between optically active and inactive states is in several meV range [30]. Thus it is naturally understood that the remarkable broadening above 10 K comes from the two-phonon Raman process of the confined acoustic phonon, as in polymer system [8].

We plot in Fig. 3.19 the size dependence of Γ_{h0} which is the homogeneous width extrapolated to 0 K corresponding to the first term in eq. (3.18). The value of Γ_{h0} were 0.22, 0.20, 0.17 and 0.15 meV for CdSe-QDs/glass with radii of 2.3, 2.5, 2.7 and 3.6 nm, respectively. They are almost proportional to $1/R$, suggesting the scattering from impurity or crystalline defect sites [6]. This contribution does not lead to a change in the transient bleach signal, and the scattering rate depends on $1/R$ because the effective density of surface scattering

should vary roughly as the surface-to-volume ratio. This mechanism is discussed again in Chapter 4.

Here, it should be noted that Γ_{h0} was broader than the inverse of nonradiative lifetime, 120 ps, measured by luminescence decay and pump-and-probe decay as the fast-decay component as discussed in Section 3.4. This assure the quality of samples whose dephasing time of the exciton at the lowest temperature is not limited by T_1 but only by the surface scattering process. In this case, we can say that the observed temperature-broadening process up to 40 K comes from the pure dephasing process.
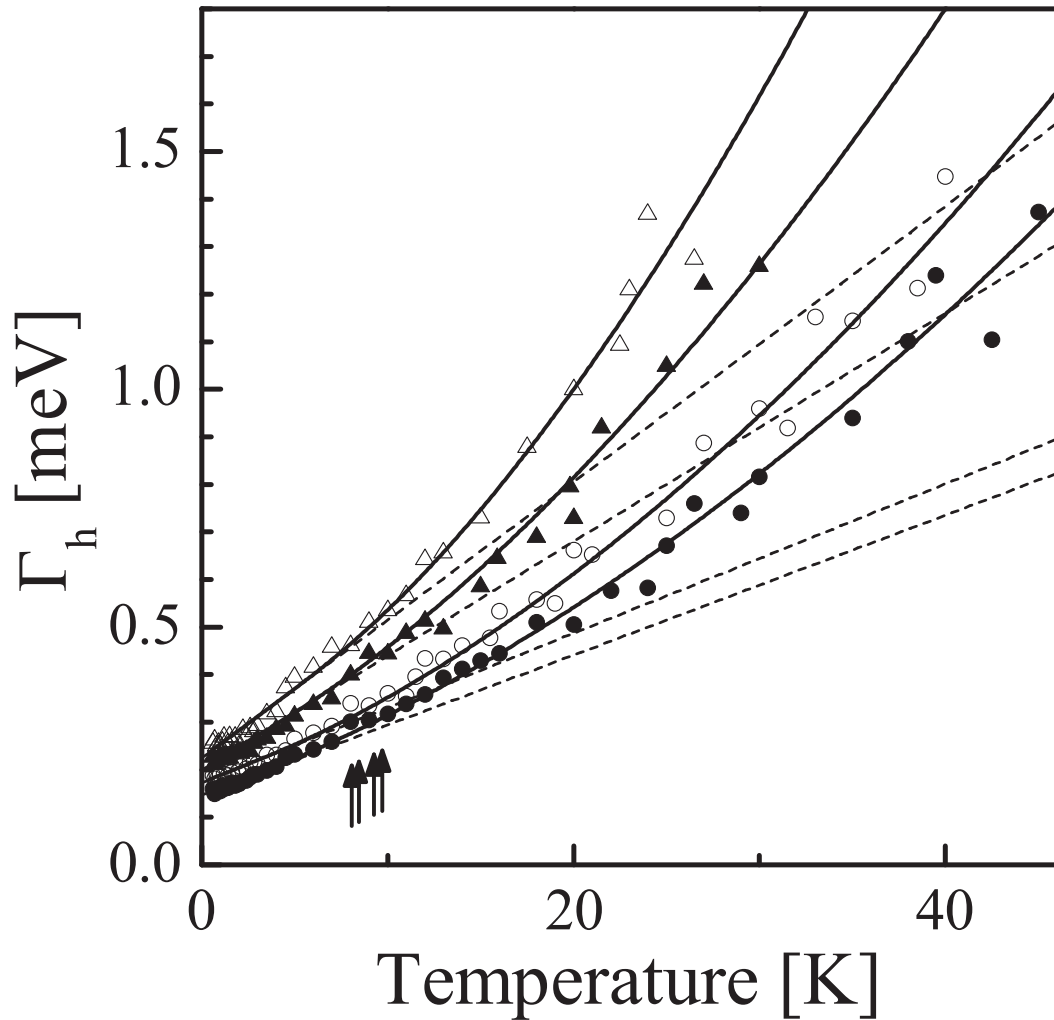
Figure 3.18: Temperature dependence of the zero-phonon linewidth for CdSe-QDs/glass with radii of 2.3 nm (open triangles), 2.5 nm (closed triangles), 2.7 nm (open circles) and 3.6 nm (closed circles). Solid lines show the fitting results based on eq. (3.18). The confined-phonon energies as a fitting parameter are $\hbar\omega =$3.4, 2.9, 2.1 and 1.6 meV, respectively. The extrapolated value of the homogeneous width, Γ_{h0}, at 0 K are 0.22, 0.20, 0.17 and 0.15 meV, respectively.
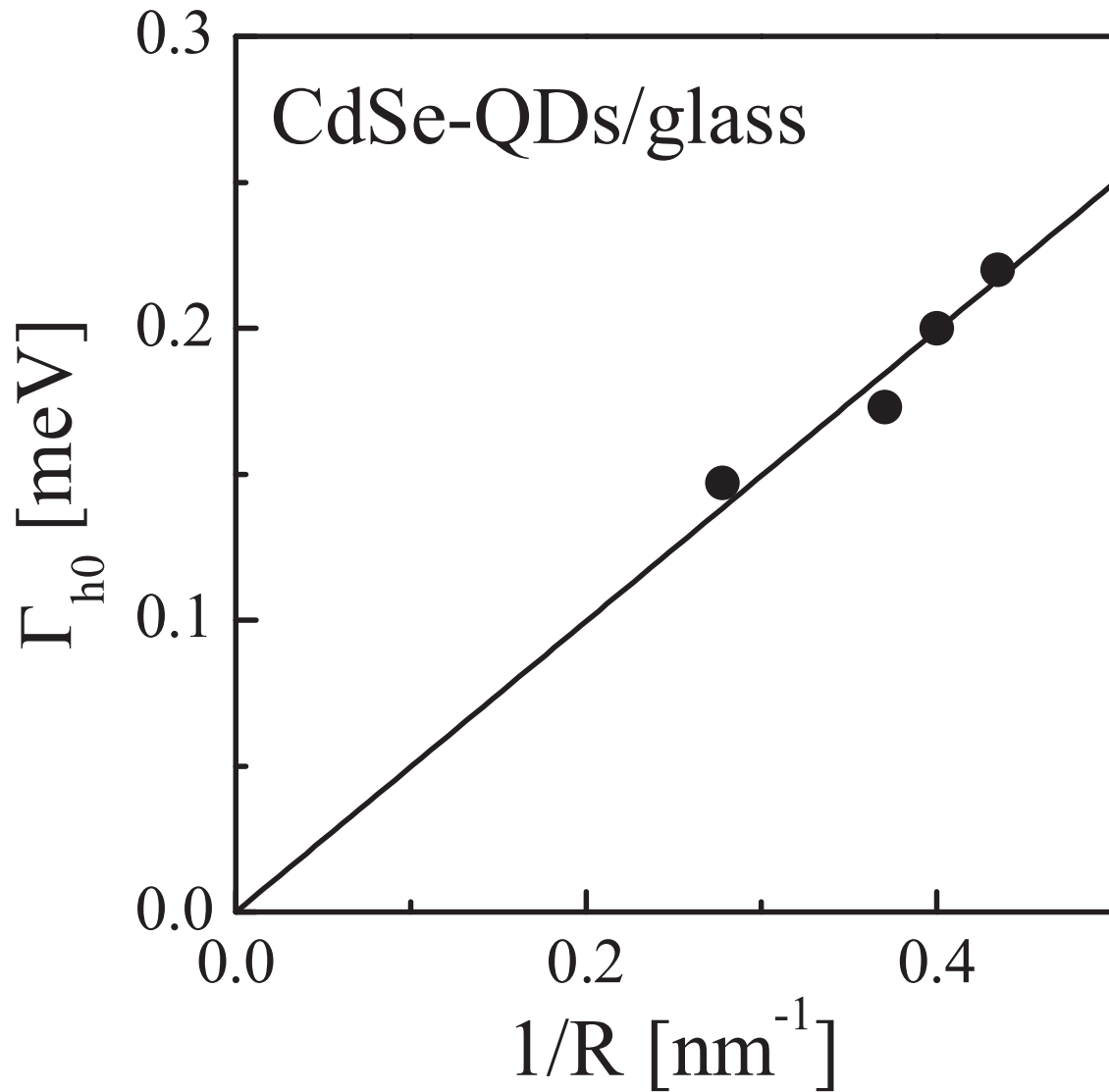
Figure 3.19: The size dependence of the homogeneous linewidth extrapolated to 0 K for CdSe-QDs/glass with average radii of 2.3, 2.5, 2.7 and 3.6 nm. The value of Γ_{h0} are 0.22, 0.20, 0.17 and 0.15 meV, respectively.

3.6 Raman Scattering Experiment

In order to determine the confined phonon energy of CdSe-QDs/glass, Raman scattering experiment was performed. As an excitation source, we used an argon ion laser whose wavelength was set at 514.5 nm. The excitation power was always kept below 5 mW and laser beam was focused onto the sample using a cylindrical lens in order to avoid sample heating. The Raman signal was collected and focused into a double-pass monochromator (Jovin Yvon U-1000 with focal length of 100 cm × 2) and detected by a photomultiplier under a single photon-counting method . The overall spectral resolution of the Raman scattering measurement was 0.1 $\mathring{A}$. All the experiment was performed at room temperature.

Figure 3.21 shows the low-frequency Raman scattering spectra of CdSe quantum dots with radii of 2.3, 2.5, 2.7 and 3.6 nm. In both Stokes and anti-Stokes sides, the phonon sidebands corresponding to low-frequency vibrational modes were observed. With decreasing dot size, both of the peak energy of the phonon sidebands and the scattering intensity increased. The Stokes energy was estimated by single Gaussian fitting to the data (dotted curves in Fig. 3.22). Normalization of the Raman spectra by the Bose factor made no difference in the estimation of the phonon energy.

The free vibrational modes of an isotropic sphere are investigated theoretically by Lamb [31]. Two kinds of modes are Raman active in the non-resonant case [32]. They are "spherical" mode with angular momentum $l = 0$ and "ellipsoidal" mode with angular momentum $l = 2$ (Fig. 3.20). Each mode is determined by branch numbers n ($n = 1, 2, 3 \cdots$). The phonon energies with the low-frequency mode linearly depend on inverse of the dot size as shown in the inset of Fig. 3.22, whose coefficients agree well with the calculation for the lowest $l = 0$ spheroidal mode [33]. Therefore, we conclude that these low-frequency modes come from the confined acoustic phonon modes. This feature is consistent with the previously reported Raman experiment [33]. The obtained confined phonon energy, $\hbar\omega = 1.7$ meV (R = 3.6 nm), 2.3 meV (R = 2.7 nm), 2.8 meV (R = 2.5 nm) and 3.5 meV (R = 2.3 nm) agreed very well with the fitting parameter of eq. (3.18): 1.6 meV

Figure 3.20: Displacement of spherical quantum dots reflecting low-frequency vibrational eigenmodes: (a) breathing mode ($l = 0, n = 1$), (b) ellipsoidal mode ($l = 2, n = 1$), and (c) torsional mode ($l = 2, n = 1$).

(R = 3.6 nm), 2.1 meV (R = 2.7 nm), 2.9 meV (R = 2.5 nm), and 3.4 meV (R = 2.3 nm). This suppose the model that the deviation from T-linear dependence of the homogeneous linewidth observed by the accumulated photon echo comes from excitonic dephasing due to two-phonon Raman process of confined acoustic phonon. Here, the broadening of the Raman spectra, e.g., 4.7 meV for 2.5 nm quantum dots, is almost equal to the half-width at half-maximum of the broader component of the Fourier-transformed HAPE spectrum. This also supports our model that the fast decay component of the HAPE signal gives the phonon sideband.
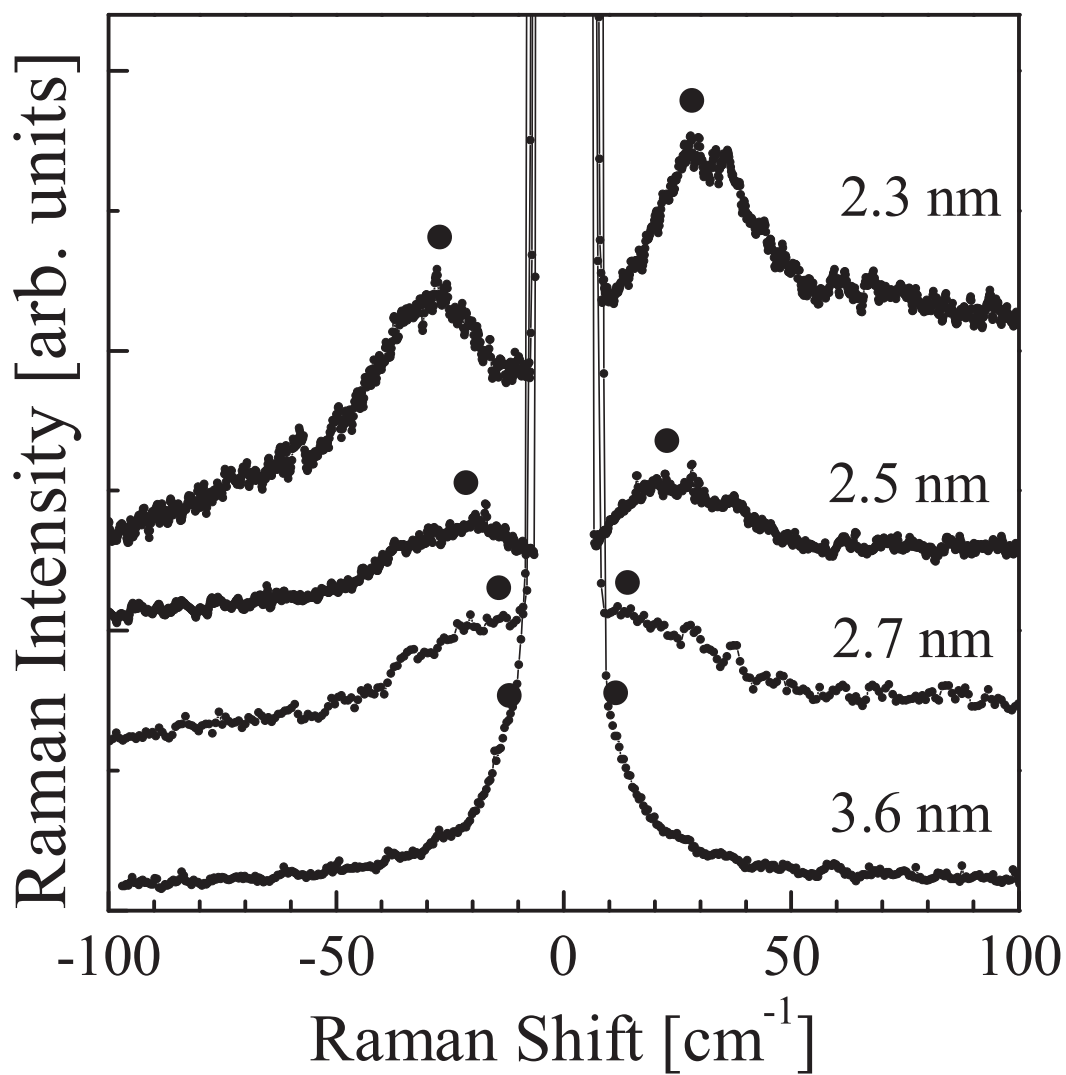
Figure 3.21: Size dependence of the low-frequency Raman scattering spectra measured for CdSe-QDs/glass with the size of 2.3, 2.5, 2.7 and 3.6 nm radii. The Raman spectra are shifted vertically for clarify.
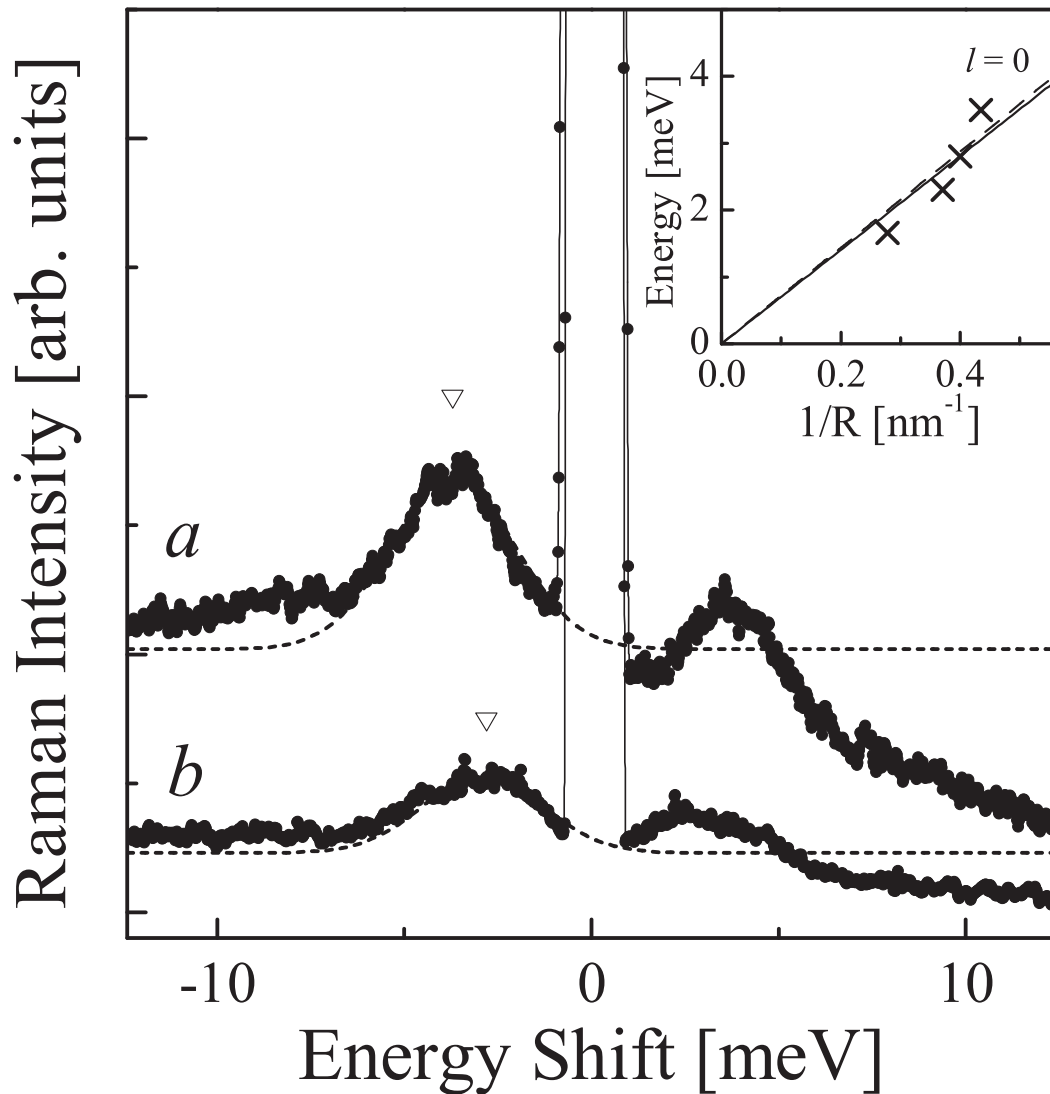
Figure 3.22: Raman scattering spectra of CdSe-QDs/glass with radii of (a) 2.3 nm and (b) 2.5 nm. The dotted lines indicate single Gaussian fittings to the Stokes-sided confined-phonon sidebands. Inset: The size dependence of the low-frequency modes obtained from Raman scattering spectra. The solid line in the inset denotes linear least-squares fit. Calculation for the lowest $l = 0$ spheroidal mode is shown by the dashed line.

3.7   Summary

Heterodyne-detected accumulated photon echo experiment was carried out at temperatures ranging from 0.6 to 40 K for CdSe-QDs/glass with radii of 2.3, 2.5, 2.7 and 3.6 nm. The time-trace signals of the photon echo were well fitted by the sum of the fast exponential decay in the femtosecond time domain and the slow exponential decay in the picosecond time domain. The slow decay component is assigned to the zero-phonon line whose decay rate became shorter with increasing temperature, while the fast decay component corresponds to the confined-phonon sideband. Below 10 K, the observed homogeneous linewidth depended linearly on temperature, while quadratic temperature dependence was observed above 10 K. The former comes from the exciton-TLS interaction and the latter comes from the exciton-confined-phonon interaction. The sharp homogeneous linewidth extrapolated to 0 K (Γ_{h0}) depends linearly on the inverse size of quantum dots, indicating the dominant contribution of surface scattering at very low temperature.

References

[1] N. Peyghambarian, B. Fluegel, D. Hulin, A. Migus, M. Jofre, A. Antonetti, S. W. Koch, and M. Lindberg, IEEE J. Quantum Electron. **QD-25**, 2516 (1989).

[2] A. P. Alivisatos, A. L. Harris, N. J. Levinos, M. L. Steigerwald, and L. E. Brus, J. Chem. Phys. **89**, 4001 (1988).

[3] M. G. Bawendi, W. L. Wilson, L. Rothberg, P. J. Carol, T. M. Jedju, M. L. Steigerwald, and L. E. Brus, Phys. Rev. Lett. **65**, 1623 (1990).

[4] U. Woggon, S. Gaponenko, W. Langbein, A. Uhrig, and C. Klingshirn, Phys. Rev. B **47**, 3684 (1993).

[5] R. W. Schoenlein, D. M. Mittleman, J. J. Shiang, A. P. Alivisatos, and C. V. Shank, Phys. Rev. Lett. **70**, 1014 (1993).

[6] D. M. Mittleman, R. W. Schoenlein, J. J. Shiang, V. L. Colvin, A. P. Alivisatos, and C. V. Shank, Phys. Rev. B **49**, 14435 (1994).

[7] S. A. Empedocles, D. J. Norris, and M. G. Bawendi, Phys. Rev. Lett. **77**, 3873 (1996).

[8] P. Palinginis and H. Wang, Appl. Phys. Lett. **78**, 1541 (2001).

[9] *Numerical Data and Functional Relationships in Science and Technology*, Landolt-Börnstein, Vol. 17: Semiconductors (Springer, Berlin, 1982).

[10] Al. Efros, Phys. Rev. B **46**, 7448 (1992).

[11] Al. Efros, Phys. Rev. B **54**, 4843 (1996).

[12] A. Kobayashi, O. F. Sankey, S. M. Volz, and J. D. Dow, Phys. Rev. B **28**, 935 (1983).

[13] G. Peter, E. Göbel, W. W. Ruhle, J. Nagle, and K. Ploog, Superlatt. Microstruct. **5**, 197 (1989).

[14] J. Feldmann, J. Nunnenkamp, G. Peter, E. Göbel, J. Kuhl, K. Ploog, P. Dawson, and C. T. Foxon, Phys. Rev. B **42**, 5809 (1990).

[15] S. Yano, T. Goto, S. Iwai, K. Edamatsu, and T. Itoh, Jpn. J. Appl. Phys. **34**, Suppl. 34-1, 140 (1995).

[16] M. G. Bawendi, P. J. Carroll, William L. Wilson, and L. E. Brus, J. Chem. Phys. **96**, 946 (1992).

[17] T. Okuno, H. Miyajima, A. Satake, and Y. Masumoto, Phys. Rev. B **54**, 16952 (1996).

[18] M. Ikezawa and Y. Masumoto, Phys. Rev. B **61**, 12662 (2000).

[19] S. Asaka, H. Nakatsuka, M. Fujiwara, and M. Matsuoka, Phys. Rev. A **29**, 2286 (1984).

[20] S. Saikan, K. Uchikawa, and H. Ohsawa, Opt. Lett. **16**, 10 (1991).

[21] S. Saikan, A. Imaoka, Y. Kanematsu, K. Sakoda, K. Kominami, and M. Iwamoto, Phys. Rev. B **41**, 3185 (1990).

[22] I. S. Osad'ko, in *Spectroscopy and Excitation Dynamics of Condensed Molecular Systems*, edited by V. M. Agranovich and R. M. Hochstrasser (north-Holland, Amsterdam, 1983).

[23] Y. Masumoto, T. Kawazoe, and N. Matsuura, J. Lumin. **76&77**, 189 (1998).

[24] W. A. Phillips, J. Low Temp. Phys. **7**, 351 (1972).

[25] P. W. Anderson, B. I. Halperin, and C. M. Warma, Phil. Mag. **25**, 1 (1972).

[26] For review, see: R. M. Macfarlane and R. M. Shelby, J. Lumin. **36**, 179 (1987); D. L. Huber, in *Dynamical Processes in Disordered Systems*, edited by W. M. Yen (Trans. Tech. Aedermannsdorf, Switzerland, 1989).

[27] Y. Masumoto, T. Kawazoe, and T. Yamamoto, Phys. Rev. B **52**, 4688 (1995).

[28] M. Shim and P. Guyot-Sionnest, Phys. Rev. B **64**, 245342 (2001).

[29] D. J. Norris and M. G. Bawendi, Phys. Rev. B **53**, 16338 (1996).

[30] D. J. Norris, Al. L. Efros, M. Rosen, and M. G. Bawendi, Phys. Rev. B **53**, 16347 (1996).

[31] H. Lamb, Proc. London. Math. Soc. **13**, 189 (1882).

[32] E. Duval, Phys. Rev. B **46**, 5795 (1992).

[33] L. Saviot, B. Champagnon, E. Duval, I. A. Kudriavtsev, and A. I. Ekimov, J. Non-Cryst. Solids **197**, 238 (1996).

Chapter 4

Optical Dephasing of Excitons in CuBr Quantum Dots

4.1 Introduction

In this chapter, we discuss the excitonic dephasing mechanism of CuBr-QDs/glass and CuBr-QDs/NaBr at low temperature. Compared to CdSe quantum dots in the strong confinement regime and CuCl quantum dots in the weak confinement regime, the study of the homogeneous broadening is very little for CuBr quantum dots. Recently, the T_2 of 6.4 ps and 2.3 ps have been reported for CuBr quantum dots in borosilicate glass by using the four-wave mixing and transient hole-burning measurement, respectively [1]. T_2 of 8.4 ps was also reported for CuBr-QDs/glass using the accumulated photon echo [2]. These works have focused on the *intrinsic* dephasing mechanism but not on the *extrinsic* one. In fact, the temperature dependence of the homogeneous width in CuBr quantum dots has been explained only by the acoustic-phonon scattering in the high-temperature approximation and the LO-phonon scattering processes [1].

In the previous chapter, we have clarified that temperature-dependent line-broadening comes from the exciton-TLS interaction below 10 K and from the exciton-confined-phonon interaction above 10 K. If the interaction with the surface or the interface of quantum dots give the essential effect on the optical properties of quantum dots embedded in matrices, the dephasing process of exciton confined in very small quantum dots should be affected

by the difference of host matrices. These phenomena come from trap states which exist in surface or interface between quantum dots and host material.

In this chapter, we show the results of matrix-dependent temperature dependence of homogeneous broadening of CuBr-QDs/glass and CuBr-QDs/NaBr. We compare the obtained results with that of strong-confined CdSe quantum dots and previously reported results of weakly-confined CuCl quantum dots [3]. Extending the study to quantum dots ranging from weak to strong confinement regime reveals the universal influence of surface-related effects and two-confined-acoustic phonon scattering on the dephasing process of quantum dots in matrices.

4.2 Property of CuBr

Lattice Structure Cupper bromide (CuBr) is a I-VII compound semiconductor with different structures depending on temperature. The crystal structure at room temperature of CuBr is zincblende structure, and wurtzite structure above the transition temperature ($\approx$ 600 K). Physical parameters of CuBr are shown in Fig. 4.1.

Band Structure Extrema of the lowest conduction band and the highest valence band are located at the center of the Brillouin zone, at the Γ point and thus the exciton absorption is of the direct allowed type at the Γ point. The valence band comes from s orbitals of the 4s states of copper. The 3d states of the copper ions form the highest valence bands, Γ_8 and Γ_7. The spin-orbit coupling contributes to the valence band splitting between the two upper valence bands with splitting energy of 150 meV.

The $Z_{1,2}$ and Z_3 exciton states come from the heavy hole with quantum number $J_h = 3/2$ and $1/2$, respectively. The heavy and light hole in the Γ_8 valence bands and k-linear terms in these bands due to the inversion symmetry bring about the anisotropic multicomponents of $Z_{1,2}$ exciton states [4]. The exciton Bohr radius of CuBr, $a_B \approx 1.5$ nm, is very small compared to that of the II-VI or III-V direct gap semiconductors. This is the reason why

CuBr quantum dots belongs to weak or intermediate confinement region.

4.3 Samples

Figure 4.2 shows typical linear absorption spectra of (a) CuBr-QDs/glass and (b) CuBr-QDs/NaBr at 2 K. As the average radius of dots becomes smaller, the absorption peaks of the $Z_{1,2}$ and Z_3 excitons shift to higher energy side. The average radii of the quantum dots were determined by X-ray scattering at small angles: $R = 2.9, 3.3, 3.8, 4.8$ and 6.5 nm for CuBr-QDs/glass, $R = 2.9, 4.8$ and 6.5 nm for CuBr-QDs/NaBr.

Physical property		Numerical value
lattice structure		cubic (zincblende)
density		$4.72 \, \text{g/cm}^2$
melting point		$487 \, ^\circ C$
bandgap energy (1.6 K)	$E_g \; (\Gamma_8 v \to \Gamma_6 c)$	3.072 eV
free exciton transition energy (K)	$Z_{1,2}(1\text{S})$	2.960 eV
	$Z_3(1\text{S})$	3.119 eV
conduction band, effective mass		$0.23 \; m_0$
valence band, effective mass		$23.2 \; m_0$
exciton Bohr radius		1.25 nm
exciton binding energy		108 meV
lattice constant (hexagonal modification)		0.57 nm
phonon wavenumbers	ν_{LO}	$167 \; \text{cm}^{-1}$ (20.7 meV)
	ν_{TO}	$136 \; \text{cm}^{-1}$ (16.8 meV)

Table 4.1: Physical parameters of bulk CuBr.
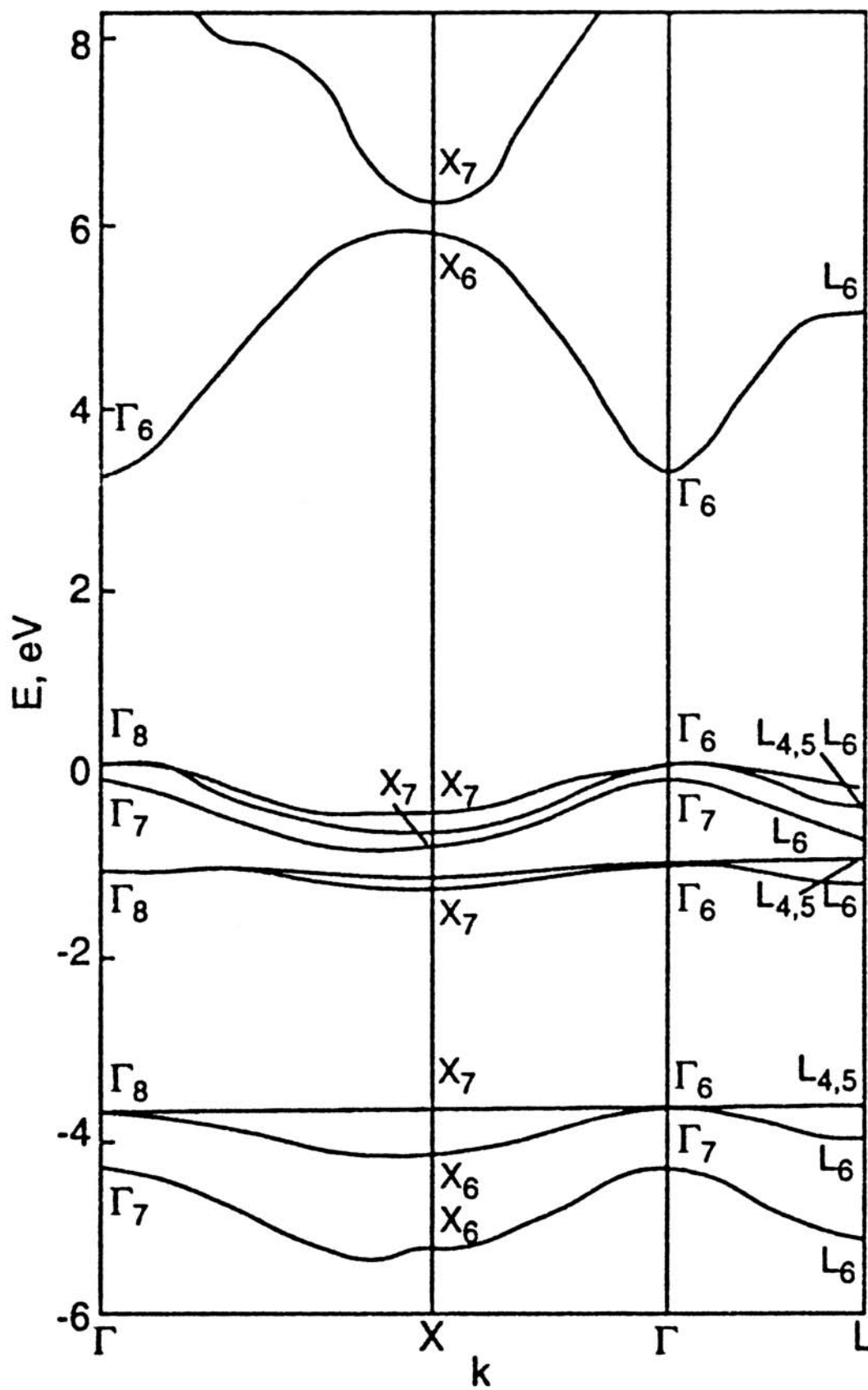
Figure 4.1: Band structure of CuBr [5].
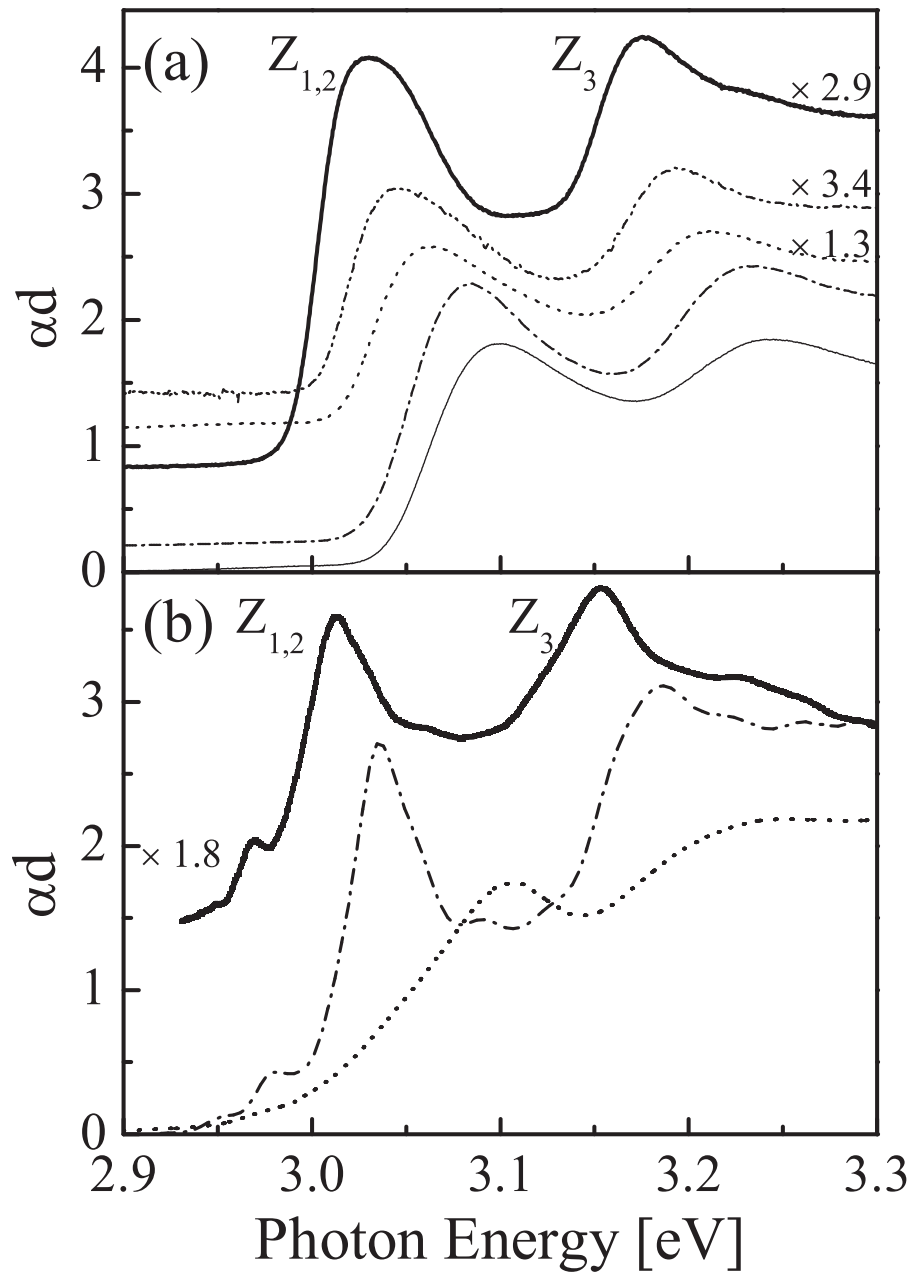
Figure 4.2: (a) Absorption spectra of CuBr-QDs/glass with radii of 2.9 nm (thin solid line), 3.3 nm (dash-dotted line), 3.8 nm (dotted line), 4.8 nm (dash-dot-dotted line) and 6.5 nm (thick solid line). (b) Absorption spectra of CuBr-QDs/NaBr with radii of 2.9 nm (dotted line), 3.8 nm (dash-dot-dotted line) and 6.5 nm (thick solid line). All spectra are observed at 2 K.

4.4 Accumulated Photon Echo

4.4.1 Experimental Setup

For CuBr-QDs/NaBr and CuBr-QDs/glass, a frequency-doubled beam of the output pulses of 130-fs temporal duration from a mode-locked Ti:sapphire laser was used to excite resonantly the $Z_{1,2}$ exciton in each sample.

The excitation density of the laser beam was always kept below 30 pJ/cm^2 during the photon echo measurements. In this excitation density region the dephasing rate did not depend on the excitation density and the mean number of excitons per quantum dot is smaller than 10^{-7}. Therefore, we can rule out the possibility of exciton-exciton scattering as a dephasing process. For PSHB measurement, the narrow-band dye laser pumped by the third harmonics of the output of a Q-switched Nd^{3+} : YAG laser (355 nm) was used as a pump source.
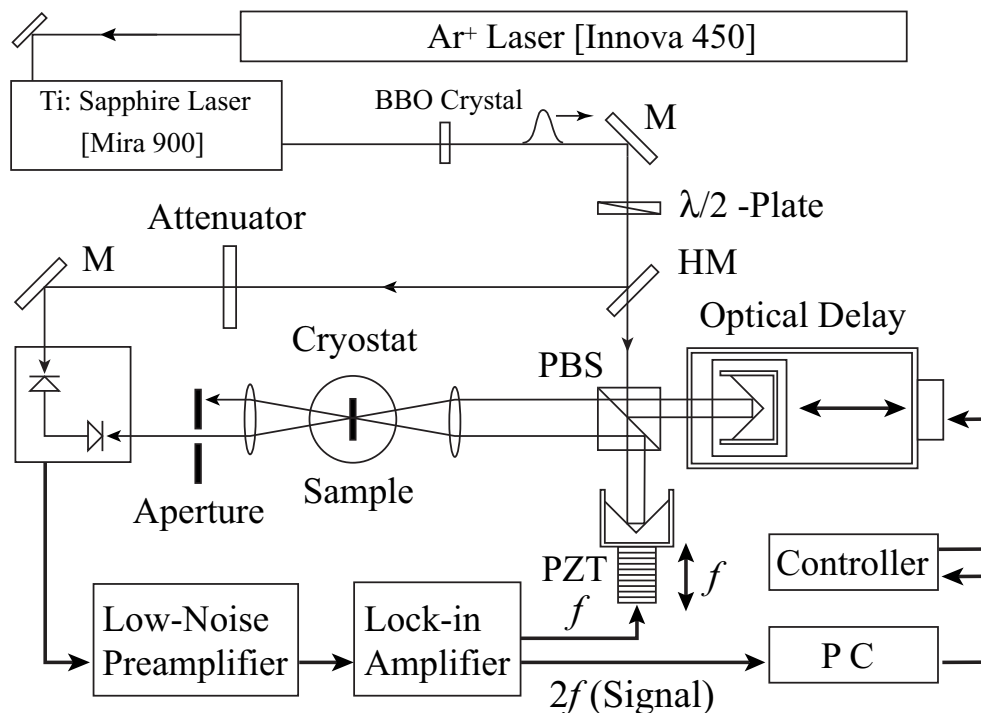
Figure 4.3: Experimental setup of the heterodyne-detected accumulated photon echo for CuBr quantum dots.

4.4.2 Results and Discussion

Time-Trace Signals Figure 4.4 shows the time-trace of the HAPE signals of 6.5 nm CuBr-QDs/glass and CuBr-QDs/NaBr at 4 K, 20 K and 40 K. The excitation intensity was always kept below 30 pJ/cm^2. The dephasing time is constant below this intensity, whereas T_2 shows linear dependence on the excitation intensity above 30 pJ/cm^2 [6].

All the echo signals exhibit single-exponential decay with single time constants corresponding to $T_2/2$. As the temperature rise, the decay time became faster. For CuBr-QDs/NaBr, the obtained dephasing times are $T_2(40\,\mathrm{K}) = 1.95\,\mathrm{ps}$, $T_2(20\,\mathrm{K}) = 5.88\,\mathrm{ps}$ and $T_2(4\,\mathrm{K}) = 38.8\,\mathrm{ps}$. On the other hand, for CuBr-QDs/glass, we obtained $T_2(40\,\mathrm{K}) = 1.68\,\mathrm{ps}$, $T_2(20\,\mathrm{K}) = 6.50\,\mathrm{ps}$ and $T_2(4\,\mathrm{K}) = 24.6\,\mathrm{ps}$. Although the dephasing time is almost the same between these two samples at 40 K and 20 K, CuBr-QDs/NaBr showed much longer T_2 than CuBr-QDs/glass at 4 K. The temperature dependence of the homogeneous linewidth for 6.5 nm CuBr-QDs/glass with the temperature range of $0.6\,\mathrm{K} \sim 80\,\mathrm{K}$ is shown in Fig. 4.5. As in the result for CdSe-QDs/glass, the obtained Γ_h showed nonlinear dependence on temperature. These data can be fitted by the following function,

$$\Gamma_\mathrm{h}(T) = \Gamma_\mathrm{h0} + A\,T + B\sinh^{-2}\left(\frac{\hbar\omega}{2k_\mathrm{B}T}\right) + \frac{C}{\exp[\hbar\Omega_\mathrm{LO}/k_\mathrm{B}T] - 1}. \tag{4.1}$$

The first term is the temperature-independent width (the offset component which determines the homogeneous width at 0 K). The second term represents the interaction with TLS. The third term is the contribution of two-phonon Raman scattering of confined acoustic phonons. The fourth term is the broadening due to the one-phonon scattering of the LO-phonon. The overall data are well reproduced by the following parameters: $\Gamma_\mathrm{h0} = 0.019\,\mathrm{meV}$, $\hbar\omega = 0.89\,\mathrm{meV}$, $A = 8\,\mu\mathrm{eV}$, $B = 4.7\,\mu\mathrm{eV}$, $C = 26\,\mathrm{meV}$. $\hbar\Omega_\mathrm{LO}$ is the LO-phonon energy of bulk CuBr ($\hbar\Omega_\mathrm{LO} = 20.97$ meV). The confined phonon energy, $\hbar\omega = 0.89$ meV, obtained from the fitting agreed well with the value of 0.86 meV obtained from the PSHB measurement (discussed later).

Next, we show in Fig. 4.6 the temperature dependence of the homogeneous broadening of CuBr-QDs/NaBr with radius of 6.5 nm. The obtained temperature dependence is obviously
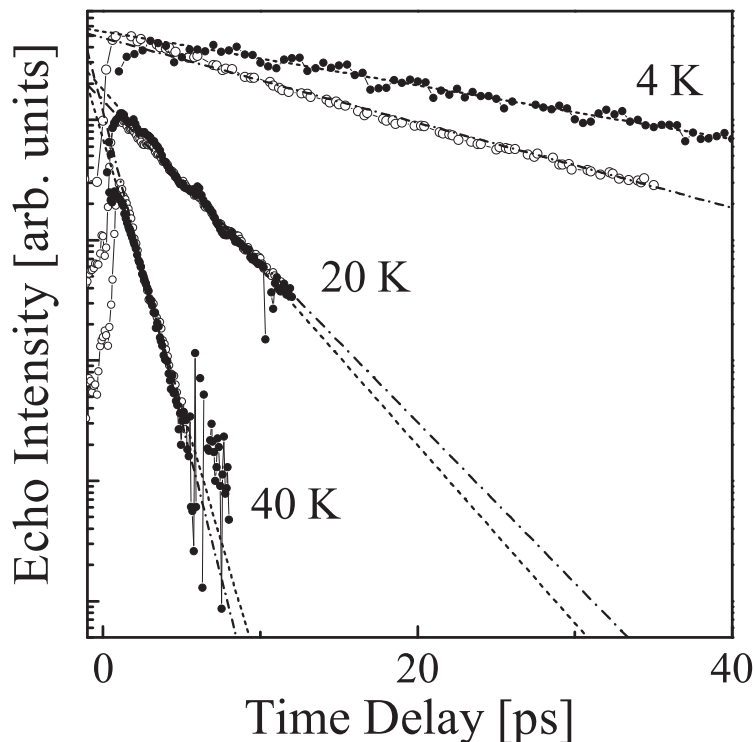
Figure 4.4: Time-trace HAPE signals between 6.5 nm CuBr-QDs/NaBr (closed circles) and CuBr-QDs/glass (open circles) at 4 K, 20 K and 40 K. The dotted lines and dash-dotted lines indicate the least-squares fits to the data for CuBr-QDs/NaBr and CuBr-QDs/glass, respectively.

different from the result of CuBr-QDs/glass. This anomalous temperature dependence of the homogeneous width cannot be fitted by eq. (4.1) but represented by the following expression:

$$\Gamma_{\mathrm{h}}(T) = \Gamma_{\mathrm{h0}} + A \cosh^{-2}\left(\frac{\delta}{2k_{\mathrm{B}}T}\right) + B \sinh^{-2}\left(\frac{\hbar\omega}{2k_{\mathrm{B}}T}\right) + \frac{C}{\exp[\hbar\Omega_{\mathrm{LO}}/k_{\mathrm{B}}T] - 1}. \qquad (4.2)$$

The first, second, third and fourth term represent the temperature-independent width, contribution of TLS with the characteristic energy δ, two-phonon Raman scattering, and LO-phonon scattering, respectively. The fitting parameters are as follows: $\Gamma_{\mathrm{h0}} = 0.029\,\mathrm{meV}$, $\delta = 2.8\,\mathrm{meV}$, $\hbar\omega = 0.95\,\mathrm{meV}$, $A = 0.27\,\mathrm{meV}$, $B = 6\,\mu\mathrm{eV}$, $C = 29\,\mathrm{meV}$.

Equations (4.5) and (4.6) are the same except the second term which originates from the matrix-dependent TLS contribution. The difference of the temperature dependence
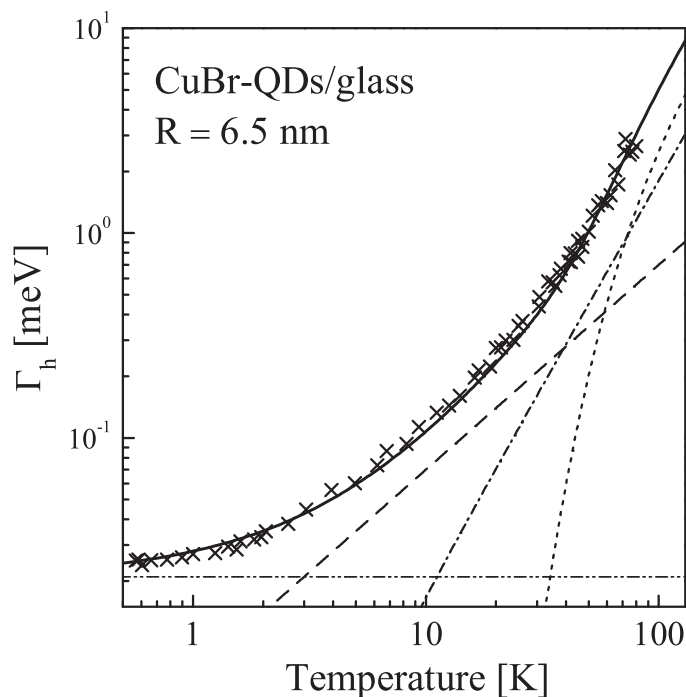
Figure 4.5: Temperature dependence of the homogeneous linewidth of CuBr-QDs/glass with radius of 6.5 nm. Crosses show the experimental data. Thick solid line represents calculated results with following components: TLS (dashed line), confined acoustic phonons (dash-dotted line), LO-phonons (dotted line), and temperature-independent width (dash-dot-dotted line).

is clearly seen in Fig. 4.7. For CuBr-QDs/glass, the homogeneous linewidth decreases monotonously from 80 K down to 0.6 K. For CuBr-QDs/NaBr, the temperature dependence are almost the same as that of the glass-matrix sample, however, the homogeneous width changes its slope at the bending point around 15 K and approaches a lower limit at 0 K. We have confirmed the same matrix dependence for 4.8 nm and 2.9 nm CuBr quantum dots (Fig. 4.8 and 4.9, respectively). These results are similar to the previous report of CuCl-QDs/glass and CuCl-QDs/NaCl [3] except the LO-phonon contribution. Moreover, the temperature-independent width Γ_{h0}, confined-phonon energy $\hbar\omega$ increased with decrease of size of quantum dots, indicating that the effect of the host material is essential for quantum dots surrounded by matrix at very low temperature. Hereafter, we discuss in detail the
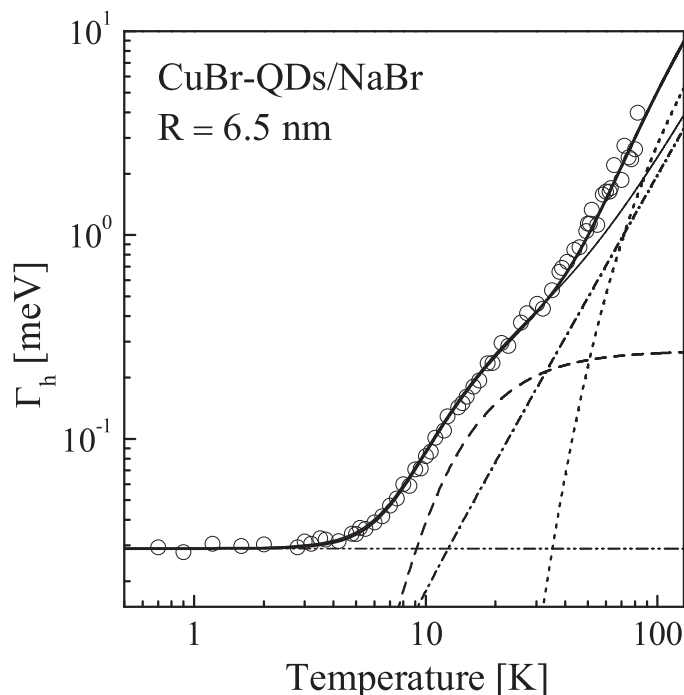
Figure 4.6: Temperature dependence of the homogeneous linewidth of CuBr-QDs/NaBr with radius of 6.5 nm. Open circles show the experimental data. The meaning of the lines is the same as Fig. 4.5.

.

origin of the temperature-dependent homogeneous broadening of confined excitons.

LO-Phonon Scattering As shown in Fig. 4.7, the homogeneous linewidth broadens rapidly above 40 K with increasing temperature. As the radii of the quantum dots become smaller, the value of the coefficient C becomes larger for both samples: $C = 26.0$ meV (6.5 nm), 32 meV (4.8 nm), 60 meV (2.8 nm) for CuBr-QDs/glass, and $C = 29.0$ meV (6.5 nm), 32 meV (4.8 nm), 60 meV (2.8 nm) for CuBr-QDs/NaBr. This indicates that the exciton-LO-phonon coupling is important above 40 K and increases with decrease of dot size. It should be noted that experimental data of the observed homogeneous width cannot be fitted well without the LO-phonon contribution as in the thin solid line in Fig. 4.7.

The fourth term of eqs. (4.1) and (4.2) are the sum of possibilities of an exciton scattered from the exciton ground state to all possible states by LO-phonons. This represents broad-

ening due to LO-phonon anti-Stokes scattering. Normally in a zero-dimensional system, no significant thermal broadening effect caused by LO-phonons would be expected [7] because discrete electron density of states prohibits the exciton-LO-phonon scattering process due to the requirement of energy conservation in scattering processes [8, 9]. However, another broadening mechanism due to the energy transition to other excitonic states is negligible in this temperature range. In fact, both the energy separation in $Z_3(1S) - Z_{1,2}(1S)$ transitions (≈ 140 meV, for 6.5 nm CuBr-QDs/NaBr) and $Z_{1,2}(1S) - Z_{1,2}(2S)$ transitions (≈ 80 meV, for bulk [4]) are larger than the LO-phonon energy. The energy splitting between the two heavy-hole-exciton states due to k-linear term (≈ 20 meV) [4] is larger than the confined acoustic phonon energy, and is comparable to $\hbar\Omega_{LO}$. These subbands can participate in the one-optical-phonon transition above 40 K.

Figures 4.7, 4.8 and 4.9 show the temperature dependence of the homogeneous linewidth of CuBr-QDs/glass and CuBr-QDs/NaBr with the radii of 6.5, 4,8 and 2.9 nm. Every data can be well reproduced by eq. (4.2), and the homogeneous width at the lowest temperature (Γ_{h0}) depended linearly on the inverse size of quantum dots, showing the dominant contribution of the surface scattering.

Confined Phonon Modes   Confined acoustic phonons were experimentally observed for CuBr quantum dots by PSHB measurement previously [10]. Figures 4.10 and 4.11 show the persistent hole-burning spectra for CuBr-QDs/glass and CuBr-QDs/NaBr with radii of 2.9, 4.8 and 6.5 nm. Stokes-side confined acoustic phonon hole was well-resolved from the main hole by Gaussian fitting (dotted lines). The obtained confined phonon energies obtained as the peak energies of the Gaussian fittings were 1.4, 1.2, 1.1, 1.1 and 0.86 meV for CuBr-QDs/glass with radii of 2.9, 3.3, 3.8, 4.8 and 6.5 nm, respectively. The energies were 1.7, 1.1 and 0.96 meV for CuBr-QDs/NaBr with radii of 2.9, 4.8 and 6.5 nm, respectively.

The size dependence of the confined phonon energy was plotted in the inset of 4.10 and 4.11. The plotted data are almost proportional to the inverse size of dots, and the values agree with the calculation for the lowest spheroidal mode with angular momentum

$l = 1, n = 1$ ($l = 0, n = 1$) on free boundary condition for CuBr-QDs/glass (CuBr-QDs/NaBr). Although only two Raman-active modes with $l = 0$ and $l = 2$ are observed [11] for quantum dots with an ideal free surface, in real quantum dots embedded in matrix, deviations from a perfect spherical surface can relax the selection rules and $l = 1$ mode can be observed in the Raman spectra [12]. Anyway, confined phonon energies obtained from the PSHB were in good agreement with the fitting value of eq. (4.1) and (4.2), suggesting that the quadratic temperature-dependence of homogeneous width between 15 K and 40 K comes from the two-phonon Raman process of confined acoustic phonons.

Two-Level System   Let us discuss the dephasing mechanism of the exciton in CuBr-QDs/NaBr and CuBr-QDs/glass below 15 K. As discussed in Chapter 3, carrier trapping at the surface of dots produces more than one ground states of the total system consisting of quantum dots and host materials as shown in Fig. 3.15 [13]. Many ground-state configurations can be simplified into the double welled potential representation. This is equivalent to the TLS model [14]. The predicted photon-echo signal on this model is of the single exponential decay form [15], in agreement with the experimental data in Fig. 4.4. When the energy of TLS is represented by the characteristic energy δ shown in Fig. 3.16, the homogeneous broadening is in proportion to $\cosh^{-2}(\delta/2k_{\mathrm{B}}T)$, while T-linear dependence is derived for widely distributed TLS energy [3]. This brings about the matrix-dependent profile of the homogeneous broadening below 15 K between CuBr-QDs/NaBr and CuBr-QDs/glass. In our case, $\delta = 2.8$ meV is obtained for CuBr-QDs/NaBr as a fitting parameter.

The temperature dependence of the homogeneous broadening for 4.8 nm and 2.9 nm-radius CuBr quantum dots are shown in Figs. 4.8 and 4.9. The coefficients, A, in eqs. (4.1) and (4.2) corresponding to the average coupling strength between an exciton and the TLS, seemed to depend linearly on the inverse size of quantum dots for both CuBr-QDs/NaBr and CuBr-QDs/glass. This is explained by the fact that the trapping rate varies as the surface-to-volume ratio, R^{-1}, because the carrier trapping process is driven by wave function overlap at the surface of quantum dots.
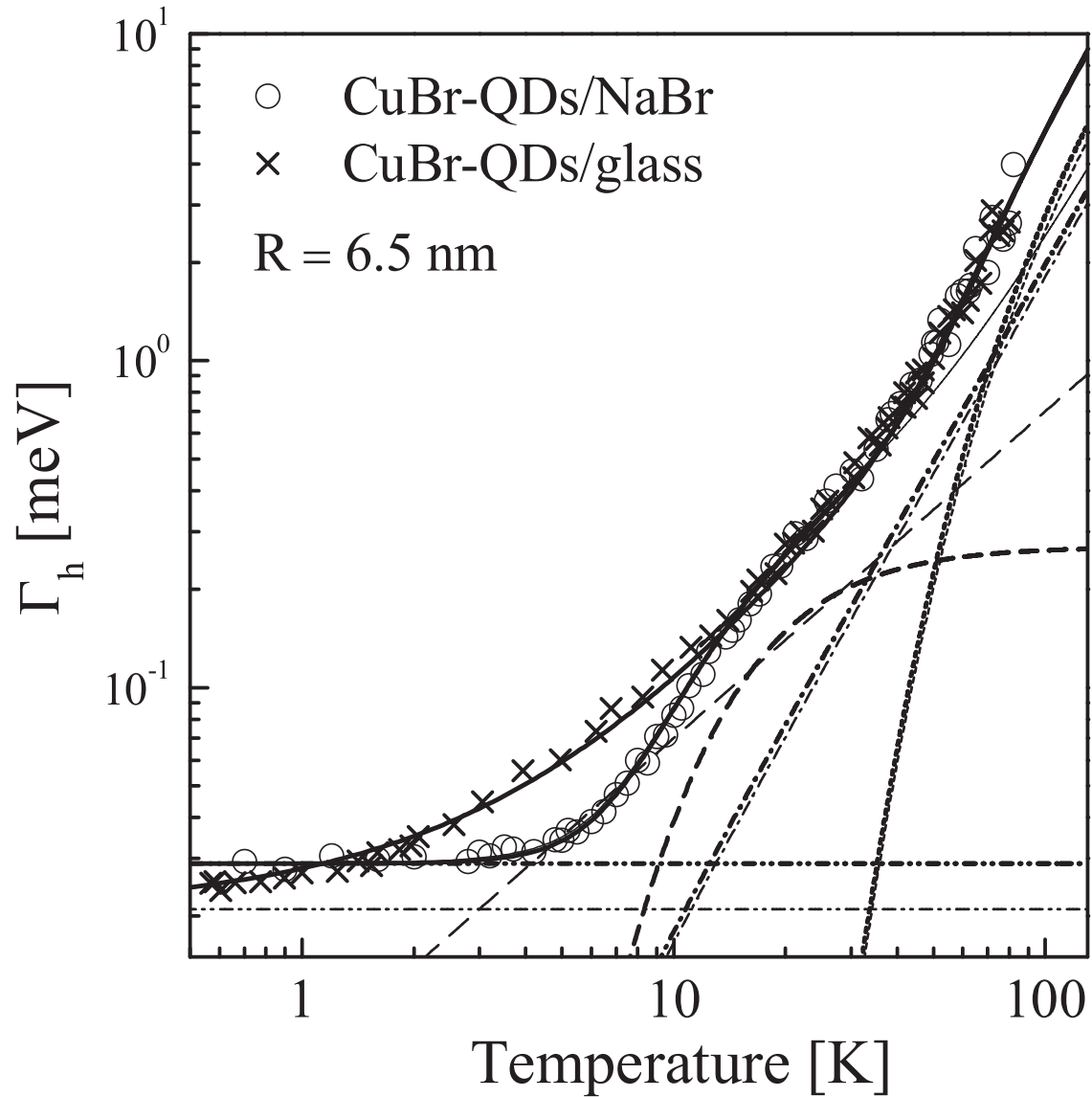
Figure 4.7: Temperature dependence of the homogeneous linewidth of CuBr-QDs/glass (crosses) and CuBr-QDs/NaBr (open circles) with radius of 6.5 nm. For the lines, refer Figs. 4.5 and 4.6. The fitting parameters were $\Gamma_{h0} = 0.019 \, \text{meV}$, $\hbar\omega = 0.89 \, \text{meV}$ for CuBr-QDs/glass, and $\Gamma_{h0} = 0.029 \, \text{meV}$, $\hbar\omega = 0.95 \, \text{meV}$, $\delta = 2.8 \, \text{meV}$ for CuBr-QDs/NaBr.
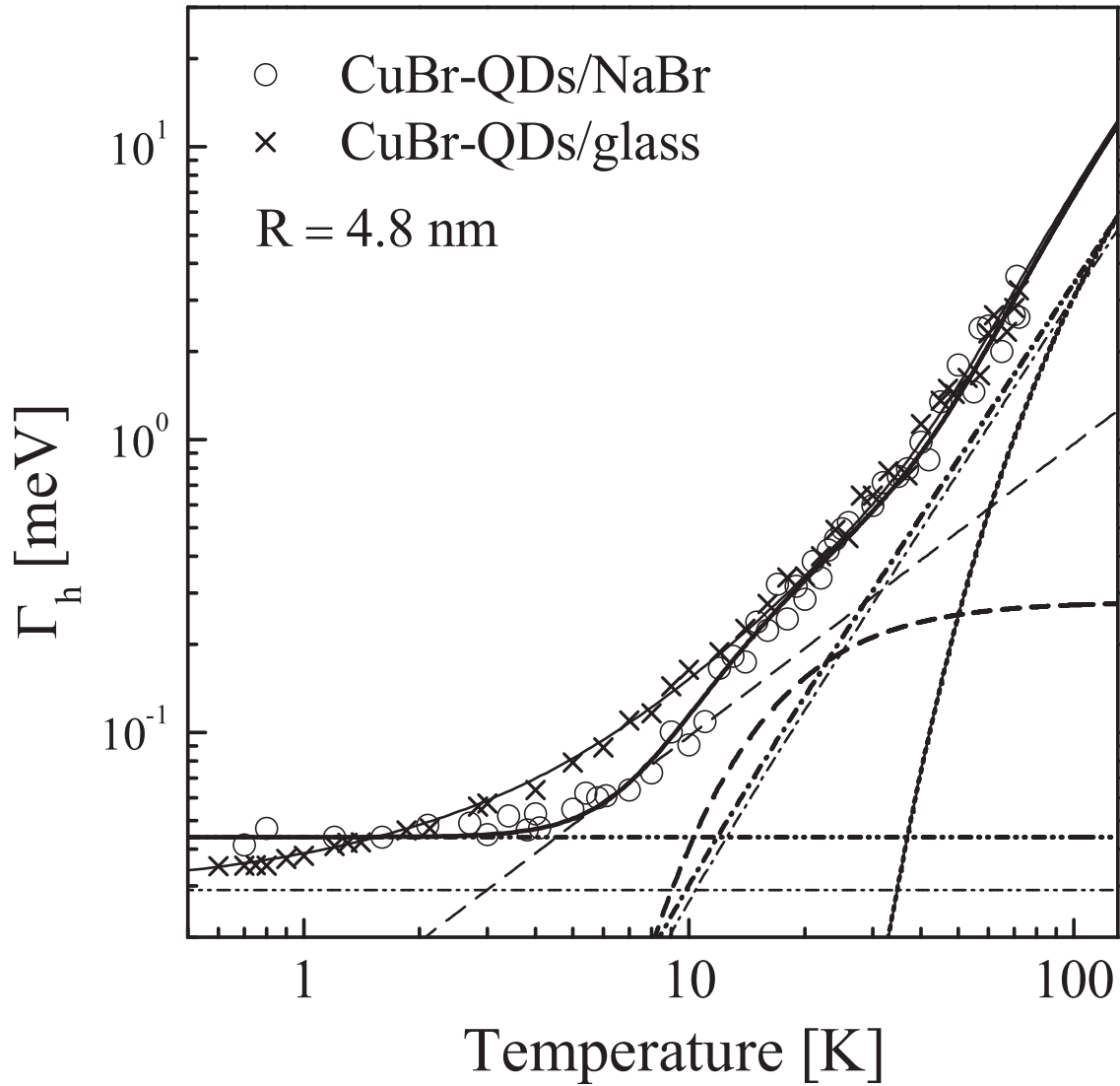
Figure 4.8: Temperature dependence of the homogeneous linewidth of CuBr-QDs/glass (crosses) and CuBr-QDs/NaBr (open circles) with radius of 4.8 nm. The fitting parameters were $\Gamma_{h0} = 0.029\,\text{meV}$, $\hbar\omega = 1.2\,\text{meV}$ for CuBr-QDs/glass, and $\Gamma_{h0} = 0.044\,\text{meV}$, $\hbar\omega = 1.1\,\text{meV}$, $\delta = 2.8\,\text{meV}$ for CuBr-QDs/NaBr.
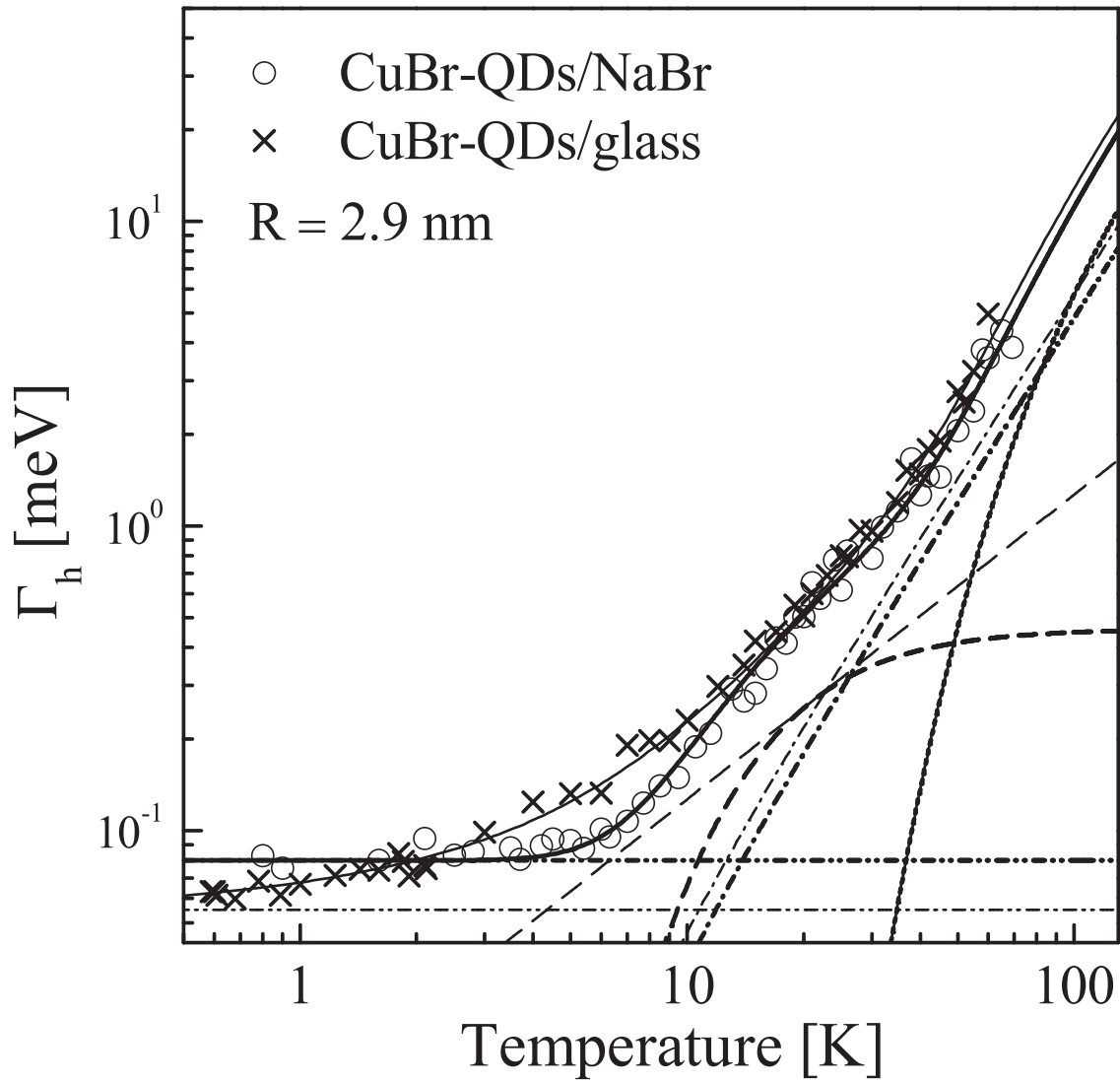
Figure 4.9: Temperature dependence of the homogeneous linewidth of CuBr-QDs/glass (crosses) and CuBr-QDs/NaBr (open circles) with radius of 2.9 nm. The fitting parameters were $\Gamma_{h0} = 0.055\,\text{meV}$, $\hbar\omega = 1.4\,\text{meV}$ for CuBr-QDs/glass, and $\Gamma_{h0} = 0.08\,\text{meV}$, $\hbar\omega = 1.7\,\text{meV}$, $\delta = 2.8\,\text{meV}$ for CuBr-QDs/NaBr.
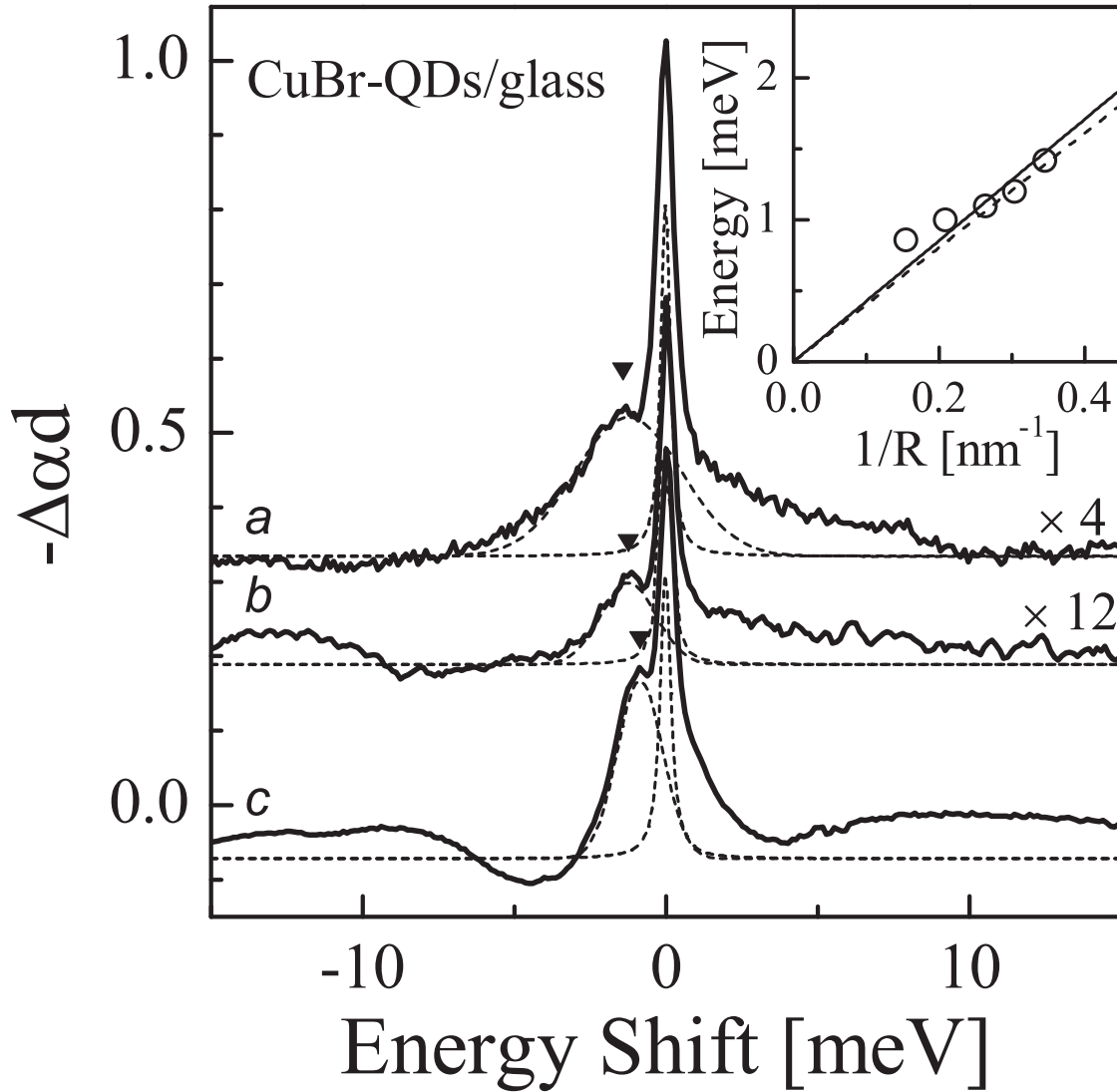
Figure 4.10: Persistent hole-burning spectra of CuBr-QDs/glass with radii of **a.** 2.9 nm, **b.** 4.8 nm and **c.** 6.5 nm observed at 2 K [10]. Dotted lines indicate Gaussian fittings to the zero-phonon hole and the Stokes-side confined phonon hole. Inset: Size dependence of the confined phonon energies obtained from the PSHB measurement for CuBr-QDs/glass (average radii are 2.9, 3.3, 3.8, 4.8 and 6.5 nm). The solid line indicates linear least-squares fit to the data. The dotted line is the calculation for the lowest spheroidal mode ($l = 1$, $n = 1$).
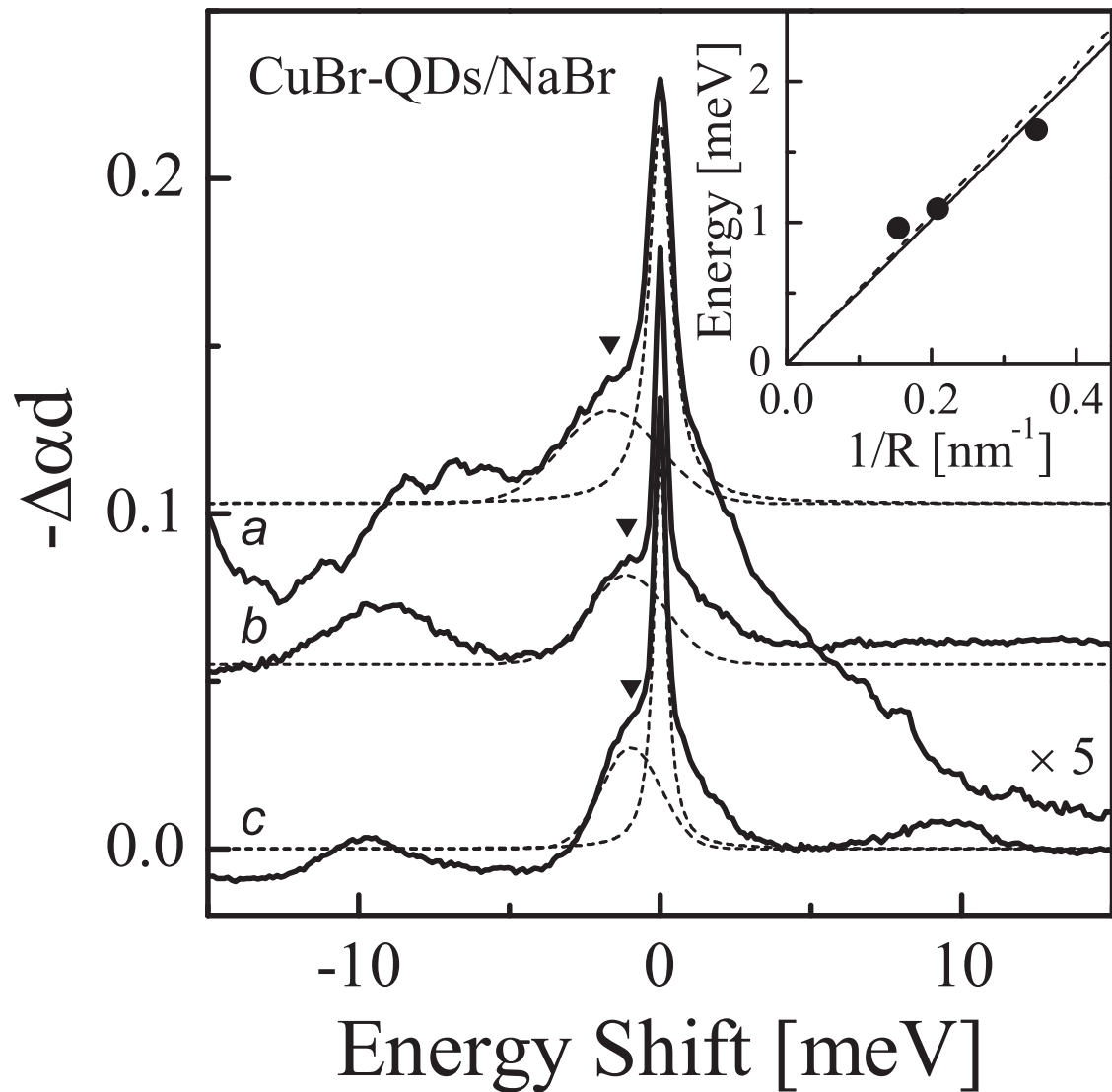
Figure 4.11: Persistent hole-burning spectra of CuBr-QDs/NaBr with radii of **a.** 2.9 nm, **b.** 4.8 nm and **c.** 6.5 nm observed at 2 K [10]. Dotted lines indicate Gaussian fittings to the zero-phonon hole and the Stokes-side confined phonon hole. Inset: Size dependence of the confined phonon energies obtained from the PSHB measurement for CuBr-QDs/NaBr (average radii are 2.9, 4.8 and 6.5 nm). The solid line indicates linear least-squares fit to the data. The dotted line is the calculation for the lowest spheroidal mode ($l = 0$, $n = 1$).

4.5 Comparative Discussion of Low-Temperature Dephasing Mechanism

The size dependence of the homogeneous widths extrapolated to 0 K for CuBr and CdSe quantum dots are displayed in Fig. 4.13. The experimental data are characterized well by a linear inverse size dependence, i.e., $\Gamma_{h0} \propto 1/R$. The temperature-independent width Γ_{h0} is broader than the inverse of nonradiative lifetime: 100 ps for CdSe-QDs/glass and 70 ps [16] for CuBr-QDs/glass, measured by time-resolved luminescence decay and induced absorption change as the fast-decay component. This indicates that the residual broadening mechanism at low temperature is not dominated by the lifetime broadening but by the surface-related dephasing process.

Here we consider again the origin of this temperature-independent dephasing mechanism. We assume that the surface defect sites distribute within a spherical shell with small thickness of Δd around the quantum dot (Fig. 4.12). In this assumption, the effective number of surface defect sites which can contribute to the scattering with confined excitons is written as

$$n' = 4\pi R^2 \rho \Delta d, \tag{4.3}$$

where ρ is the density of surface defect sites per unit and R is the radius of the spherical dot. By assumption that these defect sites are uniformly distributed in the dot (lower part of Fig. 4.12), the mean free path of the exciton $\overline{x}$ is given by

$$\overline{x} = \left(\frac{n'}{V}\right)^{-1} \propto \frac{R}{\rho \, \Delta d}. \tag{4.4}$$

where V is the volume of the dot. When ρ and Δd is independent on radius of the dot,
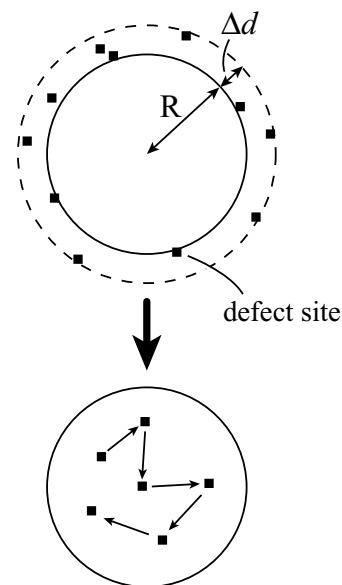
Figure 4.12: A schematic figure of the surface defect sites.
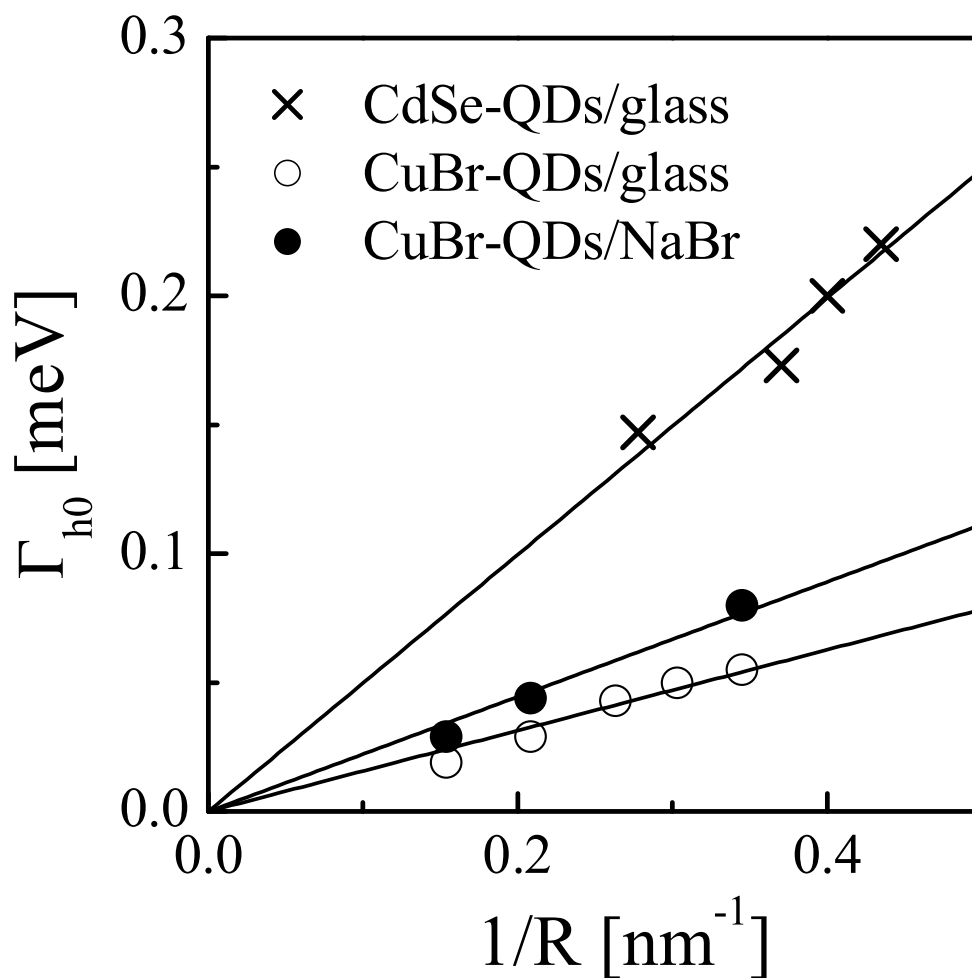
Figure 4.13: The size dependence of the homogeneous linewidth extrapolated to 0 K for CdSe-QDs/glass, CuBr-QDs/glass and CuBr-QDs/NaBr. Solid lines indicate linear least-squares fitting to the data.

and average velocity of the exciton is constant, the scattering rate τ is given by

$$\tau = \overline{x}^{-1} \propto \frac{1}{R}. \tag{4.5}$$

For all the samples, not only Γ_{h0} but also the coefficients of the TLS term, A, were found to increase linearly depending on R^{-1}. This suggests that the surface-driven dephasing is the dominant mechanism for both CuBr and CdSe quantum dots embedded in matrices at low temperature.

As for CuCl quantum dots in glass (CuCl-QDs/glass) and CuCl quantum dots in NaCl

(CuCl-QDs/NaCl), a detailed research of temperature-dependent homogeneous broadening has been reported by Ikezawa [3] for the lowest Z_3 exciton transition using the accumulated photon echo. Figure 4.16 show the comparison of the time-trace HAPE signals for CuCl-QDs/glass, CuCl-QDs/NaCl, CuBr-QDs/glass, CuBr-QDs/NaBr, and CdSe-QDs/glass at ≈ 0.6 K. The dephasing curve shows single-exponential decay for CuBr-QDs/glass and CuBr-QDs/NaBr, while double-exponential decay was observed for CuCl-QDs/glass, CuCl-QDs/NaCl, and CdSe-QDs/glass. The fast decay component comes from the confined-acoustic-phonon sideband as discussed in Chapter 3. The lack of the fast-decay component in CuBr-QDs/glass and CuBr-QDs/NaBr may indicate the weaker intensity of the confined-phonon sideband compared to the other samples.

The zero-phonon linewidths obtained from the dephasing time at the lowest temperature in Fig. 4.16, such as $\Gamma_h = 150$ μeV for CdSe-QDs/glass, 25 μeV for CuBr-QDs/glass and 1 μeV for CuCl-QDs/NaCl, were much smaller than the hole width measured by the PSHB at 2 K ($\Gamma_{hole} = 14$ meV, 1 meV and 70 μeV, respectively [1, 13, 17, 18]). These discrepancies may come from the spectral diffusion during the long persistent time in the hole-burning measurement. The spectral diffusion is the phenomenon where exciton transition frequencies wander during long time period between burning and reading of the spectral hole, leading to the ensemble hole broadening. These fluctuations were observed for CdSe single quantum dot overcoated with ZnS for example [19], in which the spectral shifts were explained by the presence of charge carriers on or near the surface of quantum dot leading to randomly oriented local electric fields that change over time. In our TLS model, the excitonic dephasing is also thought to be induced by the changes in local fields arising from charge flips of neighboring potential wells in the host matrix. Therefore, if the spectral diffusion has dominant influence on the homogeneous broadening during the accumulation time of the photon-echo signals, the homogeneous width should evolves with time diffusively. However, the observed dephasing time in our experiment has shown no difference as a function of the waiting time between write-in and read-out process ranging from 300 ms to 40 s. This means that the spectral diffusion hardly affects the homogeneous

linewidth in the accumulated photon echo experiment in this time scale. In other words, it may indicates that the homogeneous broadening due to the two-small-energy-excitation process in the TLS is to be static in tens of seconds and is determined only by the TLS-energy distribution at fixed temperature.

Figure 4.17 shows the whole temperature dependence of CdSe-QDs/glass, CuBr-QDs/glass, CuBr-QDs/NaBr, CuCl-QDs/glass, and CuCl-QDs/NaCl. For CuCl and CuBr quantum dots, matrix-dependent homogeneous broadening is clearly seen at low temperature. The TLS energy for CuCl quantum dots and CuBr quantum dots was $\delta_{CuCl} = 1$ meV and $\delta_{CuBr} = 2.8$ meV, respectively. This small-energy-excitation in the TLS determines the characteristic temperature for glass-matrix and crystal-matrix samples, below which temperature-dependent curves deviate from each other. On the other hand, two-phonon Raman scattering with confined acoustic phonons was observed for all the samples. In CuCl quantum dots, confined phonon sidebands were also experimentally observed by PSHB [20, 21] whose energy was $\hbar\omega = 1.6$ meV.

Finally, we would like to comment on difference of the extrapolated 0-K linewidth (Γ_{h0}) for CdSe, CuBr and CuCl quantum dots in Fig. 4.17. The dephasing time at the low-temperature limit for 2.0 nm CuCl-QDs/glass was 620 ps, which was much longer than the value for 6.5 nm CuBr-QDs/glass ($T_2 \approx 50$ ps) and 3.6 nm CdSe-QDs/glass ($T_2 \approx 8$ ps). This indicates that the homogeneous width becomes smaller with the increase of exciton Bohr radii which are 0.7, 1.3 and 5.6 nm for CuCl, CuBr and CdSe bulk crystals, respectively. In Fig. 4.14, we plotted Γ_{h0} of CuCl-QDs/glass, CuBr-QDs/glass and CdSe-QDs/glass as a function of a_B/R which is a factor related to the confinement strength. The Γ_{h0} depends on a_B/R almost linearly for CdSe and CuBr quantum dots. Only for CuCl quantum dots, the Γ_{h0} deviated from the fitting and showed much narrower linewidth. These results suggest the possibility of the confinement-strength-dependence of the homogeneous width at the very low temperature. The quantum dots where the exciton Bohr radius is much larger than the size of quantum dots is called as the strong confinement system. In the strong confinement system, the kinetic energies of confined electron and hole
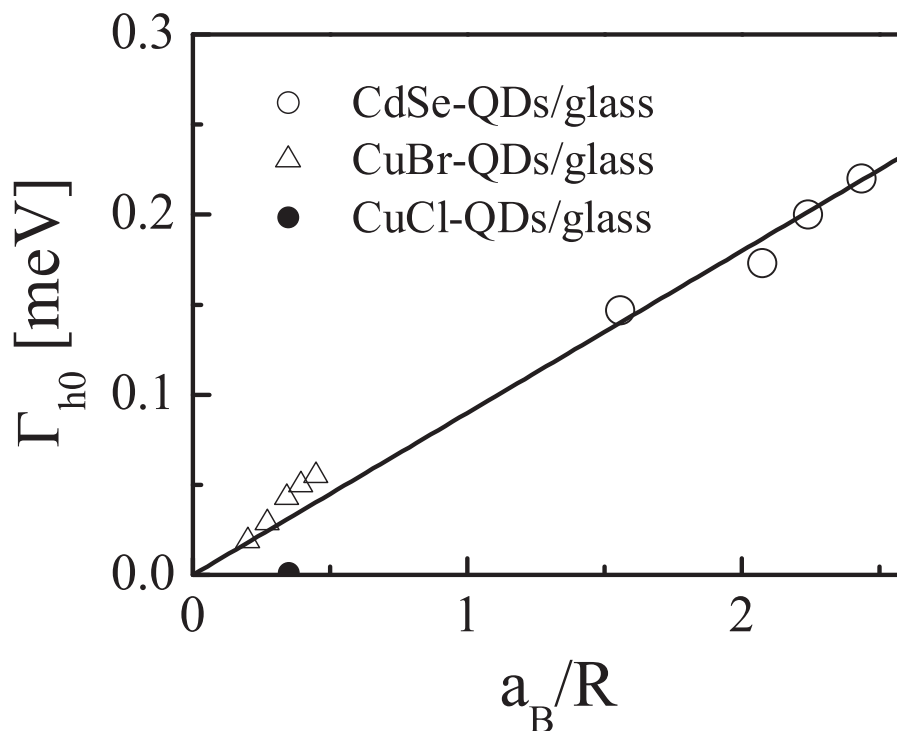
Figure 4.14: The homogeneous linewidth extrapolated to 0 K for CdSe-QDs/glass, CuBr-QDs/glass and CuCl-QDs/glass as a function of a_B/R where a_B is the exciton Bohr radius in bulk crystals. A solid line shows the least-squares fit to the data for CdSe and CuBr quantum dots.

are much larger than the Coulomb potential between them, and then the electron and hole are confined in the quantum dots individually. In such a system, an electron-hole pair in a quantum dot can be partly polarized if the surrounding medium has local electric field. On the other hand, in the quantum dots in the weak confinement regime such as CuCl quantum dots where the Coulomb potential between the electron and hole are so large that the translational motion of exciton is confined, a confined electron-hole pair is considered to behave as a neutral particle, an exciton, even if the surrounding medium has local electric field. The optical properties in quantum dots are strongly affected by whether the confined electron-hole pair is polarized or not because of the interaction with local electric fields coming from trapped carriers near the quantum dots. A possible charge-flipping process near the quantum dots can affect the homogeneous broadening even at the lowest temper-
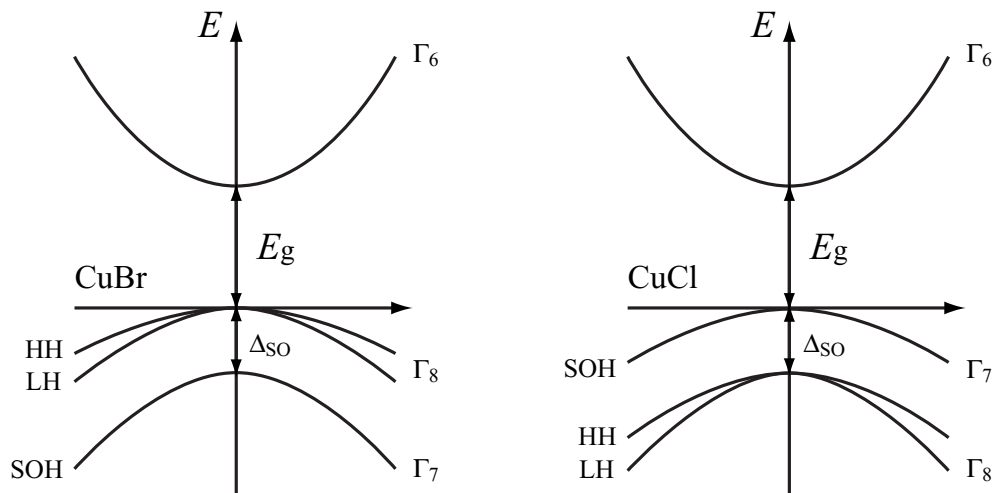
Figure 4.15: Schematic figure of energy band structure of bulk CuBr and CuCl. The HH, LH and SOH indicates the heavy-hole, light-hole and spin-orbit split-off bands, respectively.

atures. It is plausible that the quantum dots in the strong confinement regime show much broader Γ_{h0} than that in the weak confinement regime because the polarized electron-hole pair interacts with the local electric fields while the neutral pardicle does not.

As a reason for relatively short dephasing time in CuBr and CdSe quantum dots compared to CuCl quantum dots, the fine structures in the lowest exciton transition states may be considered. In CdSe quantum dots, it is known that the lowest-energy exciton-transition state ($1S_{3/2}1S_e$) is eightfold degenerate. This lowest-transition state is split into five sublevels because of the effects of the hexagonal lattice [22], the nonspherical shape [23], and electron-hole exchange interaction [24]. The five sublevels are labeled by $|N_m|$ which is the projection of the total angular momentum N along the unique crystal axis: one sublevel with $|N_m| = 2$, two with $|N_m| = 1$, and two with $|N_m| = 0$. In our case, the smallest energy splitting between optically active states and inactive states ranges from 1-4 meV for CdSe-QDs/glass with radii of 2.7-3.6 nm [25]. For CuBr, the lowest-energy exciton state is two-fold degenerated at the center of Brillouin zone, involving heavy and light holes ($Z_{1,2}$ exciton). In addition the energy-level splitting due to the k-linear term cannot be neglected for the heavy-hole exciton. The k-linear term is a factor which brings

about anisotropic multicomponents in the $Z_{1,2}$ exciton states because of the lack of the inversion symmetry in these crystals [26, 27]. According to Itoh *et al.*, the energy splitting in the lowest-$Z_{1,2}$ exciton states for our 6.5-nm-radius CuBr-QDs/glass corresponds to $\approx$ 20 meV [4]. On the other hand, this fine structure of the lowest-transition states cannot be observed for CuCl quantum dots because the relative positions of the $Z_{1,2}$ and Z_3 excitons are reversed (Fig. 4.15). In this case, the lowest Z_3-exciton transition in CuCl is simply given by an isotropic dispersion. Therefore, we may attribute the relatively short dephasing time observed in CuBr and CdSe quantum dots compared to CuCl quantum dots to the splitting of the band-degeneracy in the lowest-exciton-transition state which results in the additional broadening due to the intraband scattering process occurring even in the lowest-temperature region.
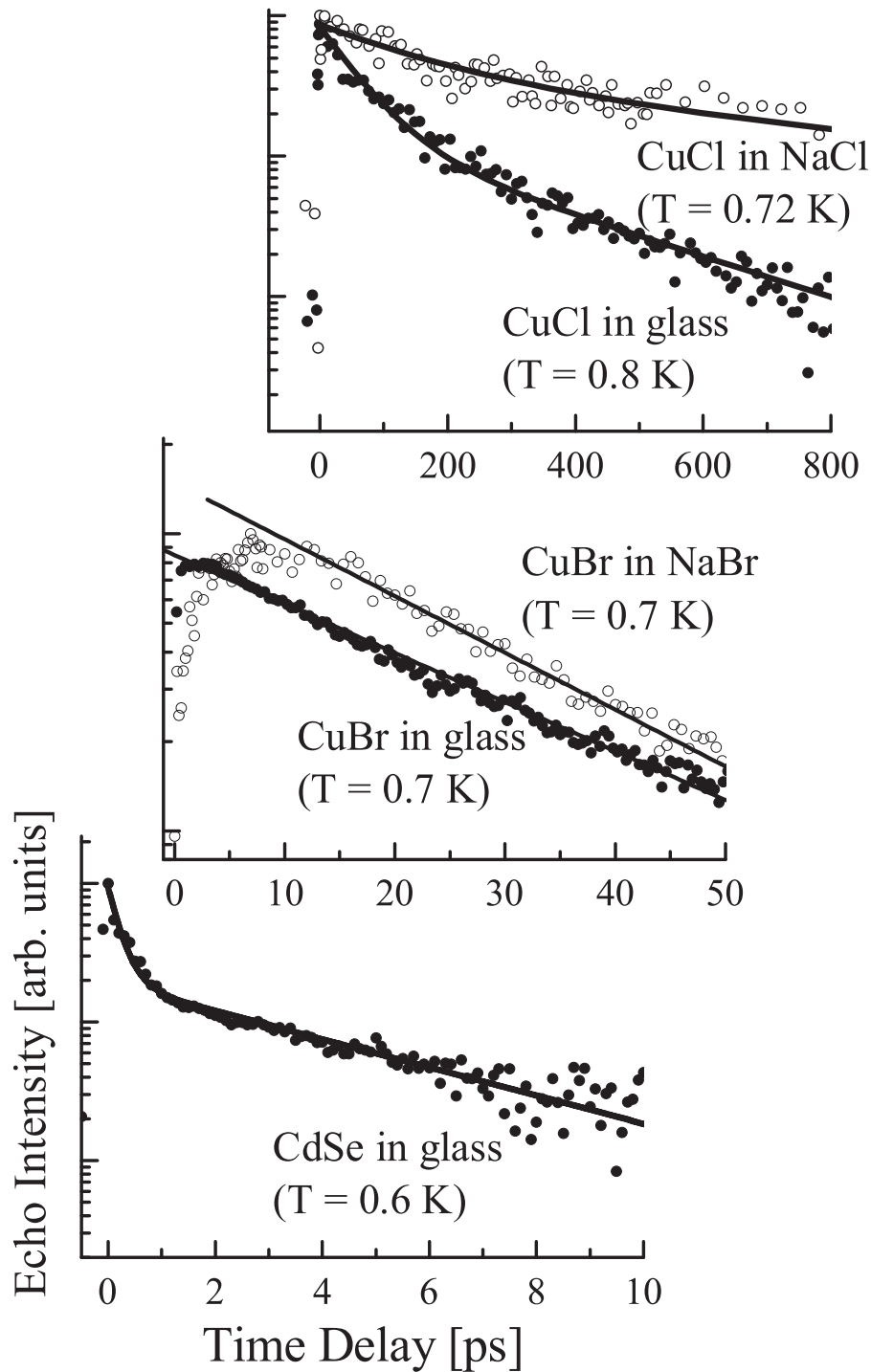
Figure 4.16: Time-trace signals of accumulated photon echo for CuCl-QDs/glass (R = 2.0 nm), CuCl-QDs/NaCl (R = 2.0 nm), CuBr-QDs/glass (R = 6.5 nm), CuBr-QDs/NaBr (R = 6.5 nm) and CdSe-QDs/glass (R = 3.6 nm) at very low temperature. The dephasing times corresponding to zero-phonon linewidth are 620 ps, 1.3 ns, 52.6 ps, 45.4 ps, and 8.6 ps, respectively.
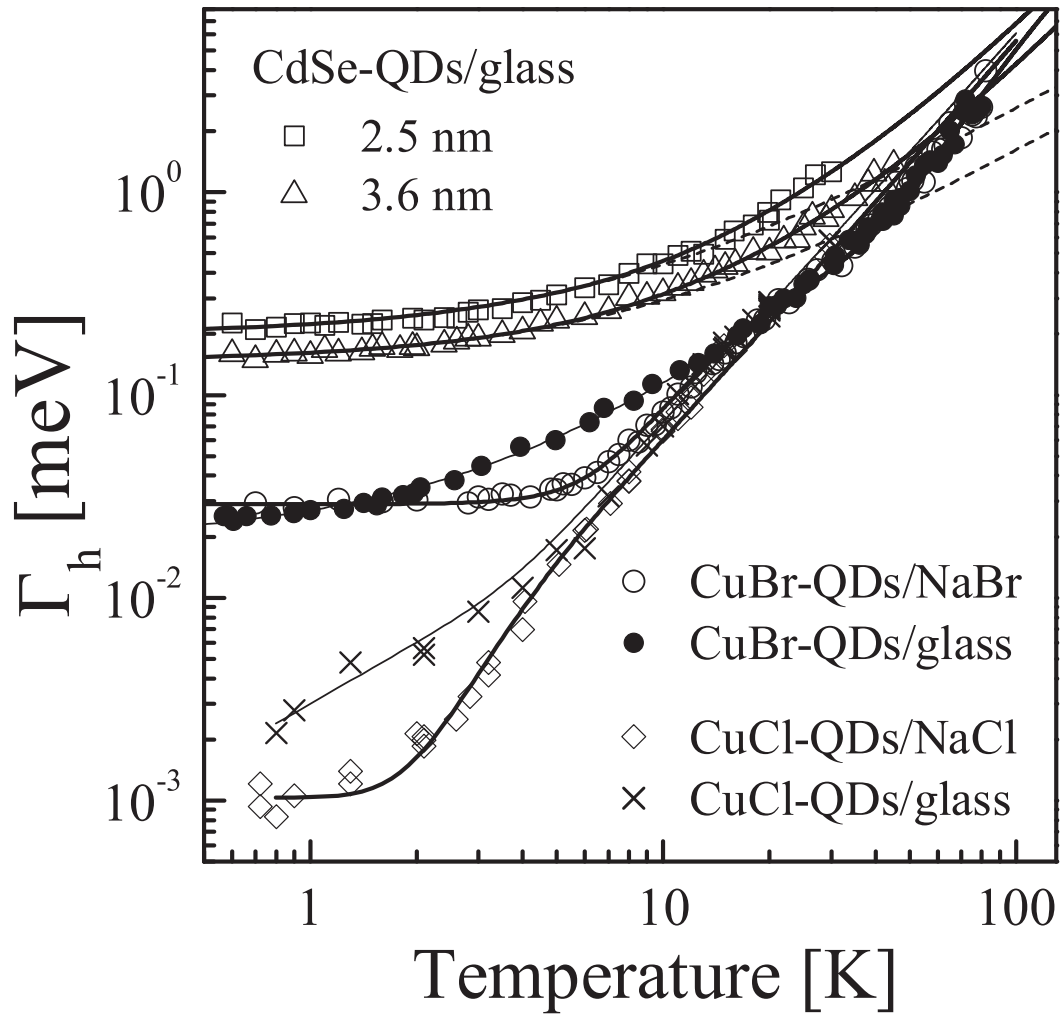
Figure 4.17: Temperature dependence of the homogeneous linewidth of CdSe-QDs/glass (R = 2.5 nm and 3.6 nm), CuBr-QDs/glass (R = 6.5 nm), CuBr-QDs/NaBr (R = 6.5 nm), CuCl-QDs/glass (R = 2.0 nm) and CuCl-QDs/NaCl (R = 2.0 nm).

4.6   Summary

The accumulated photon echo measurement has been performed for CuBr quantum dots embedded in glass and in NaBr matrices. By detailed measurement of the temperature dependence of the homogeneous linewidth, it has been clarified that the excitonic dephasing rate is determined by the following four mechanisms: (A) one-phonon scattering process with LO-phonons (above 40 K), (B) two-phonon Raman scattering process with confined acoustic phonons (above 15 K), (C) the exciton-TLS interaction (below 15 K), and (D) surface scattering process (at ~ 0 K).

There are two types of TLS: one is the case the TLS energy is widely distributed throughout the glassy matrix, and the other is the case the TLS energy is represented by one characteristic energy, δ. This difference affects the dephasing rate of confined exciton in quantum dots in the low-temperature region. This result corresponds to the previously reported matrix-dependent dephasing process of excitons confined in CuCl quantum dots in glass and in NaBr matrices.

Not only for CuBr but for CdSe quantum dots, the homogeneous linewidth extrapolated to 0 K depended linearly on $1/R$, suggesting dominant contribution of surface- or interface-related dephasing process in quantum dots embedded in matrices.

References

[1] J. Valenta, J. Moniatte, P. Gilliot, B. Hönerlage, J. B. Grun, R. Levy, and A. I. Ekomov, Phys. Rev. B **57**, 1774 (1998).

[2] T. Kuroda, F. Minami, K. Inoue, and A. V. Baranov, Phys. Rev. B **57**, R2077 (1998).

[3] M. Ikezawa and Y. Masumoto, Phys. Rev. B **61**, 12662 (2000).

[4] T. Itoh, Y. Iwabuchi, and T. Kirihara, Phys. Stat. Sol. (b) **146**, 531 (1988).

[5] H. Overhof, Phys. Stat. Sol. (b) **97**, 267 (1980).

[6] B.-R. Hyun, in *Coherent Dynamics of Excitons in Semiconductor Quantum Dots* (Doctoral thesis, University of Tsukuba, 1999).

[7] M. Grundmann, J. Christen, N. N. Ledentsov, J. Böhrer, D. Bimberg, S. S. Rumimov, P. Werner, U. Richter, U. Gösele, J. Heydenreich, V. M. Ustinov, A. Yu. Egorov. A. E. Zhukov. P. S. Kop'ev, and Zh. I. Alferov, Phys. Rev. Lett. **74**, 4043 (1996).

[8] U. Bockelman and G. Bastard, Phys. Rev. B **42**, 8947 (1990).

[9] H. Benisty, C. M. Sotomayer Torres, and C. Weisbuch, Phys. Rev. B **44**, 10945 (1991).

[10] J. Zhao, in *Confined Exciton States and Phonon Modes in Cuprous Halide Quantum Dots* (Doctoral thesis, University of Tsukuba, 1999).

[11] L. Saviot, B. Champagnon, E. Duval, I. A. Kudriavtsev, and A. I. Ekimov, J. Non-Cryst. Solids **197**, 238 (1996).

[12] N. N. Ovsyuk and V. N. Novikov, Phys. Rev. B **53**, 3113 (1996).

[13] For review, see: Y. Masumoto, J. Lumin. **70**, 386 (1996).

[14] P. W. Anderson, B. I. Halperin, and C. M. Varma, Philos. Mag. **25**, 1 (1972); W. A. Phillips, J. Low Temp. Phys. **7**, 351 (1972).

[15] D. L. Huber, M. M. Broer, and B. Golding, Phys. Rev. Lett. **52**, 2281 (1984).

[16] T. Okuno, H. Miyajima, A. Satake, and Y. Masumoto, Phys. Rev. B **54**, 16952 (1996).

[17] Y. Masumoto, T. Kawazoe, and N. Matsuura, J. Lumin. **76&77**, 189 (1998).

[18] Y. Masumoto, S. Okamoto, T. Yamamoto, and T. Kawazoe, Phys. Stat. Sol (b) **188**, 209 (1994).

[19] S. A. Empedocles and M. G. Bawendi, Science **278**, 2114 (1997).

[20] S. Okamoto and Y. Masumoto, J. Lumin. **64**, 253 (1995).

[21] J. Zhao and Y. Masumoto, Phys. Rev. B **49**, 5821 (1994).

[22] Al. L. Efros, Phys. Rev. B **46**, 7748 (1992).

[23] Al. L. Efros and A. V. Rodina, Phys. Rev. B **47**, 10005 (1993).

[24] M. Nirmal, D. J. Norris, M. Kuno, M. G. Bawendi, Al. L. Efros, and M. Rosen, Phys. Rev. Lett. **75**, 3728 (1995).

[25] D. J. Norris, Al. L. Efros, M. Rosen, and M. G. Bawendi, Phys. Rev. B **53**, 16347 (1996).

[26] S. Suga, K. Cho, Y. Niji, J. C. Merle, and T. Sauder, Phys. Rev. B **22**, 4931 (1980).

[27] Y. Nozue, J. Phys. Soc. Japan **51**, 1840 (1982).

Chapter 5

Conclusion

We have investigated systematically the homogeneous linewidth of CdSe quantum dots in strong confinement regime, CuBr quantum dots in intermediate confinement regime at low temperature using the heterodyne-detected accumulated photon echo. The temperature dependence of the homogeneous width for CdSe-QDs/glass was explained by the combination of T-linear contribution coming from exciton-TLS interaction and quadratic contribution coming from exciton-confined-phonon interaction. For CuBr-QDs/glass, the contribution of exciton-LO-phonon scattering was also observed at higher temperature in addition to the above component. For CuBr-QDs/NaBr, the temperature dependence of the homogeneous width was reproduced by the same expression as for CuBr-QDs/glass, but TLS energy distribution is considered to concentrate on one characteristic energy, $\delta \approx 2.8$ meV. The difference of the energy distribution of the TLS energy brings about the different temperature dependence at very low temperature. This feature agrees well with the result of CuCl quantum dots in strong confinement regime.

The homogeneous width extrapolated to 0 K depends on the inverse radius of quantum dots, indicating the surface-related dephasing process. The detailed study of the homogeneous width of quantum dots ranging from weak confinement regime to strong confinement regime have revealed that the low-temperature dephasing mechanism of confined excitons is understood in terms of universal mechanisms: two-acoustic-phonon process and two-small-energy-excitation process in two-level-system.

Acknowledgment

List of Publications

Following papers have been or will be published concerning with the present study.

1. **"Homogeneous optical spectrum of CdSe quantum dots observed by accumulated photon echo"**,

   Yasuaki Masumoto, Kazuya Takemoto, Takuya Shoji, and Byung-Ryool Hyun :

   Proceedings of the 24th International Conference on the Physics of Semiconductors, Jerusalem, Th2-C5 (1998).

2. **"Observation of homogeneous optical spectrum in CdSe quantum dots using femtosecond accumulated photon echo"**,

   Kazuya Takemoto, Byung-Ryool Hyun, and Yasuaki Masumoto :

   Journal of Luminescence **87-89**, 485 (2000).

3. **"Heterodyne-detected accumulated photon echo in CdSe quantum dots"**,

   Kazuya Takemoto, Byung-Ryool Hyun, and Yasuaki Masumoto :

   Solid State Communications **114**, 521 (2000).

4. **"Homogeneous line broadening mechanism of quantum dots"**,

   Byung-Ryool Hyun, Masashi Furuya, Kazuya Takemoto, and Yasuaki Masumoto :

   Journal of Luminescence **87-89**, 302 (2000).

5. **"Homogeneous width of confined excitons in quantum dots at very low temperatures"**,

   Yasuaki Masumoto, Michio Ikezawa, Byung-Ryool Hyun, Kazuya Takemoto, and Masashi Furuya :

   Physica Status Solidi (b) **224**, 613 (2001).

6. **"Residual dephasing mechanism at low temperature in semiconductor quantum dots"**,

   Kazuya Takemoto, Michio Ikezawa, and Yasuaki Masumoto :

   Proceedings of the 26th International Conference on the Physics of Semiconductors, Edinburgh, H145 (2002).

7. **"Coherent acoustic phonons in quantum dots"**,

   Michio Ikezawa, Kazuya Takemoto, and Yasuaki Masumoto :

   Proceedings of the 26th International Conference on the Physics of Semiconductors, Edinburgh, H140 (2002).

8. **"Low-temperature dephasing mechanism of very small quantum dots: The role of confined phonons and surrounding matrices"**,

   Kazuya Takemoto, Michio Ikezawa, and Yasuaki Masumoto :

   to be published in Physica Status Solidi (b).

9. **"Universal dephasing mechanism in semiconductor quantum dots embedded in matrix"**,

   Kazuya Takemoto, Byung-Ryool Hyun, Masashi Furuya, Michio Ikezawa, Jialong Zhao, and Yasuaki Masumoto :

   to be published in Journal of the Physical Society of Japan **72** (2003).